



Neda Neisi

# DYNAMIC AND THERMAL MODELING OF TOUCH-DOWN BEARINGS CONSIDERING BEARING NON-IDEALITIES



Neda Neisi

## **DYNAMIC AND THERMAL MODELING OF TOUCH-DOWN BEARINGS CONSIDERING BEARING NON-IDEALITIES**

Dissertation for the degree of Doctor of Science (Technology) to be presented with due permission for public examination and criticism in the Auditorium 1316 at Lappeenranta-Lahti University of Technology LUT, Lappeenranta, Finland on the 26<sup>th</sup> of June, 2020, at noon.

Acta Universitatis  
Lappeenrantaensis 909

Supervisors Professor Jussi Sopenen  
LUT School of Energy Systems  
Lappeenranta-Lahti University of Technology LUT  
Finland

D.Sc.(Tech.) Janne Heikkinen  
LUT School of Energy Systems  
Lappeenranta-Lahti University of Technology LUT  
Finland

Reviewers Professor Patrick Keogh  
Department of Mechanical Engineering  
University of Bath  
United Kingdom

Professor Ilmar Santos  
Department of Mechanical Engineering  
Technical University of Denmark  
Denmark

Opponents Professor Ilmar Santos  
Department of Mechanical Engineering  
Technical University of Denmark  
Denmark

Dr. Hunter Cloud  
President  
BRG Machinery Consulting, LLC  
Virginia-USA

ISBN ISBN 978-952-335-521-7  
ISBN ISBN 978-952-335-522-4 (PDF)  
ISSN-L 1456-4491  
ISSN 1456-4491

Lappeenranta-Lahti University of Technology LUT  
LUT University Press 2020

---

## Abstract

Neda Neisi

### **Dynamic and thermal modeling of touchdown bearings considering bearing non-idealities**

Lappeenranta 2020

74 pages

Acta Universitatis Lappeenrantaensis 909

Diss. Lappeenranta–Lahti University of Technology LUT

ISBN 978-952-335-521-7, ISBN 978-952-335-522-4 (PDF), ISSN-L 1456-4491, ISSN 1456-4491

In an active magnetic bearing (AMB) supported rotor, the touchdown bearings support the rotor in case of an electromagnetic field failure or a fault in the control system. In this work, a dynamic and thermal model of touchdown bearings was studied, and non-idealities in the bearing were taken into account. The effect of off-sized ball/balls on the stress in the touchdown bearing was investigated. The Hertzian contact model was applied to study the stress in the touchdown bearing. The results show that off-sized balls affect the load distribution in the bearing. Therefore, the contact forces and stresses change. The outcome indicates that stress in the touchdown bearing is affected by the dimension and location of off-sized ball.

Furthermore, heat generation due to the impact and collision of the rotor and touchdown bearing, in addition to the internal friction in the bearing, can raise the temperature of the touchdown bearing. The effect of different orders and amplitude of surface waviness in an angular contact ball bearing type of touchdown bearing were investigated. An equivalent electrical circuit model was used for the thermal model of the touchdown bearing. It was found that the surface waviness of the bearing alters the contact force and friction loss in the touchdown bearing. The effect of a higher amplitude of surface waviness on the thermal expansion of the touchdown bearing was also studied.

In addition, an experimental and numerical study on the dropdown of a rotor is presented. The recorded behavior of the rotor in the sudden failure of the electromagnetic field is demonstrated. A comparison between simulation results and dropdown test data can help the further development of the model. This was achieved in this study by considering the dropdown test data to determine the initial position of the rotor at the start of dropdown as well as the support properties. The machine was not equipped with force sensors for the touchdown

---

bearing. Non-contact displacement sensors were provided for monitoring the displacement of the rotor, which make it difficult to evaluate a safe dropdown. The model was verified by comparing the rotor orbits in the simulation and measurements. The Fast Fourier Transform (FFT) was applied to the measured displacement of the rotor and revealed the harmonics of the operation speed, rub-impact frequencies, pendulum motion of the rotor, as well as the first two bending frequencies of the rotor as it settled on the touchdown bearings. A critical speed map justified the bending frequencies of the rotor and identified the support properties. The study enables the comparison of a single dropdown in relation to a previous drop.

Keywords: touchdown bearing, rotor, dropdown, friction, thermal analysis, waviness, off-sized ball, force estimation

---

## Acknowledgements

This study was carried out in the Laboratory of Machine Dynamics at Lappeenranta-Lahti University of Technology LUT, Finland, between 2016 and 2020.

I would like to thank the following people, without whom I would not have been able to complete this dissertation. First and foremost, I would like to express my appreciation and gratitude to Professor Jussi Sopanen, who helped me to do my postgraduate studies in his team. He taught me how to start the research. His critical comments were helping to speed up the research. I would like to thank the second supervisor D.Sc. (Tech.) Janne Heikkinen, for his guidance during my studies. They always supported during the dissertation and publication process. The work presented here would not be completed without their help. Thanks to Aurelia Turbines Ltd for great cooperation to perform the dropdown tests on their gas turbine unit.

I also express my gratitude to the preliminary examiners, Professor Patrick Keogh from Bath University and Professor Ilmar Santos from the Technical University of Denmark. Their valuable comments helped greatly in improving the work. I also express my gratitude to the opponents Dr. C. Hunter Cloud President of BRG Machinery Consulting LLC, and Professor Ilmar Santos. I appreciate the effort they made for reviewing the dissertation.

I also would like to say thank you to all my current and former colleagues from the machine dynamics and machine design laboratory.

Thanks to my friends, you never let the distance separate us. You were increasing my energy to complete the dissertation. I am also in debt to my friends and my supervisors who helped me to start my doctoral study. Last, but not least, I would like to thank my family for their unconditional love and supports.

Neda Neisi  
June 2020  
Lappeenranta, Finland



**Abstract**

**Acknowledgements**

**Contents**

**List of publications** **9**

**Author's contributions** **11**

**Symbols and abbreviations** **13**

**1 Introduction** **17**

- 1.1 Motivation for the study . . . . . 17
- 1.2 Dynamic and thermal model of a touchdown bearing . . . . . 19
- 1.3 Surface waviness in touchdown bearings . . . . . 20
- 1.4 Stress in touchdown bearing with off-sized ball . . . . . 21
- 1.5 Dropdown test and touchdown bearing force . . . . . 21
- 1.6 Objective and scope of the dissertation . . . . . 22
- 1.7 Limitations . . . . . 23
- 1.8 Scientific contributions . . . . . 24

**2 A thermomechanical model of a touchdown bearing** **27**

- 2.1 Model of a rotor . . . . . 27
- 2.2 Model of a touchdown bearing . . . . . 28
  - 2.2.1 Model of the contact . . . . . 29
  - 2.2.2 Modeling of surface waviness . . . . . 31
  - 2.2.3 Thermal model of a bearing . . . . . 32
  - 2.2.4 Power loss in a touchdown bearing . . . . . 33
  - 2.2.5 Bearing deformation under thermal effects . . . . . 35
  - 2.2.6 Updating the model . . . . . 36
  - 2.2.7 Contact stress . . . . . 37

---

<b>3</b>	<b>Integrating dropdown test data with simulation data</b>	<b>39</b>
3.1	Procedure . . . . .	39
3.2	Initial conditions of the rotor . . . . .	41
3.3	Support properties . . . . .	41
3.4	Aerodynamic torque . . . . .	42
<b>4</b>	<b>Summary of findings</b>	<b>43</b>
4.1	Stress in a touchdown bearing . . . . .	43
4.1.1	Stress in a touchdown bearing with a single off-sized ball . . . . .	45
4.1.2	Multiple off-sized balls . . . . .	46
4.2	Dynamic and thermal model of a touchdown bearing . . . . .	46
4.2.1	Orbital motion of the rotor . . . . .	47
4.2.2	Effect of surface waviness . . . . .	48
4.2.3	Thermal analysis . . . . .	53
4.3	Force estimation of a touchdown bearing . . . . .	55
4.3.1	Support stiffness and damping . . . . .	56
4.3.2	Rotor orbit . . . . .	58
4.3.3	Bearing force . . . . .	59
4.3.4	Further analysis of experimental results . . . . .	61
4.3.5	Waterfall of the rotor dropdown . . . . .	62
<b>5</b>	<b>Conclusions</b>	<b>65</b>
5.1	Stress in a touchdown bearing with off sized ball . . . . .	65
5.2	Influence of surface waviness in the heat generation and thermal expansion of a touchdown bearing . . . . .	66
5.3	Model-based performance evaluation of a touchdown bearing . . . . .	66
	<b>References</b>	<b>69</b>
	<b>Publications</b>	

---

LIST OF PUBLICATIONS

---

This dissertation includes a comprehensive introduction and the following publications.

*Publication I*

Neisi, N., Sikanen, E., Heikkinen, J., Sopenan, J. Effect of off-sized balls on contact stresses in a touchdown bearing. *Tribology International*, 120 (2018) 340–349.

*Publication II*

Neisi, N., Heikkinen, J., Sopenan, J. Influence of surface waviness in the heat generation and thermal expansion of the touchdown bearing. *European Journal of Mechanics-A Solids*, 74 (2019) 34–47.

*Publication III*

Neisi, N., Ghalamchi, B., Heikkinen, J., Sillanpää, T., Hartikainen, T., Sopenan, J. A Case Study of the Contact Force and Stress in the Backup Bearing of a Generator: Experimental Study and Numerical Simulation of Dropdown. *Mechanisms and Machine Science*, IFToMM 2018: Proceedings of the 10th International Conference on Rotor Dynamics – IFToMM, Vol(62), 2019.

*Publication IV*

Neisi, N., Heikkinen, J., Sillanpää, T., Hartikainen, T., Sopenan, J. Performance evaluation of touchdown bearing using model-based approach. Accepted to *Nonlinear Dynamics*, 2020.



This section presents the contribution of the author in the writing of the following articles. The articles were written under the supervision of Professor Jussi Sopanen and D.Sc. (Tech.) Janne Heikkinen from LUT University.

*Publication I* investigates the maximum Hertzian stresses in a ball bearing type touchdown bearing. The study applies the Hertzian contact model to calculate the contact force and stresses in the dropdown. The dimensional non-ideality as an off-sized ball is taken into account. The study evaluates how the magnitude and the location of an off-sized ball influence the stress in the bearing.

Neda Neisi was the main author and investigator for this publication, who developed a model for the stress in the touchdown bearing and wrote the paper. The second author was responsible for extending the previous dropdown models developed at LUT to adopt with this case study. The authors finalized the work together.

*Publication II* presents a dynamic and thermal model of a touchdown bearing of an AMB supported rotor. A high-speed electric motor utilizing active magnetic bearings (AMB) was selected as a case study. This publication presents a numerical model for the power loss, frictional heat, thermal expansion, and temperature rise in a touchdown bearing. The study evaluates different orders and the magnitude of surface waviness in a touchdown bearing.

Neda Neisi was the main author, and investigator and was responsible for writing this publication. The author developed a model for the dynamic and thermal model of a touchdown bearing where the surface waviness was taken into account.

The authors finalized the work together.

*Publication III* presents a numerical and experimental study of the dropdown of a generator rotor in a two-stage radial gas turbine. The recorded behavior of the rotor in the sudden failure of an electromagnetic field is demonstrated. Furthermore, the contact force and the contact stress in the touchdown bearing were studied. The comparison of the simulation model with the measurement data presented in this publication helps to build an understanding of practical aspects that will be of use for further development of the simulation tools.

Neda Neisi was the main author, and investigator, who developed a model for a touchdown bearing of the rotor under investigation and studied the contact force and stress in the dropdown. Behnam Ghalamchi contributed to the modeling of the rotor-bearing system. Teemu Sillanpää conducted the dropdown tests and provided the measurement data. Toni Hartikainen was in charge of the necessary information for the machine and approved that the content was in accordance with the usual procedures of the Aurelia Turbines Ltd (manufacture of the generator rotor). Neda Neisi was responsible for developing the model, analyzing the results, and writing the paper. The authors finalized the work together.

*Publication IV* represents the second phase of the study of the system under investigation presented in *Publication III*. In this publication, the measurement data from the dropdown tests were integrated with the dropdown model. Neda Neisi was the principal author and investigator for this publication. The author was responsible for developing a model and was also responsible for writing the paper. Janne Heikkinen provided the critical speed map routine for the publication. Teemu Sillanpää conducted the dropdown test and provided the measurement data. Toni Hartikainen was in charge of the necessary information for the machine and approved that the content was in accordance with the usual procedures of the Aurelia Turbines Ltd. The authors finalized the work together.

---

SYMBOLS AND ABBREVIATIONS

---

ALPHABETICAL SYMBOLS

$A$	Inverse of the effective radius of curvature in the $x$ -direction
$A_m^{in}$	Amplitude of the $m^{th}$ waviness order in the inner ring
$A_m^{out}$	Amplitude of the $m^{th}$ waviness order in the outer ring
$a^*$	Semi-major axis of the elliptic area
$B$	Inverse of the effective radius of curvature in the $y$ -direction
$b^*$	Semi-minor axis of the elliptic area
$b$	Damping parameter
<b>C</b>	Damping matrix
$C$	Specific heat
$C_b$	Bearing damping
$\mathbf{C}_{brg}$	Matrix form of the specific heat for the bearing model
$C_{sup}$	Support damping
$c_r$	Radius of the air gap
$d_b$	Ball diameter
$d_e$	Inner diameter of the outer race
$d_h$	Housing diameter
$d_i$	Inner ring diameter
$d_m$	Pitch diameter
$d_o$	Outer ring diameter
$d_s$	Shaft diameter
$\frac{dT}{dt}$	Temperature gradient
$d$	Distance between the inner ring and outer ring
$E$	Modulus of elasticity for the contact body $I$ and $II$
$E^*$	Effective modulus of elasticity
$e_j^r$	Radial displacement between bearing rings
$e_j^t$	Axial displacement between bearing rings
$e_r$	Radial displacement of the rotor
$e_{x,r}, e_{y,r}$	Radial displacement between the rotor and the inner ring on the $x$ and $y$ -axis
$e_{x,y,z}$	Relative displacements between bearing rings along the main axes
<b>F</b>	Vector of externally applied forces
$F_j$	Contact force between ball and bearing ring
$F_r$	Contact force between the rotor and the touchdown bearing
$F_\mu$	Friction force between the rotor and the touchdown bearing
$f_{1,2}$	Factors dependent on the design and load on the bearing
<b>G</b>	Gyroscopic matrix

$\mathbf{H}_{in}^t$	Input heat flux
$\mathbf{H}_{out}^t$	Output heat flux
$H_i$	Heat generation in the inner ring
$H_{in}$	Input heat
$H_o$	Heat generation in the outer ring
$H_{out}$	Output heat
$H_r$	Heat generation in the contact between the rotor and the touchdown bearing
$h_h$	Convection heat transfer from the bearing housing
$I_p$	Polar moment of inertia of the rotor
$j$	Ball number
$\mathbf{K}$	Stiffness matrix
$K$	Contact stiffness between the rotor and the inner ring
$K_b$	Bearing stiffness
$K_c^{tot}$	Total contact stiffness
$K_{eq}$	Equivalent stiffness
$K_{sup}$	Support stiffness
$\mathbf{M}$	Mass matrix
$\mathbf{M}_{brg}$	Lumped mass matrix
$M$	Share of the rotor mass at the location of each support
$M_{ad}$	Aerodynamic torque in the deceleration of the rotor
$M_{ij}$	Friction torque in the inner ring
$M_{si}$	Spinning drag in the inner ring
$M_L$	Load dependent friction torque
$M_v$	Velocity dependent friction torque
$M_\mu$	Friction torque
$M^*$	Global friction in the bearing
$m_{in}$	Waviness order in the inner ring
$m_{out}$	Waviness order in the outer ring
$N_w$	Number of waves
$N^*$	Speed of the inner ring
$n^*$	Constant dependent on the contact type
$n$	Number of waves
$\dot{n}$	Derivative of the speed of the rotor during deceleration
$P$	Equivalent load of the ball bearing
$\mathbf{Q}$	Measurement matrix
$\mathbf{Q}_1$	Unbalance force vector
$\mathbf{Q}_2$	Unbalance force vector related to the acceleration of rotor
$\mathbf{q}$	Vector of the generalized coordinate
$R_e$	Contact curvature
$R_{in}, R_{out}$	Inner and outer raceway radius
$R_{1-9}$	Thermal resistances in bearing model

---

$\mathbf{r}_m$	Vector of the measured data
$\mathbf{r}_t$	Deformation at all degrees of freedom
$r_b$	Ball radius
$r_h$	Housing radius
$r_i$	Inner ring radius
$r_{in}, r_{out}$	Inner and outer raceway groove radius
$r_s$	Shaft radius
$\mathbf{T}^t$	Temperature at the current time
$\mathbf{T}^{t+\Delta T}$	Temperature at a new time step
$T$	Temperature
$T_b$	Ball temperature
$T_{ci}$	Temperature in the contact of ball/inner ring
$T_{co}$	Temperature in the contact of ball/outer ring
$T_h$	Housing temperature
$T_i$	Inner ring temperature
$T_o$	Outer ring temperature
$T_s$	Shaft temperature
$T_\infty$	Ambient temperature
$V$	Volume
$V_{rel}$	Relative velocity between the rotor and the inner ring
$W$	Bearing width

## GREEK SYMBOLS

$\alpha_b$	Thermal expansion coefficient of the ball
$\alpha_{in}$	Thermal expansion coefficient of the inner ring
$\alpha_{out}$	Thermal expansion coefficient of the outer ring
$\beta_j$	Azimuth angle of the $j^{th}$ ball
$\delta$	Penetration of the rotor on the inner ring
$\delta_j^{tot}$	Total elastic deformation of the bearing race
$\Delta T_b$	Temperature growth of the ball
$\Delta T_{ci}$	Temperature growth in the contact area of the ball/inner ring
$\Delta T_h$	Temperature growth of the housing
$\Delta T_{in}$	Temperature growth of the inner ring
$\Delta T_{out}$	Temperature growth of the outer ring
$\Delta t$	Time difference
$\epsilon_b$	Thermal expansion of the ball
$\epsilon_{in}$	Thermal expansion of the inner ring
$\epsilon_{out}$	Thermal expansion of the outer ring
$\zeta$	Elliptic integral of the second kind
$\theta$	Ball pitch angle

$\theta_{irw}$	Phase angles of the $m^{th}$ order waviness of the inner ring
$\theta_{orw}$	Phase angles of the $m^{th}$ order waviness of the outer ring
$\kappa$	Elliptic eccentricity parameter
$\lambda$	Contact parameter
$\mu$	Friction coefficient
$\nu$	Poisson's ratio for the contact body <i>I</i> and <i>II</i>
$\nu_{in}$	Poisson's ratio of the inner ring
$\nu_{out}$	Poisson's ratio of the outer ring
$\nu^*$	Kinematic viscosity
$\xi$	Elliptic integral of the first kind
$\rho$	Density
$\sigma_{max}$	Maximum Hertzian stress
$\Phi$	Modal matrix
$\varphi_i$	Contact angle in the inner ring
$\varphi_j$	Contact angle of the $j^{th}$ ball
$\varphi_o$	Contact angle in the outer ring
$\psi_{x,y}$	Misalignment of the inner ring along the $x, y$ -axis
$\omega, \omega_r$	Angular velocity of the rotor
$\omega_b$	Angular speed of the ball
$\omega_c$	Cage velocity
$\omega_{ci}$	Angular velocity in the contact area between the ball/inner ring
$\omega_{co}$	Angular velocity in the contact area between the ball/outer ring
$\omega_i$	Angular velocity of the inner ring
$\omega_k$	Natural frequency of the single mass system
$\omega_{si}$	Spinning velocity of the inner ring
$\omega_{so}$	Spinning velocity of the outer ring

## ABBREVIATIONS

AMB	Active magnetic bearings
DE	Drive end of the rotor
FEM	Finite element method
FFT	Fast Fourier Transform
NDE	Non drive end of the rotor
TB1	Touchdown bearing 1
TB2	Touchdown bearing 2

## Introduction

The highest rotational speeds in rotating machinery can be obtained when the rotor can be rotated freely without mechanical contact with the bearings. This can be achieved by levitating the rotor in a controlled electromagnetic field. In an active magnetic bearing (AMB) supported system, electromagnetic forces levitate the rotor, and the system does not suffer from the wear due to this non-contact operation. AMB systems require continuous active control. Active control enables adjusting the motions of the dynamic system and offers a valuable control system feature during regular operation that is not available with a conventional rotor-bearing system. Therefore, AMBs are the preferred choice in high-speed applications compared to other bearing types.

Although AMBs have many advantages over conventional bearings, they require a safety system for preventing fatal failures in case the electromagnetic field disappears due to an electric short circuit or a fault in the control system. An example of a high-speed electric motor using an active magnetic bearing system is shown in Fig. 1.1. The system has two radial AMBs and an axial AMB, and two touchdown bearings at each end of the rotor. In a rotor dropdown, the touchdown bearings act as a safety device and support the rotor. The touchdown bearings are also known as auxiliary bearings, backup bearings, or safety bearings. The touchdown bearings have to endure a high collision and friction force during the dropdown.

### 1.1 Motivation for the study

An AMB system has several advantages over the conventional rotor-bearing systems. The AMB systems are wear less, have low maintenance costs, they do not need lubrication and can be considered as a favorite choice for applications

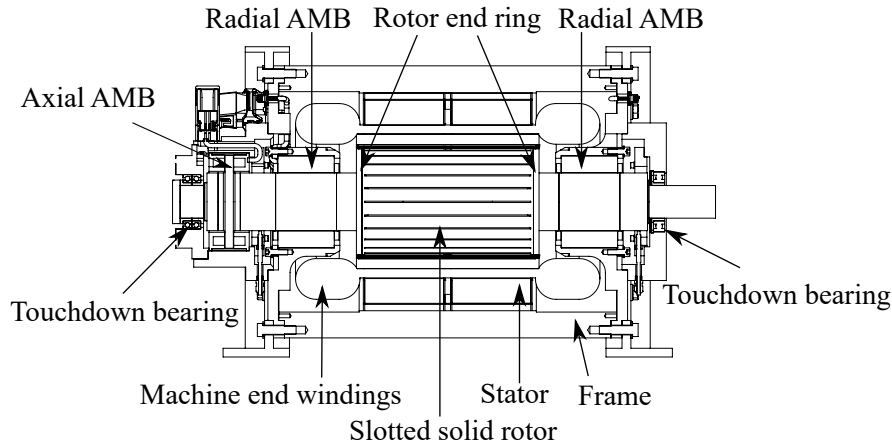


**Figure 1.1.** Schematic of the AMB supported rotor

where contaminated oil is not allowed for safety and environmental reasons. During the last decades, there has been a great deal of effort in the development of magnetic suspension systems. The earliest patents in the development of the magnetic bearing was date back to the fifties. Jesse Beams performed one of the earliest works on AMBs during the second world war. In 1941 Beams and Holmes had a patent on the suspension of rotatable bodies [5]. In 1973, Habermann dealt with the patent on magnetic bearing block device for supporting a vertical shaft adapted for rotating at high speed [14]. Since then, several patents have been documented by Habermann, Loyen, Joli and Aubert (1974), Habermann and Brunet (1977), Habermann, Brunet and LeClère (1978), Meeks and Crawford (1992), respectively [17, 15, 16, 39]. This trend in the growth of AMB technology in the last century shows that the development process required a tremendous effort until gaining acceptance in industrial applications, and up to this date the development is still in progress.

In the design of AMB supported rotors, it is important to ensure that the touchdown bearing can tolerate the load in a dropdown. Therefore, it is essential to evaluate the contact load and stress in the touchdown bearing. However, few studies can be found presenting the stress in touchdown bearings, assuming that the bearing is in an ideal condition and the dimensional errors are not taken into account. Despite considerable development in the manufacturing of ball bearings, a dimensional error such as an off-sized ball can exist in the touchdown bearing. This imperfection during the operation of a conventional rotor bearing can cause the vibrations at cage speed and its harmonics.

In addition, the friction between the rotor and the touchdown bearing and also the internal friction in the bearing can increase the temperature inside the bearing.

If the heat generation is accumulated in the bearing and is not appropriately removed from the bearing, the temperature in the bearing can rise and this might lead to excessive deformation or local stress of the bearing components and consequently, a bearing failure might occur. Therefore, the importance of thermal analysis to the performance of the bearing cannot be neglected. Furthermore, the surface waviness resulting from the wear between the rotor and the touchdown bearing in the previous dropdown of a rotor can affect the performance of the touchdown bearing, which has not been addressed in previous studies.

Apart from this, industrial AMB machines generally do not have force sensors for touchdown bearings, and the systems are only equipped with position sensors to record rotor displacement. Therefore, it is not easy to evaluate the severity of the touchdown bearing load during the dropdown. The API 617 [3] standard regarding touchdown bearings states that the touchdown bearing shall withstand an agreed number of coast downs from trip speed without a need for replacement or refurbishment of the bearing (at least two dropdowns). According to ISO 14839-4 [29] the number of safe dropdowns should be agreed upon between the vendor and the customer, and the number of safe dropdown depends on the application. Determining the severity of a dropdown is on going research and it is not straightforward to find precise instruction in this case.

## 1.2 Dynamic and thermal model of a touchdown bearing

Even though there has been a considerable advancement in rolling bearing technology, several cases of thermal failures of bearings have been reported [7, 54]. The reported failures were due to the rapid growth of the thermal-induced preload and high-temperature gradient in the bearings. This type of failure can occur even without a considerable change in the vibration levels [54]. Numerous publications have implemented an equivalent electrical circuit to study the heat transfer in touchdown bearings [51, 52, 36, 59, 32]. Takabi and Khonsari [53, 54] developed an experimental setup to evaluate the temperature in conventional ball bearings. The experimental setup enabled them to investigate the variation of temperature under different speeds and operating conditions.

Due to the complicated geometry of the bearing assembly and the change in the heat generation rate, some simplifications for the boundary conditions and the model might be required. Accordingly, the results of an analytical solution might be slightly different from the experimental results [31]. In addition to single-row bearings, thermal analyses of double-row bearings have been carried out. Yan et al. [58] and Ai et al. [1] performed a thermal analysis of a double-row tapered roller bearing. Jin et al. [32] compared the thermal structure of single-decker and double-decker touchdown bearings. They concluded that the double-decker configuration reduces the temperature rise in the touchdown bearing.

The aforementioned studies on thermal models of touchdown bearings presume that the bearing is in an ideal condition. However, as a result of surface waviness, particularly due to the wear between the rotor and touchdown bearing in the previous dropdown of the rotor, the friction torque and the power loss calculated for the thermal model of the touchdown bearing can be different from the ideal condition of the bearing.

### 1.3 Surface waviness in touchdown bearings

There are numerous studies about bearing waviness in conventional ball bearings. Zhuo et al. [60] evaluated the influence of applied load, internal clearance, the number of balls as well as the surface waviness on the kinematic behavior of a double-row of self-aligning ball bearings. They described the vibration characteristic of the rotor-bearing system including the surface waviness in the bearing races. The influence of the surface waviness on the stability of a rigid rotor supported by ball bearings is presented in a paper by Harsha and Kankar [24]. They showed that the nonlinear vibration response of a rotor-bearing system due to the surface waviness in the bearing system is highly affected by the number of balls and order of waviness. In addition, they pointed out that by increasing the number of balls, the stiffness of the system is higher and the influence of ball pass frequency decreases. Wardle [56, 57] conducted both a numerical and experimental study on the vibration analysis of the bearings with surface waviness. The study by Changqing and Qingyu [8] on the effect of internal clearance and waviness includes the high-speed effect in the bearing, and their work indicated that waviness causes a change in the main frequencies of the bearing. Liu et al. [37] developed a multibody dynamic model for a ball bearing. They found that as a consequence of the high-speed effect in the bearing, the waviness in the outer race has a higher influence on the vibration of the system rather than the waviness in the inner race.

The aforementioned publications on the surface waviness in bearings mainly discuss the influence of surface waviness, numerically. A recent paper by Heikkinen et al. [26] evaluates the vibration analysis of a spherical roller bearing from surface waviness both experimentally and numerically. Few studies have focused on the influence of the waviness in touchdown bearing applications. Recently, Halminen et al. [18, 19] developed a multibody model of a touchdown bearing. They investigated the effect of 1st, 2nd, and 3rd order surface waviness of the bearing races on the calculation of the friction loss of a touchdown bearing. The above mentioned study applied a multibody model for the touchdown bearing and the thermal model of the bearing was not included. It should be possible to achieve further improvements in the touchdown bearing designs by considering the influence of the surface waviness in a dynamic and thermal model of the

touchdown bearing.

#### 1.4 Stress in touchdown bearing with off-sized ball

For the design aspect of a touchdown bearing, it is important to identify the stress imposed on the bearing and ensure that the bearing can tolerate the stress in the dropdown. For this reason, it is essential to conduct studies on the contact stress in the touchdown bearing. Sun [51] estimated the fatigue life of touchdown bearings. He evaluated the Hertzian contact stresses and used the Lundberg-Palmgren method to approximate the fatigue life of the bearings. The drawback in the selected method was that the Lundberg-Palmgren method was applicable mainly for steady-state loading conditions, while in touchdown bearings the load is time-varying. After few years, Lee and Palazzolo [36] applied the rainflow analysis to consider the time-varying stress for evaluating the fatigue life of touchdown bearings. To evaluate the stress in touchdown bearings, the load distribution and the contact forces in the touchdown bearings should be studied.

Additionally, a dimensional error might occur in various types of bearings, including touchdown bearings. Despite recent developments in the manufacture of high precision ball bearings, identical balls are hard to be produced and there is a possibility that the diameter of the balls might have some deviation from the nominal size. Balls with this defect are known as off-sized balls. Available scientific knowledge on the stresses in touchdown bearings generally assumes that the bearing is in an ideal condition and dimensional errors are rarely taken into account. The size deviation changes the contact force, which consequently can affect the dynamic performance of the bearing. The static and dynamic analyses of off-sized balls in conventional ball bearings have been discussed in the literature. Gupta [13] studied the effect of off-sized ball dimensions and showed that when the deviation of an off-sized ball increases beyond the tolerance limit, the circular shape of the orbit of the ball changes to a polygonal shape. Vibration response of the off-sized balls can be characterized by the cage frequency and its harmonics [2, 23].

There are a few papers available about the stress in touchdown bearings assuming the bearing is in an ideal condition and the dimensional error caused by off-sized balls is not taken into account. In addition, the numerical model for calculating the force and stress in the touchdown bearing can be improved by considering the dropdown test data and the real condition of the machine.

#### 1.5 Dropdown test and touchdown bearing force

A comparison between the simulation results and dropdown test data contributes to developing a more accurate simulation model. The numerical and experimental

study by Schmied and Pradetto [47] on the dropdown of a one-ton rotor is a well-known piece of research in this field and reported that the whirling during a dropdown can be mitigated by applying a corrugated ribbon, low inertia of the inner ring, as well as low friction. They pointed out that the time lag in the controller and the existence of the electromagnetic force at the start of dropdown might cause a deviation between the simulation results and dropdown test data. The dynamic properties of the corrugated ribbon damper are discussed in the paper by Jarroux et al. [30].

The backward whirling of the rotor can be a reason for the damage in rotating machines, the dry friction backward whirling has been studied in the comprehensive study of Bartha [4]. Raju et al. [46] pointed out that when the rotor is balanced well, the dropdown will not begin with a high whirling, whereas for a high magnitude of the unbalance the backward whirling can appear. The study of Hawkins, Imani, and Prosser [25] on the dropdown test of the AMB supported expander/generator indicates that by increasing the unbalance, the rotor can experience full whirling.

In the literature, the comparison of the rotor orbit in a dropdown test was used for the verification of simulation results [48, 55]. Fonseca et al. [10] conducted a numerical and experimental study on the behavior of the rotor dropdown. They studied the nonlinear behavior in a dropdown due to rotor unbalance and presented the rotor orbit for three levels of unbalance. They showed that for low unbalance values, the rotor oscillates in the bottom of the touchdown bearing whereas with a high unbalance value the rotor bounces from contact and impacts the bearing strongly. Helfert et al. [27] studied the acceleration behavior of cageless ball bearings during rotor dropdown. They applied a high-speed video recording in their experiment to capture the interaction of the rotor and touchdown bearing. A few studies can be found documenting the touchdown bearing force through measurements. Fumagalli [11] studied the touchdown bearing force using the measured acceleration in the vertical direction. In a paper by Jarroux et al. [30] different contact models in the simulation of a dropdown were demonstrated. They also performed a dropdown test and measured the touchdown bearing force and presented the normalized bearing force and orbit against the measured results.

## 1.6 Objective and scope of the dissertation

The main objective of the present study is to extend and provide a comprehensive study of a dropdown simulation using a numerical model and dropdown test. With this goal the specific objectives and the scope of the study can be expressed as follows:

- To study the stress in the touchdown bearing arising from the contact of

the rotor and bearing. The effect of the dimensional deviation, off-sized ball, is evaluated. The effect of the location and dimensions of the off-sized ball are studied (*Publication I*).

- The research work presented in this dissertation aimed at developing a dynamic and thermal model of touchdown bearings (*Publication II*). For this purpose, an equivalent electrical circuit model of the bearing is applied. The study presents the touchdown bearing model, bearing kinematics, spinning loss, and the friction heat and power loss in the dropdown. During the lifetime of the bearing the surface quality can degrade, the effect of the magnitude and order of the surface waviness on the temperature rise of the touchdown bearing is taken into account.
- In the present work, a dropdown test was conducted in the case study of a rotor. The main purpose of the study is to compare the simulation results with the measurement data and illustrate how the measurement data provides insights for the further improvement of the dropdown model (*Publication III*). The study on the system is continued, and the measurement data are integrated with a dropdown simulation. Using model-based approach, the forces in the touchdown are estimated and the rotor behaviour in four different dropdowns are compared (*Publication IV*).

## 1.7 Limitations

The stress in the touchdown bearing was studied using a numerical method. The dynamic and thermal model of the touchdown bearing was studied numerically. Investigating the thermal effect in the touchdown bearing in the case study of an electrical motor was validated by comparing the results with the relevant literature. In this dissertation, the dropdown test carried out on the case study of a generator rotor. A direct comparison of the numerical simulation and the dropdown test was not possible. One obstacle is that it is not possible to obtain detailed information about the exact value of all the parameters especially if the parameter is not measured. In addition, at the start of the dropdown test, the electromagnetic field might affect the recorded behavior. The comparison of the rotor orbits in the simulation and measurements were used for verifying the results. Validating the numerical value of the bearing force requires establishing a setup for force measurement and this was not possible because the machine was an industrial application and no change in the initial configuration of the machine was desired.

## 1.8 Scientific contributions

In this dissertation, a dynamic and thermal model of a touchdown bearing is developed and the dimensional error is also taken into account. The measurement data were integrated with a simulation and can be used for further analysis of a touchdown bearing. The scientific contributions of the study can be summarized in four categories in publications I, II, III, and IV.

The current state of the art introduces stress calculations for the bearing with an ideal bearing, and *Publication I* extends the current scientific knowledge by introducing a dimensional deviation component to the simulation. This study applies the Hertzian contact model to feature the stresses in the dropdown and evaluates how dimensional non-ideality such as an off-sized ball can affect the stress distribution in the touchdown bearing. In case of an off-sized ball or balls, the load distribution in the bearing can deviate from the contact load in the bearing with ideal dimensions and consequently affects the stress in the bearing. The effect of the location and number of off-sized balls on the contact stress, as well as the effect of the degree of deviation from nominal size, are evaluated.

*Publication II* aims to develop a dynamic and thermal model for a touchdown bearing and evaluates the friction loss, heat generation, and temperature rise of the touchdown bearing. The thermal expansion of the bearing components is taken into account. The influence of friction heat generated in the touchdown bearing due to different amplitudes and orders of surface waviness in the bearing rings is investigated. This work also presents the effect of the waviness on the temperature rise in the bearing during a rotor drop.

*Publication III* presents an experimental and numerical study on the dropdown of a generator rotor in a two-stage radial gas turbine. In the simulation, the contact force and contact stress in the touchdown bearing are studied. The comparison between the measured and the simulated results provides an insight for further development of the touchdown bearing model that is continued as *Publication IV*.

*Publication IV* compares dropdowns with respect to each other without the need to modify the original configuration of an industrial machine for force measurement. A comparison of the dropdowns with respect to each other can assist condition monitoring teams to investigate the condition of a machine and carry out further analysis to determine a safe dropdown. To compare relatively dropdowns, the maximum Hertzian stress in different dropdowns was selected as a criterion to compare different dropdowns and was analyzed using a statistical method. A model-based approach was used and the measurement data were integrated with the simulation model. The support properties were estimated using an equivalent single mass model. The simulation model was tested for the dropdown test at four different speeds. Apart from this, the FFT was used to study the speed

---

dependence and the constant frequencies found in the measured data. The critical speed map was used to confirm the bending frequencies of the rotor settled in the touchdown bearing and the estimated support properties.



## A thermomechanical model of a touchdown bearing

This chapter demonstrates a dynamic and thermal model of a touchdown bearing. In the model, the friction heat and the thermal expansion of the bearing components during a dropdown are taken into account. In the dropdown model, the FEM (finite element method) is used for the rotor model. This chapter starts with a brief description of the rotor model. Then, the touchdown bearing model is explained. The process for performing the thermomechanical model of the touchdown bearing will be shown. Two kinds of non-ideality in the touchdown bearing are studied; the waviness imperfection and off-sized ball.

### 2.1 Model of a rotor

The FEM model of a rotor was constructed based on the shear deformable Timoshenko beam element by Nelson [41]. The equation of motion of the system can be written as:

$$\mathbf{M}\ddot{\mathbf{q}} + (\mathbf{C} + \omega\mathbf{G})\dot{\mathbf{q}} + (\mathbf{K} + \dot{\omega}\mathbf{G})\mathbf{q} = \omega^2\mathbf{Q}_1 + \dot{\omega}\mathbf{Q}_2 + \mathbf{F} \quad (2.1)$$

where,  $\mathbf{M}$  is the mass matrix,  $\mathbf{C}$  is damping matrix and  $\mathbf{K}$  represents the stiffness matrix. The gyroscopic matrix is denoted by  $\mathbf{G}$ . The vector of the generalized coordinate is shown by  $\mathbf{q}$ . The vector  $\mathbf{Q}_1$  represents the rotor unbalance for the constant rotation speed, and for the non-constant rotational speed of the rotor is shown by  $\mathbf{Q}_2$ . The vector of externally applied force is denoted as  $\mathbf{F}$  and  $\omega$  is the angular rotation speed of the rotor.

## 2.2 Model of a touchdown bearing

The touchdown bearings are simulated according to the model for a ball bearing presented by Sopenan and Mikkola [50]. The radial displacement of the inner ring in the direction of ball  $j$  can be expressed as:

$$e_j^r = e_x \cos \beta_j + e_y \sin \beta_j \quad (2.2)$$

The axial displacement of the inner ring at ball  $j$  is:

$$e_j^t = e_z - (-\psi_x \sin \beta_j + \psi_y \cos \beta_j) (R_{in} + r_{in}) \quad (2.3)$$

where  $e_x$ ,  $e_y$  and  $e_z$  are the relative displacements between the bearing races along the main axes. The index  $j$  represents the ball number.  $\beta_j$  is the azimuth angle of the  $j^{th}$  ball. In Fig. 2.1, the inner race radius and inner race groove radius are denoted as  $R_{in}$  and  $r_{in}$ , respectively. Similarly, for the outer ring they are shown as  $R_{out}$  and  $r_{out}$ , respectively. The misalignment of the inner race in the principal directions are denoted as  $\psi_x$  and  $\psi_y$ . The distance between the bearing rings is given by:

$$d_j = r_{out} + r_{in} - \frac{(R_{in} + \epsilon_{in}) + r_{in} + e_j^r - (R_{out} + \epsilon_{out}) + r_{out}}{\cos \varphi_j} \quad (2.4)$$

where the contact angle is denoted as  $\varphi_j$ :

$$\varphi_j = \arctan \left( \frac{e_j^t}{R_{in} + \epsilon_{in} + r_{in} + e_j^r - R_{out} - \epsilon_{out} + r_{out}} \right) \quad (2.5)$$

where  $\epsilon_{in}$  and  $\epsilon_{out}$  are the thermal expansion of the inner race and outer race, respectively. In a dropdown, the contact angle,  $\varphi_j$ , can be slightly different from the nominal contact angle of the bearing presented in the bearing catalog.

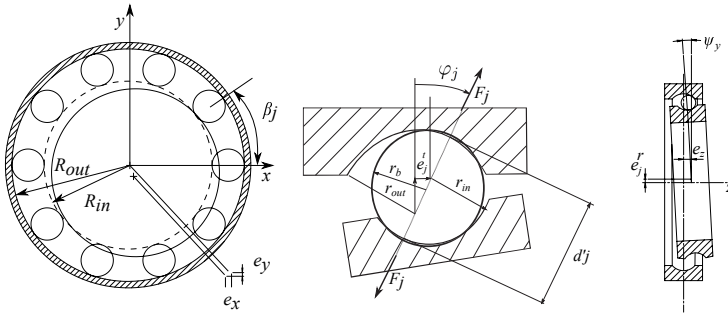


**Figure 2.1.** Cross-section of the ball bearing.

The total elastic deformation of the bearing race is as follows:

$$\delta_j^{tot} = 2r_b + \epsilon_b - \acute{d} \quad (2.6)$$

where  $r_b$  is the ball radius and  $\epsilon_b$  is the thermal expansion of the balls. In the case of a touchdown bearing with an off-sized ball, the ball diameter can be different for each ball.

Then, the contact force between the ball  $j^{th}$  and inner race can be obtained using Hertzian contact theory [21]:

$$F_j = K_c^{tot} \left( \delta_j^{tot} \right)^{3/2} \quad (2.7)$$

where  $K_c^{tot}$  is the total contact stiffness.

### 2.2.1 Model of the contact

The radial contact force between the rotor and touchdown bearing is calculated based on the nonlinear contact model introduced by Hunt and Crossley [28]:

$$F_r = \begin{cases} K\delta^{n^*} + b\delta^{n^*}\dot{\delta} & e_r > c_r \text{ and } F_r > 0 \\ 0 & e_r \leq c_r \text{ and } F_r \leq 0 \end{cases}, \quad (2.8)$$

where  $K$  represents the contact stiffness between the rotor and inner race, and  $n^*$  is a constant dependent on the type of contact (for the contact between the rotor and touchdown bearing  $n^* = 10/9$ ) and  $\dot{\delta}$  is the velocity of penetration of the rotor in the touchdown bearing. The damping parameter,  $b$ , can be related to the coefficient of restitution. Hunt and Crossley [28] showed that  $b = \frac{3}{2}\lambda K$  and they pointed out that the contact parameter  $\lambda$  ranged between 0.08 and 0.32 sec/m can be reasonable. If  $\lambda$  is very low, the material will be very resilient. On the other hand, a very large value of  $\lambda$  such as 0.64 sec/m can raise questions in the assumption for deriving  $b = \frac{3}{2}\lambda K$  and might not be appropriate. In the present study the contact parameter  $\lambda$  equal to 0.08 was selected based on the literature on the simulation of the dropdown [52]. The penetration of the rotor in the inner race can be obtained as:

$$\delta = e_r - c_r + \epsilon_{in} \quad (2.9)$$

where the radius of the air gap between the rotor and touchdown bearing is denoted as  $c_r$ . The radial displacement of the rotor can be calculated as follows [33]:

$$e_r = \sqrt{e_{x,r}^2 + e_{y,r}^2} \quad (2.10)$$

where the radial displacement between the rotor and the inner race along the  $x$  and  $y$ -axis are denoted as  $e_{x,r}$  and  $e_{y,r}$ . The mechanical model for the interaction of

the rotor and touchdown bearing is shown in Fig. 2.2 where,  $K_b$  is bearing stiffness,  $K_{sup}$ , and  $C_{sup}$  represent the support stiffness and damping. The damping of the bearing  $C_b$  typically ranges  $(0.25-2.5) \cdot 10^{-5} K_b$  [34]. The support stiffness and damping parameters can be obtained experimentally or using FEM analysis.  $\omega_i$  and  $\omega_r$  represent the angular velocity of the inner race and rotor, respectively. Here,  $F_r$  and  $F_\mu$ , are the normal and tangential force in the contact of the rotor

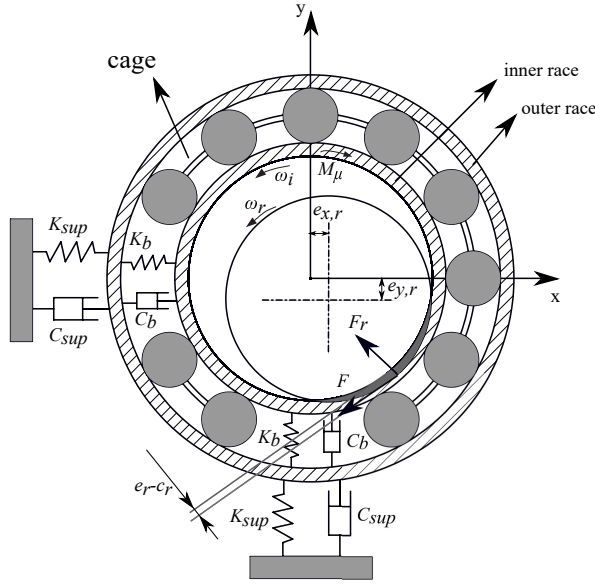


**Figure 2.2.** Mechanical model for the interaction of the rotor and touchdown bearing.

and touchdown bearing. The friction force between the rotor and inner race is:

$$F_\mu = \mu F_r \quad (2.11)$$

where  $\mu$  is the friction coefficient between the rotor and inner race. In this study, the friction is modeled by combining the Coulomb, Stribeck and static friction. The friction force is modeled as the function of the relative speed between the rotor and the touchdown bearing as shown in Fig. 2.3. Friction force creates a torque against the direction of rotation as follows:

$$M_\mu = F_\mu r_s \quad (2.12)$$

where  $r_s$  is the shaft radius. For more information about different friction models please see Olsson et al. [43].

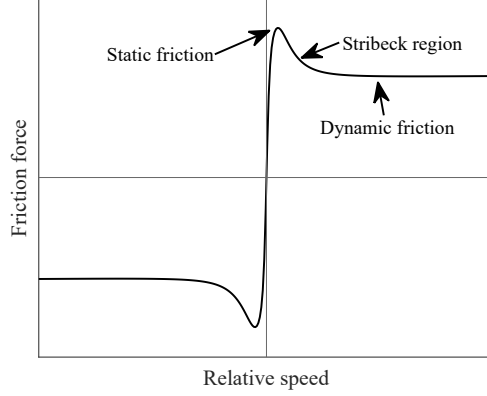


**Figure 2.3.** Friction model for the interaction of the rotor and touchdown bearing.

### 2.2.2 Modeling of surface waviness

The waviness imperfection refers to the dimensional irregularity where the bearing surface periodically deviates from the nominal dimensions. It can influence the total elastic deformation of the bearing race. Consequently, it can change the contact force in the touchdown bearing. The surface waviness in the bearing can be modeled using the sinusoidal function. Then, the elastic deformation of the bearing race (eq. 2.6) can be rewritten as [49]:

$$\delta_j^{tot} = 2r_b + \epsilon_b - \acute{d} + \sum_{N_w=1}^n A_m^{in} \sin(m_{in}(\beta) + \theta_{irw}) + \sum_{N_w=1}^n A_m^{out} \sin(m_{out}(\beta) + \theta_{orw}) \quad (2.13)$$

where,  $m_{in}$  and  $m_{out}$  are the waviness orders for the inner ring and outer ring, respectively.  $\beta$  is the azimuth angle (Fig. 2.4).  $A_m^{in}$  and  $A_m^{out}$  are the amplitudes of the  $m^{th}$  waviness order in the inner ring and outer ring, respectively. Here,  $\theta_{irw}$  and  $\theta_{orw}$  are the phase angles of the  $m^{th}$  waviness order of the inner race and outer race, respectively. The number of waves is denoted as  $N_w$ . The surface waviness in the bearing can be a combination of the different waves ( $n$ ).

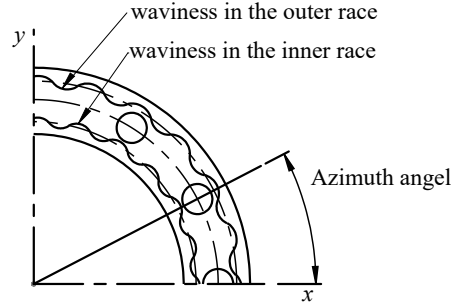


Figure 2.4. Model of surface waviness in bearing races.

### 2.2.3 Thermal model of a bearing

In the touchdown bearing, heat transfers by both conduction and convection mechanisms. The friction between the rotor and the inner race, and also the friction between the ball and bearing races, are considered as generating heat sources. Fig. 2.5 shows a schematic of the equivalent electrical circuit of the bearing model. Here,  $d_e$ ,  $d_h$ ,  $d_i$ ,  $d_o$ ,  $d_s$ ,  $d_m$ , and  $W$  are the dimensions of the bearing that can be found in the bearing catalog and the drawings of the case study.  $H_i$ ,  $H_o$  and  $H_r$  represent the heat generation in the inner ring, outer ring, and in the contact of rotor and touchdown bearing, respectively, and these will be described in section 2.2.4. The thermal resistances ( $R_{1-9}$ ) are summarized in Table 2.1. Here,  $T_b$ ,  $T_i$ ,  $T_o$ ,  $T_s$ ,  $T_h$  are the temperatures of the ball, inner ring, outer ring, shaft, and housing, respectively. Temperatures in the contact of ball/inner ring and ball/outer ring are denoted as  $T_{ci}$  and  $T_{co}$ , respectively.

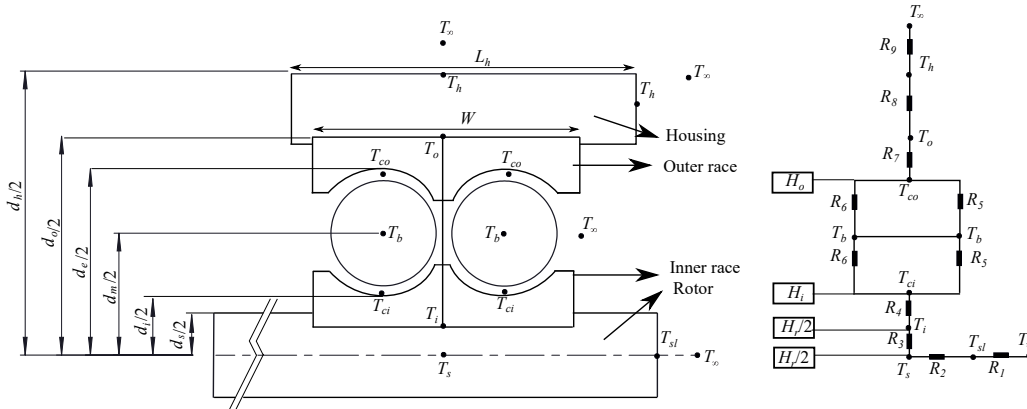


Figure 2.5. Equivalent electrical circuit model of the bearing.

The following equation represents the coefficient of free convection heat transfer

**Table 2.1.** Thermal resistances of bearing elements [59].

Shaft/Inner race	Ball/ambient	Outer race	Housing
$R_1$ convection	$R_5$ conduction	$R_7$ conduction	$R_8$ conduction
$R_2$ conduction	$R_6$ convection		$R_9$ convection
$R_3$ conduction			
$R_4$ conduction			

from the bearing housing [21]:

$$h_h = 23(T - T_\infty)^{0.25} \quad (2.14)$$

where  $T$  is temperature and  $T_\infty$  is the ambient temperature. The heat transfer balance should be satisfied in each node of the model [59].

$$H_{in} - H_{out} = \rho CV \frac{dT}{dt} \quad (2.15)$$

where  $H_{in}$  and  $H_{out}$  are input and outflow heat, respectively.  $C$  is the specific heat,  $\rho$  is the density, and  $V$  is the volume. The temperature gradient is denoted as  $\frac{dT}{dt}$ . In a discrete form, the thermal balance in the bearing can be written as [32]:

$$\mathbf{M}_{brg} \mathbf{C}_{brg} (\mathbf{T}^{t+\Delta t} - \mathbf{T}^t) = (\mathbf{H}_{in}^t - \mathbf{H}_{out}^t) \Delta t \quad (2.16)$$

where  $\mathbf{M}_{brg}$  is the lumped mass matrix and  $\mathbf{C}_{brg}$  is a matrix form of the specific heat for the bearing model. The input heat flux and output heat flux are denoted as  $\mathbf{H}_{in}^t$  and  $\mathbf{H}_{out}^t$ , respectively. The temperature in the new time step  $\mathbf{T}^{t+\Delta t}$  can be calculated by the temperature in the previous time step  $\mathbf{T}^t$ .

#### 2.2.4 Power loss in a touchdown bearing

The power loss resulting from the contact between the rotor and the inner race can be expressed as follows [32]:

$$H_r = F_\mu V_{rel} \quad (2.17)$$

where  $V_{rel}$  is the relative velocity between the rotor and the inner race and  $F_\mu$  is the friction force between the rotor and the touchdown bearing. The second part of the power loss is due to friction between the balls and the bearing races. The equation that expresses the global friction in the bearing ( $M^*$ ) is as follows [21]:

$$M^* = M_L + M_v \quad (2.18)$$

The load-dependent term is given by [44]:

$$M_L = f_1 P d_m \quad (2.19)$$

where  $P$  is the equivalent load of the ball bearing. The velocity-dependent term can be calculated by [44]:

$$\begin{cases} M_v = 10^{-7} f_2 (\nu^* N^*)^{2/3} d_m^3 & \nu N^* > 2000 \\ M_v = 160 \times 10^{-7} f_2 d_m^3 & \nu N^* \leq 2000 \end{cases}, \quad (2.20)$$

where  $f_1$  and  $f_2$  are factors dependent on the design and the load on the bearing,  $\nu^*$  is the kinematic viscosity (centistoke) and  $N^*$  is the speed of the inner race (rpm) and  $d_m$  is the pitch diameter (mm). In high-speed applications, the spinning torque, as a consequence of the spinning movement of the individual balls around its axis, can be considered as one of the sources of the friction generated in the bearing. The spinning torque in the inner ring can be expressed as follows [45]:

$$M_{si} = \frac{3\mu F_j a^* \zeta}{8} \quad (2.21)$$

where  $\mu$  is the friction coefficient,  $F_j$  is the contact force given in equation 2.7, and  $a^*$  is the semi-major diameter of the elliptic contact in the bearing (eq. 2.30). The parameter  $\zeta$  is the elliptical integral of the second type. The equation that describes the total heat generation at the inner race is as follows [59]:

$$H_{in} = \sum_{j=1} (\omega_b M_{ij} + \omega_{si} M_{si}) \quad (2.22)$$

where  $M_{ij}$  is the friction torque in the inner race, and  $M_{si}$  is spinning torque,  $\omega_b$  is the angular speed of the ball, and  $\omega_{si}$  is the spinning velocity in the contact of the ball and inner ring.

A similar approach can be applied to obtain the heat generation at the outer race. Applying the instant center of velocity and trigonometry relation, the spinning velocity of the ball can be derived [9]. The angular speed of the ball in the contact area between the ball/inner race ( $\omega_{ci}$ ) and the ball/outer race ( $\omega_{co}$ ) intersect each other at the point  $P$  along the axis of the bearing (Fig. 2.6). In Fig. 2.6a ( $\omega_c$ ) is cage speed. The spinning velocity in the contact of the ball and bearing races is as follows [20]:

$$\begin{cases} \omega_{si} = -\omega_b \sin(\varphi_i - \theta) + \omega_{ci} \sin(\varphi_i) \\ \omega_{so} = \omega_b \sin(\varphi_o - \theta) + \omega_{co} \sin(\varphi_o) \end{cases}, \quad (2.23)$$

where  $\varphi_i$  and  $\varphi_o$  represent the nominal contact angle in the inner race and outer race, respectively.  $\varphi$  is the contact angle when the bearing is under the load. The ball pitch angle is denoted as  $\theta$ :

$$\tan(\theta) = \frac{\sin\varphi}{\cos\varphi_o + d_b/d_m} \quad (2.24)$$

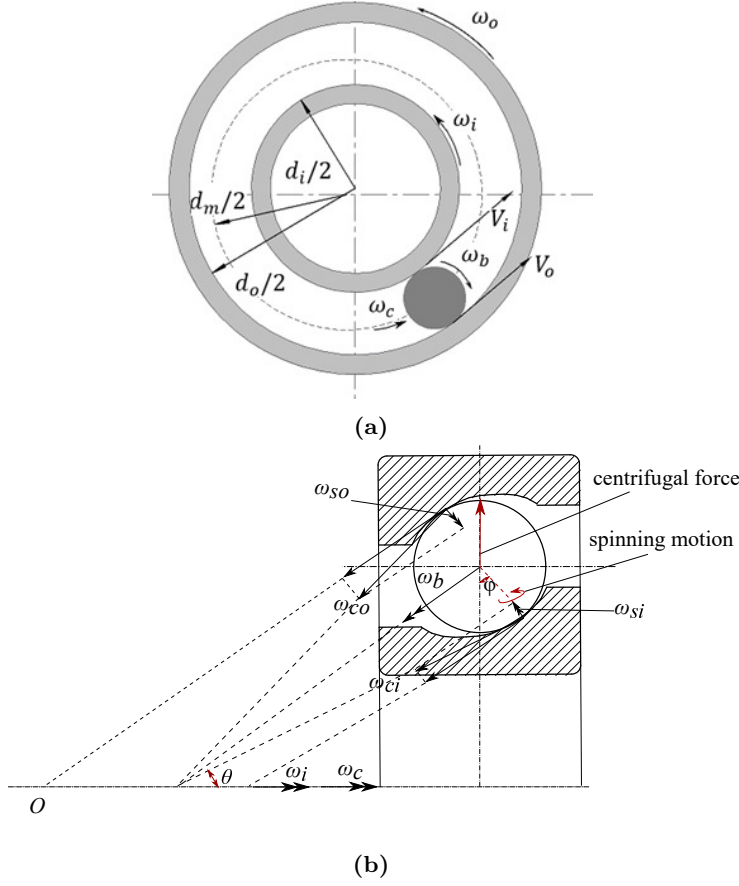


Figure 2.6. Bearing kinematics.

and, the angular speed of the ball can be calculated as follows [42]:

$$\omega_b = \frac{\omega_{co}(d_m + d_b \cos \varphi)}{d_b} \quad (2.25)$$

where  $d_b$  and  $d_m$  represent the ball diameter and pitch diameter, respectively.

### 2.2.5 Bearing deformation under thermal effects

The friction heat generated in the dropdown might cause the thermal expansion of the bearing components. The thermal expansion of the ball and inner race can be calculated as follows [52]:

$$\epsilon_b = \alpha_b r_b \Delta T_b \quad (2.26)$$

$$\epsilon_{in} = \frac{\alpha_{in} (1 + \nu_{in}) r_s}{3 (r_i + r_s)} \left[ \Delta T_{in} (2r_s + r_i) + \Delta T_{ci} (2r_i + r_s) \right] \quad (2.27)$$

The thermal expansion of the outer race is as follows [52]:

$$\epsilon_{out} = \frac{\alpha_{out} (1 + \nu_{out}) r_{out}}{3 (r_{out} + r_h)} \left[ \Delta T_{out} (2r_{out} + r_h) + \Delta T_h (2r_h + r_{out}) \right] \quad (2.28)$$

The radius of the ball, inner race and cross-section of the rotor at the location of the touchdown bearing, outer race and housing are denoted as  $r_b$ ,  $r_i$ ,  $r_s$ ,  $r_{out}$ , and  $r_h$  respectively. The thermal expansion coefficient of the ball, inner race, and outer race are expressed as  $\alpha_b$ ,  $\alpha_{in}$ , and  $\alpha_{out}$ , respectively.  $\nu_{in}$  and  $\nu_{out}$  are the Poisson's ratio of the inner race and outer race, respectively. The temperature growth of the ball, inner ring, outer ring, housing, and the contact area of the ball/inner ring are denoted as  $\Delta T_b$ ,  $\Delta T_{in}$ ,  $\Delta T_{out}$ ,  $\Delta T_h$ , and  $\Delta T_{ci}$ , respectively.

### 2.2.6 Updating the model

There should be a balance between the heat generation inside the bearing and the heat dissipated from the bearing. If the heat dissipation is less than the heat generated inside the bearing, the temperature in the bearing will rise and it can promote the possibility of thermal failure. Therefore, the thermal expansion of the bearing components needs to be considered. A flow chart of the simulation is presented in Fig. 2.7.

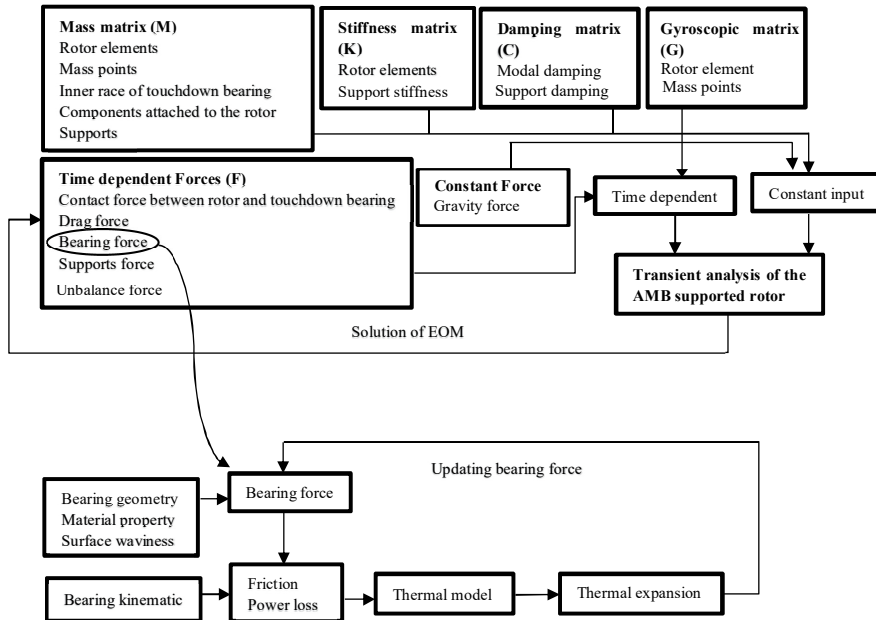


Figure 2.7. Flowchart of a thermomechanical model of a touchdown bearing.

### 2.2.7 Contact stress

According to the Hertzian contact model, the maximum contact stress occurs at the geometrical center of the contact between the ball and bearing race, which can be calculated as follows [22]:

$$\sigma_{max} = \frac{3F_j}{2\pi a^* b^*} \quad (2.29)$$

where  $a^*$  and  $b^*$  are the semi-major/minor axes of the elliptic contact, respectively. The following equations can be used to calculate  $a^*$  and  $b^*$  [12]:

$$a^* = \left( \frac{3\kappa^2 \xi F_j R_e}{\pi E^*} \right)^{1/3}, b^* = \left( \frac{3\xi F_j R_e}{\pi \kappa E^*} \right)^{1/3} \quad (2.30)$$

where,  $R_e$  is contact curvature and  $E^*$  represents the equivalent modulus of elasticity:

$$\frac{1}{E^*} = \frac{1 - \nu_I^2}{E_I} + \frac{1 - \nu_{II}^2}{E_{II}} \quad (2.31)$$

where  $\nu$  and  $E$  represent the Poisson ratio and modulus of elasticity of bodies  $I$  and  $II$  (the ball and inner race). The elliptic eccentricity parameter  $\kappa$  and the elliptic integral of the first kind  $\xi$  can be calculated as follows [6]:

$$\kappa \approx 1.0339 (A/B)^{0.636} \quad (2.32)$$

$$\xi \approx 1.0003 + 0.5968 (A/B) \quad (2.33)$$

where  $A$  and  $B$  are the principal curvatures of contact in the  $x$  and  $y$ -direction [12].



## Integrating dropdown test data with simulation data

Conducting the dropdown test and comparing the measurement data with the simulation results can be considered for further development of the dropdown simulation. The experimental data can be used for estimating unknown parameters, using similar constraints for the model as well as verifying the model. Practically, due to the nonlinear phenomena involved in the dropdown and also limitations in the measurements, this process can be challenging. The prototype studied here and the majority of the AMB machines are equipped with position sensors for the rotor displacement and they do not have the force sensors for touchdown bearings. Therefore, investigating the condition of the touchdown bearings is not straightforward. The present study applies a model-based approach and integrates the measurement data with the simulation model to estimate the touchdown bearing force.

### 3.1 Procedure

Experience of conducting a dropdown test showed that because of the electromagnetic field, the position of the rotor at the start of a dropdown might not necessarily be at the center. A modal expansion was applied to obtain the initial conditions of the rotor based on the measurement data. Furthermore, dissimilarity between the nominal air gap and measurements have been found previously, and the air gaps at both ends of the rotor have also been found to be different. In this study, the air gap value is picked out from the test data and the difference in the air gaps at both ends is considered in the model. The touchdown bearing forces are estimated by integrating the dropdown data with the simulation model and the initial position of the rotor, support properties are studied in details.

The friction coefficient was chosen by sensitivity analysis and the simulation orbit and measurement orbit were compared. The friction coefficient representing the close behavior of the simulation orbit and measurement was selected as the final value for the friction coefficient. To verify the model, the rotor orbits in the simulation and measurements were compared. This provides an explanation that for the level of force estimated, the displacement of the rotor in the simulation are alike measurement data. Figure 3.1 shows a flow chart of the simulation routine.

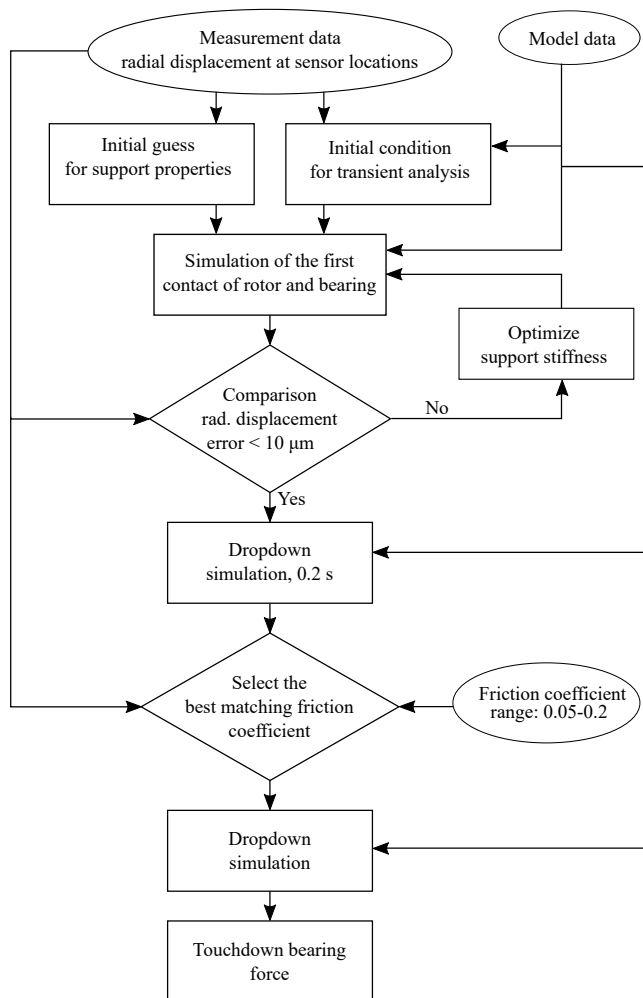


**Figure 3.1.** Flow chart of the estimation of touchdown bearing force.

### 3.2 Initial conditions of the rotor

In the present study, the radial displacements of the rotor near the touchdown bearing location were recorded (two locations at each end of the rotor). However, the dropdown simulation needs to consider the initial displacement and velocity of the rotor over all degrees of freedom. Using a modal expansion the measurable part of the system is in relation to the deformation at all degrees of freedom [38]:

$$\mathbf{r}_m = \mathbf{Q}\mathbf{r}_t \quad (3.1)$$

where  $\mathbf{r}_m$  is the vector of the measured data,  $\mathbf{Q}$  is the measurement matrix and  $\mathbf{r}_t$  is the deformation at all degrees of freedom. The following equation can be used to calculate the deformation at full degrees of freedom, based on the pseudo-inverse:

$$\mathbf{r}_t = \{\Phi [(\mathbf{Q}\Phi)^T(\mathbf{Q}\Phi)]^{-1} [\mathbf{Q}\Phi]^T\} \mathbf{r}_m \quad (3.2)$$

where  $\Phi$  is the reduced mode shape matrix (the number of modes is equal to the maximum number of measurement points). In this case, the reduced mode shape matrix is limited to rigid body modes. In an AMB supported rotor with an operating speed higher than the first critical speed, estimating the initial position with rigid body modes produces satisfactory results because the rotor deformation as a consequence of its flexibility is not significant in comparison to the relative movement of the rotor and bearings. The initial condition for the velocity is calculated with the differentiation of the displacement signal. Noise smoothing and using the average of the velocity signal just after the fall of the rotor might be beneficial to eliminate the noise and find the four measurement points for the velocity. Similarly, using the modal expansion, the velocity in the full degrees of freedom is calculated.

### 3.3 Support properties

Applying the single-mass model depicted in Fig. 3.2 the support properties can be estimated. The time history of the vertical displacement of the rotor limited to the first contact is studied. The equivalent stiffness can be calculated by [47]:

$$\omega_k = \sqrt{K_{eq}/M} \quad (3.3)$$

where  $M$  is the share of the rotor mass at each support and  $\omega_k$  represents the natural frequency of an equivalent system. The damping ratio was chosen from the literature [35].

The equivalent stiffness calculated from the above equation ( $K_{eq}$ ) is the series combination of support stiffness and bearing stiffness. Additional analysis is

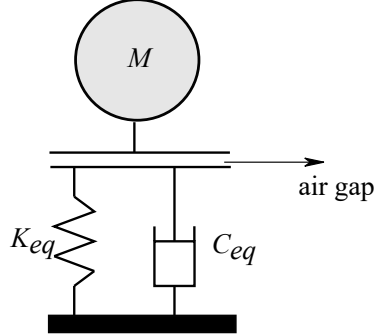


Figure 3.2. Single mass model for support.

needed to separate these components. To simplify the calculation, this work presumes that the support stiffness in the horizontal direction is similar to the vertical direction. The equivalent stiffness properties are used as an initial guess of the support stiffness, whereas the bearings are modeled using the proposed method in section 2.2. To estimate the support properties, the dropdown is simulated to the bounce after the initial contact of the rotor and touchdown bearing. The simulated response is compared with the test data and the least-squares optimization algorithm is used to determine the optimum values for the stiffness, damping, and mass of the supports.

### 3.4 Aerodynamic torque

The measurement data showed that the rotor speed in the dropdown has an exponential profile. In the simulation model, the characteristics of an exponential profile for the rotor speed are extracted from the measurement. Then, the aerodynamic torque in the deceleration of the rotor is as follows:

$$M_{ad} = I_p \dot{n} \quad (3.4)$$

where  $\dot{n}$  is a derivative of the speed of the rotor during deceleration and the polar moment of inertia of the rotor is denoted as  $I_p$ .

## Summary of findings

In this dissertation, three rotor-touchdown bearing systems were selected as case studies. An outline of the results presented in this section is as follows:

- A case study of the dropdown of an electric motor in which the stress in a touchdown bearing with an off-sized ball is evaluated.
- A case study of the dropdown of an electric motor in which the thermal expansion of the touchdown bearing as well as the influence of surface waviness are studied.
- The dropdown of a gas turbine rotor is studied both numerically and experimentally. In the initial phase of the study, the behavior of the rotor in the dropdown test is demonstrated and the simulation results are compared with measurement data. In the second phase, the model has been improved and the touchdown bearing forces in the dropdown are evaluated based on the displacement recorded by position sensors installed in the machine.

### 4.1 Stress in a touchdown bearing

*Publication I* evaluates the stress in a touchdown bearing of an electric motor. The touchdown bearings were deep groove ball bearings type 6016 on both sides. First of all, the maximum Hertzian stress in the touchdown bearings with a nominal diameter was studied and the distribution of the stress for the first, second, and third contact of the rotor and touchdown bearing is presented. Figure 4.1a depicts the distribution of stress during first contact. In the first contact, the balls numbered 7, 8, 9, and 10 penetrate the inner race (Fig. 4.1b). The highest

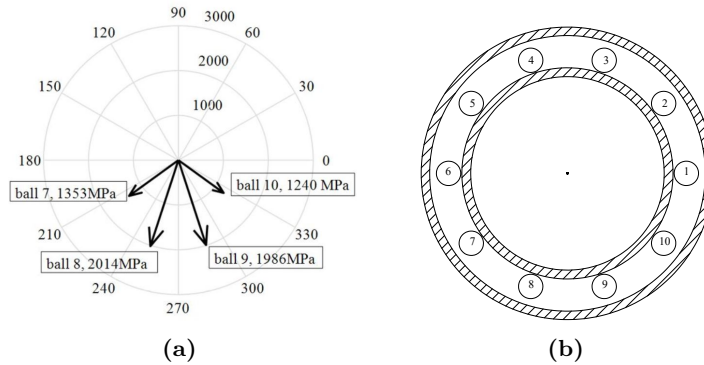


**Figure 4.1.** Distribution of stress a) first contact of the rotor and touchdown bearing b) ball arrangement at the start of the simulation.

stress was experienced in the contact of ball number 8 with the inner race. The contact force between the rotor and inner race has two components. The vertical component is mainly due to the effect of the weight of the rotor. The friction force between the rotor and inner race is in the tangential direction and acts in the opposite direction to the rotation of the rotor (counterclockwise). Therefore, the total contact force between the rotor and inner race is orientated to the left. For this reason, ball 8 experiences a higher contact force than ball 9 and the stress is higher. Figure 4.2 depicts the stress distribution in the second and third contact of the rotor and inner race. In the second and third contacts, ball number 10 is no longer in contact with the inner race and the location of the balls has been changed.

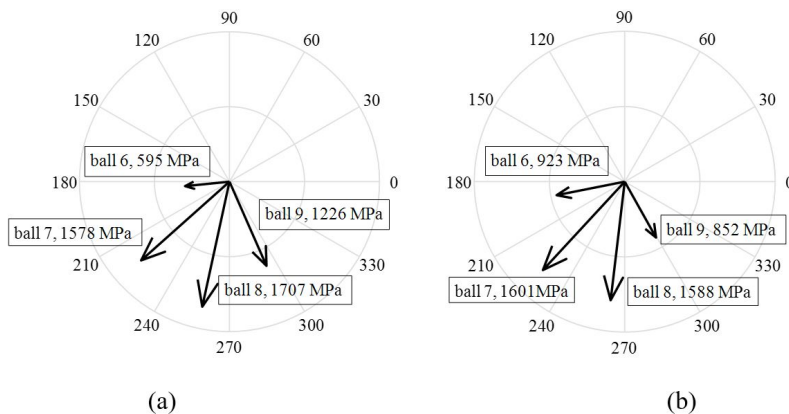


**Figure 4.2.** Stress distribution, (a) second contact (b) third contact.

In the dropdown, the stresses are not uniformly distributed between balls. In

the first contact, the bearing experiences the highest stress. Then, the stresses decrease and the differences in the stresses between the balls gradually are reduced. It is clear that the magnitude of the stress and the location of the ball with the highest stress change with the rotation of the balls in the bearing.

#### 4.1.1 Stress in a touchdown bearing with a single off-sized ball

In this section, the influence of the dimension and location of an off-sized ball on the stress in the touchdown bearing is discussed. It is assumed that the bearing has a single off-sized ball (up to 5  $\mu\text{m}$  greater than nominal diameter), and this ball can be in locations 1-10 of Fig. 4.3b. The effect of the location and size of the single off-sized ball on the contact stress of ball 8 (it has maximum stress) is depicted in Fig. 4.3a. When the off-sized ball is located in an unloaded zone (locations 1-6), the off-sized ball does not significantly affect the stress on ball number 8. When the off-sized ball is in the loaded zone and is far from ball 8 (location 10) there is a small effect on the stress on ball 8 (up to 3  $\mu\text{m}$  for the off-sized ball). When ball 8 itself is off-sized, a clear increase in the stress can be observed. An off-sized ball in locations 7 or 9, causes a reduction in the maximum Hertzian stress for ball 8.

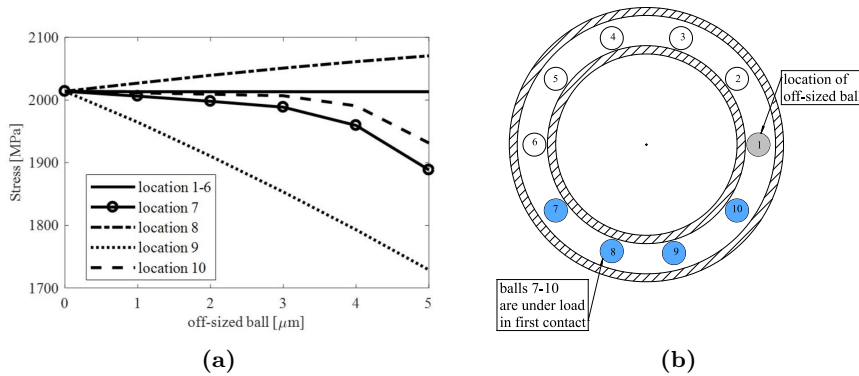


**Figure 4.3.** The effect of the diameter and location of the off-sized ball diameter in the a) stress in ball number 8 during the first contact, b) location of off-sized.

In the case of an off-sized ball in the loaded zone, the load distribution in the bearing is different from the bearing of a nominal size. Initially, the off-sized ball contacts the inner ring. Then, the other balls make contact with the inner ring. When an off-sized ball is in the loaded zone, the off-sized ball experiences a higher load while the other balls carry less load since the total amount of energy transferred in the bearing does not change.

The diameter of an off-sized ball might also be less than the nominal diameter. In this case, first the balls of nominal size contact the inner ring and then the

off-sized ball starts make contact. This causes balls of a nominal size to carry a higher load.

#### 4.1.2 Multiple off-sized balls

To study multiple off-sized balls, it is assumed that the touchdown bearing has three off-sized balls (+5  $\mu\text{m}$ ) located in the arrangements shown in Fig. 4.4. The effects of the stresses on the balls under load (in the first contact) are shown in Table 4.1. When two off-sized balls are located in the unloaded zone (Fig. 4.4a,b), one of the three off-sized balls carries the highest load, and the increase in stress has a similar pattern to the single off-sized ball presented before. When all the off-sized balls are located in the loaded zone (Fig. 4.4c), the difference in the stresses in the balls carrying load becomes even smaller. In this case, balls 8 and 9 carry equivalent stress.

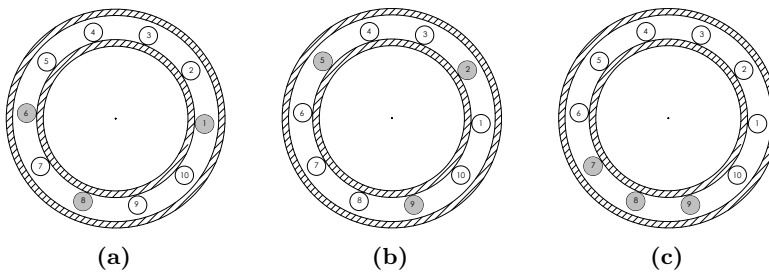


**Figure 4.4.** Studied arrangements of multiple off-sized balls.

**Table 4.1.** Stress in a touchdown bearing with multiple off-sized balls, MPa.

Multiple off-sized balls 5 $\mu\text{m}$				
ball under load	nominal diameter	balls 1, 6, 8	balls 2, 5, 9	balls 7, 8, 9
7	1353	1027	1107	1486
8	2014	2070	1729	1994
9	1986	1697	2047	1991
10	1240	977	890	897

## 4.2 Dynamic and thermal model of a touchdown bearing

*Publication II* investigates a dynamic and thermal model of a touchdown bearing of an electric motor. The influence of surface waviness is also studied. Touchdown bearing 1 is a hybrid deep groove ball bearing of type 6014 HC5/C3, and touchdown bearing 2 is a pair of angular contact ball bearings of type 71914-E-T-PS4 installed

in an X-configuration. The present results describe the dynamic and thermal model for touchdown bearing 2.

#### 4.2.1 Orbital motion of the rotor

The rotor orbit presented in Fig. 4.5 shows that after the initial impact of the rotor with the touchdown bearings, the rotor bounces back up to the height of more than half of the air gap. In order to clearly describe the rotor orbit, the rotor displacement along the main axes is studied in detail.

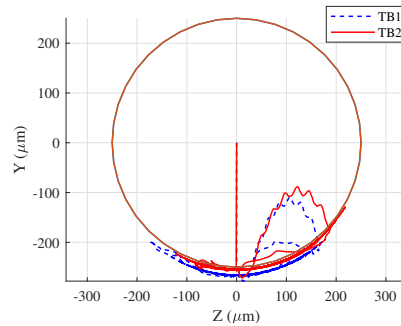


**Figure 4.5.** Rotor orbit (TB1: touchdown bearing 1, TB2: touchdown bearing 2).

This work focuses on studying the horizontal and vertical displacements of the rotor. The axial displacement is constrained. Figure 4.6 shows the displacement of the rotor at the locations of the touchdown bearings. The first hit of the rotor on the touchdown bearings deforms both the bearings and the support, resulting in a higher displacement than the air gap (250  $\mu\text{m}$ ). After the first hit, the rotor lifts off from the inner ring and during the subsequent contacts the displacement in the vertical direction is reduced (Fig. 4.6(a)) and gradually the rotor stabilizes on the bottom of the bearing. The contacts of the rotor with the touchdown bearings can be also seen in the horizontal direction (Fig. 4.6(b)). In this direction, the displacement does not exceed or even closely approach the air gap length. The results indicate a smooth swinging motion on the bottom of the bearing.

Figure 4.7 shows angular velocities of the inner rings of the touchdown bearings. The inner rings of the touchdown bearings accelerate with different rates. This is mainly due to the different bearing types, and different inertia properties. TB1 is a deep groove ball bearing that accelerates faster. After 0.2 s, the tangential velocity of the bearing inner ring equals the tangential velocity of the rotor outer surface. As TB2 (a pair of angular contact bearings) has a higher mass and moment of inertia, the acceleration of TB2 is lower.

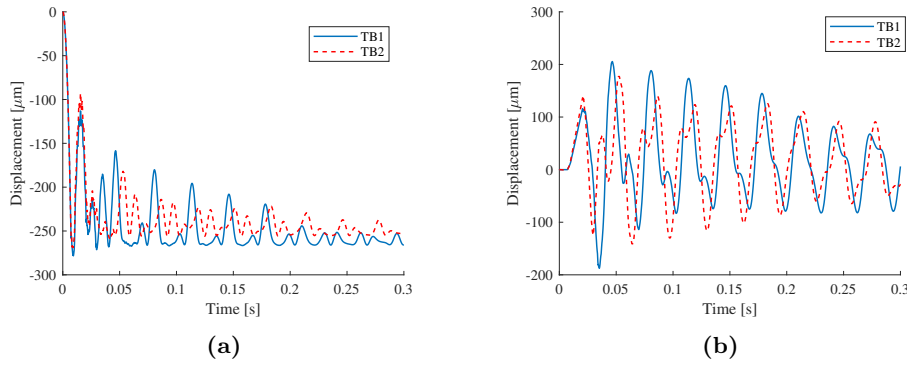


**Figure 4.6.** Rotor displacement a) vertical-direction b) horizontal-direction.

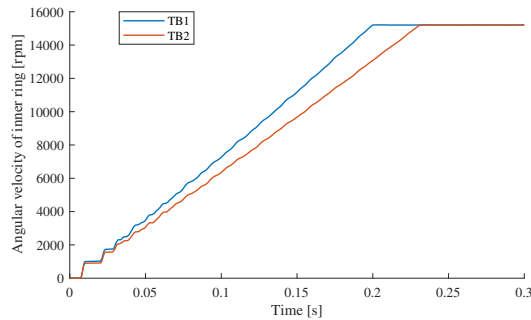


**Figure 4.7.** Angular velocity of the rotor and inner race during dropdown.

#### 4.2.2 Effect of surface waviness

The contact forces and the friction heat generation in the bearing have been evaluated for the cases introduced in Table 4.2. The first case presumes that the bearing has an ideally smooth surface. In cases 2-4, the inner race has a surface waviness with the amplitude of 1  $\mu\text{m}$  and the 1st, 2nd, and 3rd orders of waviness are studied. The last two cases are used to evaluate the influence of a higher amplitude of surface waviness.

**Table 4.2.** Various cases of waviness in the bearing.

	Different cases of surface waviness in bearing, waviness order (Amplitude)					
	Ideal	1st (1 $\mu\text{m}$ )	2nd (1 $\mu\text{m}$ )	3rd (1 $\mu\text{m}$ )	2nd (4 $\mu\text{m}$ )	3rd (2 $\mu\text{m}$ )
Ideal surface of bearing	✓	-	-	-	-	-
Waviness in both races	-	✓	✓	✓	✓	✓
Waviness in contact of rotor	-	✓	✓	✓	✓	✓

### Contact force

Figure 4.8 shows the contact force between the rotor and the bearing inner ring as functions of time. The waviness orders of the first to third orders are studied and compared with the bearing with the ideal surface. The first hit of the rotor on the bearings results in high contact forces exceeding 5000 N. Figure 4.8(b) shows a close zoom of the figure for the time span of 0.025-0.1 s. The figure shows that with a surface waviness of amplitude  $1\ \mu\text{m}$ , the contact occurs in the time close to the bearing with the ideal surface. Eventually, the rotor is in continuous contact with the bearing and the contact force between the rotor and the inner ring gradually settles around 500 N.

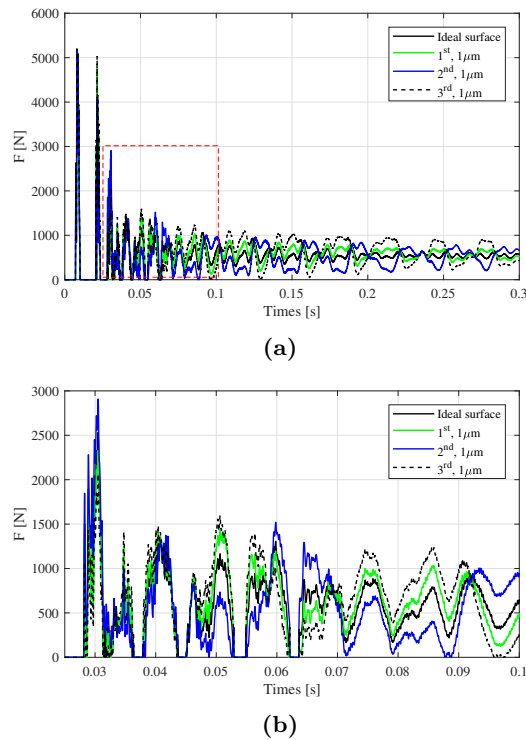


**Figure 4.8.** Magnitudes of the contact forces between the rotor and inner race for a bearing with an ideal surface and a bearing with waviness. a) simulation time 0.3 s, b) zoomed view from 0.025 to 0.1 s.

The waviness affects the variation of the forces when the rotor swings smoothly on the bottom of the touchdown bearing. In the ideal case, the contact force between the rotor and inner ring settles at the level of 500 N. In other cases where any order of bearing waviness is included, the contact force varies below or above the magnitude of the contact force in the ideal bearing (Fig. 4.9). The magnitude of

the variation can be as high as double the stabilized level of the contact force in the ideal case.

The contact forces in the bearing are smoothed evenly in the case of triangular waviness (third order waviness) and in ideal bearings. In cases of first and second order waviness, the contact forces in the bearing vary notably. The reason for such behavior is most likely geometrical. The triangularity of the bearing has a 120-degree phase difference between wave peaks that results in forces that are counteracting each other. In the case of a 180-degree phase difference in the waves, there are no such counteracting forces and the highest force component follows the wave peak traveling in the lower half of bearing ring.

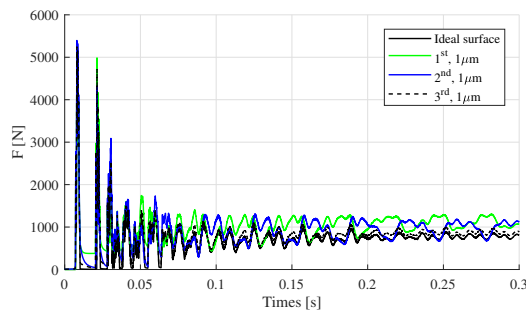


**Figure 4.9.** Magnitude of the bearing force for a bearing with an ideal surface and bearing with waviness.

### Friction torque

Figure 4.10(a) shows the friction torque in a touchdown bearing with an ideal surface. In this case study, the load-dependent friction torque is less than the velocity-dependent friction torque. In the first contact, the load-dependent friction torque has the highest value of about 0.14 Nm. After the second contact, it is reduced and gradually approaches a uniform level. The velocity-dependent term is highly affected by the angular velocity of the inner race and by increasing the angular velocity, the level of viscous friction torque becomes higher.

It is important to mention that applying the empirical equation for the velocity-dependent friction determined by Palmgren [44], equation (2.20), can raise some uncertainties in the calculation of the velocity-dependent term in an oil-free touchdown bearing. The above equation is valid for the case where the bearing operates at moderate speed and does not carry an excessive load, and can be used for the lubricant with the specific gravity of 0.9. Later on, it will be shown that the internal heat generation in the bearing is relatively low compared to the heat generated due to the contact of the rotor and the inner ring. Therefore, applying this empirical equation can still provide reasonable results for the dropdown of the rotor in an oil-free touchdown bearing. Figure 4.10(b) shows that for surface

waviness at an amplitude of 1  $\mu\text{m}$ , the global friction torque has a small variation irrespective of the waviness order, and the effect is negligible.

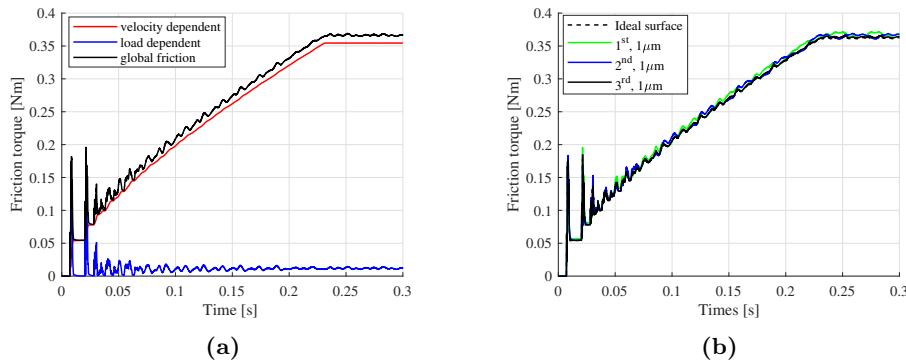


**Figure 4.10.** Friction torque in a bearing a) with an ideal surface b) with global friction torque for an ideal surface and a bearing with 1–3 order waviness at an amplitude of 1  $\mu\text{m}$ .

### Heat generation

Figure 4.11 shows that from the start of the dropdown until 0.2 s, the heat generation increases in both races; after this, it is stabilized around a constant value. In the case of a bearing with an ideal surface, the maximum heat generation in the contact of the outer race is 60 W, which is approximately 10 W higher than the maximum heat generation in the inner race. This figure reveals the heat generation in the bearing races has a similar trend to the acceleration of the bearing race (Fig. 4.7). In addition, for a surface waviness at an amplitude of 1  $\mu\text{m}$ , regardless of the waviness order, the heat generation in the bearing is higher than the bearing with the ideal surface. In the case of 1st waviness, the maximum heat generation in the bearing races is about 10 % higher than the corresponding values for the bearing with an ideal surface. At the same amplitude of surface waviness, for the higher order of waviness (2nd, 3rd), the differences in the heat generation of the bearing with surface waviness and the ideal surface are reduced to approximately 7 % and 5 %, respectively. Furthermore, at the start of the dropdown the differences between the heat generation in the bearing with surface waviness and the bearing with an ideal surface are low and as the rotor starts to rub against the touchdown bearing, the difference becomes higher. After 0.2 s the difference in the heat generation of the bearing with surface waviness and the ideal case reaches a maximum value.

Due to the smaller radius of the inner race rather than the outer race radius, the friction torque in the inner race (term  $M_{ij}$  in equation (2.22)) is less than the friction torque in the outer race. Therefore, the inner race experiences less heat generation compared to the outer ring. In the first few milliseconds of

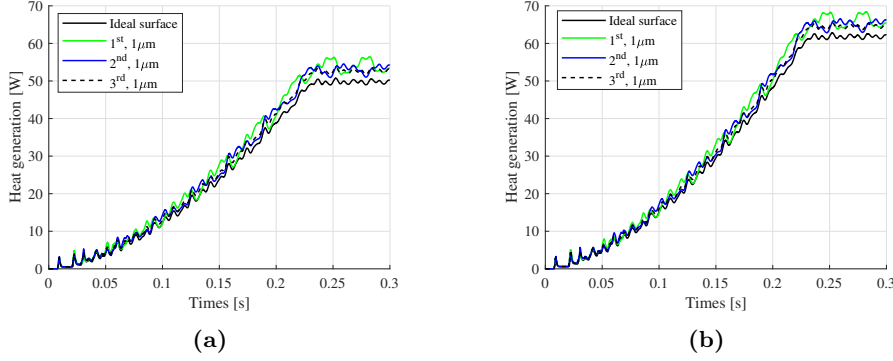


**Figure 4.11.** Internal heat generation in a touchdown bearing a) inner ring b) outer ring.

the simulation, the main part of the global friction torque is due to the load-dependent friction torque. When the inner ring accelerates because of the high angular velocity of the inner ring, the friction drag torque increases. In addition, the friction drag torque is expressed in terms of the angular velocity of the inner ring. For this reason, the heat generation in the bearing follows the same trend as the acceleration of the inner ring. After the inner ring rotates at the same speed as the rotor, a clear fluctuation in the magnitude of the heat generated in the bearing is observed. This can be attributed to the nature of the sinusoidal function used for the numerical simulation of the waviness.

Figure 4.12 depicts the frictional heat generation because of the contact between the rotor and the touchdown bearings. A few milliseconds after the dropdown, the heat generation in the bearing with the ideal surface rises to the maximum value of  $2.8 \cdot 10^4 \text{ W}$ . Then, it is reduced and for a couple of milliseconds becomes zero. Then, the second peak in heat generation is observed. After this, the reduction in heat generation is followed by a fluctuation until 0.2 s. Then, the heat generation becomes zero. The overall pattern shows that waviness imperfection results in a greater amount of heat generation between the rotor and the inner ring rather than the bearing with the ideal surface.

Due to the high magnitude of the contact force between the rotor and inner race, and also the high magnitude of the relative angular velocity of the rotor and inner race, the heat generation in the first contact of the rotor and inner race were found to be considerably greater than the internal heat generated in the bearing. As the inner ring accelerated with the same speed as the rotor (after 0.2 s), the relative velocity between the rotor and the inner ring becomes zero. Therefore, heat generation is equal to zero. Surface waviness in the bearing results in greater penetration of the rotor into the inner ring. Consequently, the contact

force increases and the bearing has to endure higher heat generation. Even though the magnitudes of the peak values are very high, the periods for the highest peaks are just some milliseconds, resulting in a moderate rise in temperatures, as will be shown in the next section.

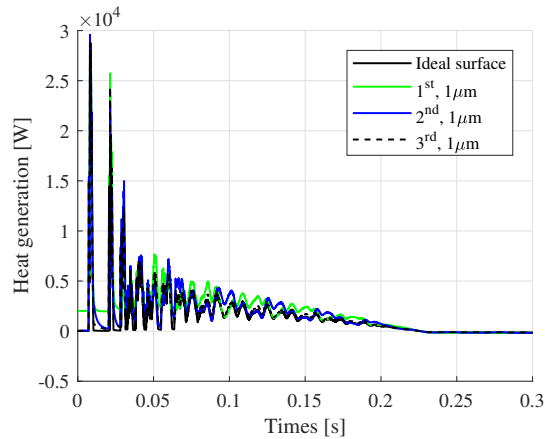


**Figure 4.12.** Friction heat generation in the contact of rotor and touchdown bearings.

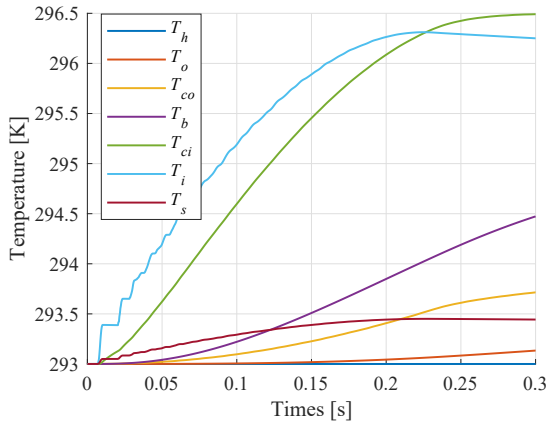
### 4.2.3 Thermal analysis

Figure 4.13 shows the temperature rise for different nodes of the model introduced in Fig. 2.5. This figure shows that the temperature rise in the bearing is not a linear phenomenon. The rotor drop speed, geometry and material property of the rotor and bearing, air gap clearance, as well as friction in the bearing, can influence the temperature of the rotor and touchdown bearing.

At the beginning of the dropdown, the rotor moves downwards; at this time the rotor is not in contact with the touchdown bearing. For this reason, during the first few milliseconds, the temperature of the inner ring is the same as the ambient temperature. After the initial contact, there is a considerable amount of friction heat generation between the rotor and inner ring which can explain the instantaneous increase in the temperature of the inner race. After the first contact of the rotor and inner ring, the rotor bounces back; at this time the temperature remains constant until the rotor contacts the bearing for a second time. This behavior lasts until the rotor continually whirls in the bearings. The temperature of the inner ring increases in relation to the acceleration of the bearing race. When the inner ring accelerates, the temperature of the inner ring increases and when it rotates with the same angular velocity as the rotor (from 0.2 s to end of simulation), the heat generation remains constant and the temperature of the inner ring stabilizes. The high friction between the bearing and rotor, and also

the friction inside the bearing, make the temperature in the contact region of the ball and bearing race and ball relatively high.

In the thermal model of the bearing (Fig. 2.5), the lumped mass of the shaft is significantly greater than the lumped mass of bearing components. Therefore, the temperature of the rotor increases at a lower rate rather than the bearing. Inside the bearing housing, the heat transfers via conduction. Between the outer face of the housing and the environment the heat transfers by natural convection. Therefore, the temperature rise is lower than in other parts and there is not a significant difference in the temperature rise. The results can be partially validated based on the existing literature on rotor dropdowns. The trend in the temperature increase of the inner race is found to be similar to the study of Jin et al. [32] and Zhao et al. [59].



**Figure 4.13.** Temperature rise in the rotor ( $T_s$ ), inner ring ( $T_i$ ), outer ring ( $T_o$ ), ball ( $T_b$ ), housing ( $T_h$ ), contact of the ball and bearing races ( $T_{ci}, T_{co}$ ).

Fig. 4.14(a) shows that in the case where the bearing has some surface waviness regardless of either the amplitude of the waviness or the waviness order, the temperature of the inner ring is higher than the temperature of the bearing with an ideal surface. For the surface waviness at an amplitude of 1  $\mu\text{m}$ , the first order waviness results in a higher temperature rise rather than a higher order of waviness. To observe the influence of the higher amplitude of surface waviness in the temperature rise of the bearing, the last two cases, 2  $\mu\text{m}$  (3rd) and 4  $\mu\text{m}$  (2nd), were studied. The highest studied amplitude for the surface waviness is 4  $\mu\text{m}$ , which is within the range of the surface waviness of bearings with the best bearing manufacturing conditions reported in Ref. [40]. A higher amplitude of surface waviness (2  $\mu\text{m}$ , 3rd) leads to more of a temperature rise in the inner ring. For a bearing with an ideal surface, the temperature rise is 3.5 K, whereas for the last case (4  $\mu\text{m}$ , 2nd) the temperature of the inner race has an 8 K increase.

A similar pattern has been found for the temperature rise of the contact area of the ball and the inner ring (Fig. 4.14(b)). The previous section shows that in the case of surface waviness at an amplitude of 1  $\mu\text{m}$ , the waviness orders 1–3 caused a minor change in friction heat generation. Consequently, the temperature of the inner ring experiences a small increase (approximately 1 K) when compared to the bearing with the ideal surface. With a higher amplitude of the waviness, there are noticeable increases in the contact force and power loss in the bearing. For this reason, the temperature of the inner ring rises noticeably higher than the bearing with an ideal surface.

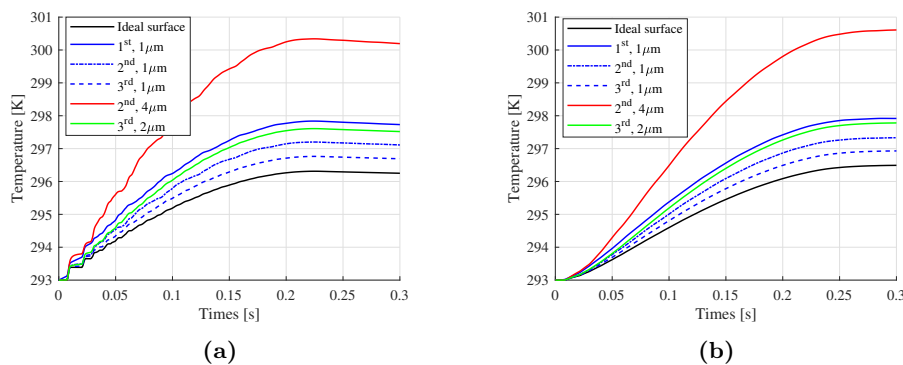


**Figure 4.14.** Temperature rise of a) inner ring b) contact area of ball/inner ring.

### 4.3 Force estimation of a touchdown bearing

*Publications III* and *IV* present a case study of the dropdown of a gas turbine rotor. The touchdown bearings were a pair of angular contact ball bearings of the type XCB71914-E-2RSD-T-P4S-U installed in an X-configuration. The dropdown was studied numerically and experimentally. The first set of experiments and a comparison of the measurement data with the simulation results presented in *Publication III* showed that at the beginning of the test the rotor might not be located in the center and the initial condition of the rotor at the start of the test needs to be considered. In addition, a discrepancy between the nominal air gap and the measurements was found. In the simulation model, the radial movement of the rotor was studied, and the axial movement of the rotor was constrained. However, the dropdown test revealed some axial back and forth movement of the rotor in the dropdown. Further improvements in the model were carried out and in *Publication VI* the touchdown bearing forces were evaluated based on the measured displacement of the rotor.

### Test setup

In the second set of experiments, dropdown tests were carried out at rotation speeds of 60 Hz, 100 Hz, 150 Hz, and 210 Hz for the low-pressure turbine. For safety considerations, the dropdown tests were conducted at a lower speed than nominal speed (550 Hz). At the beginning of the tests, the active magnetic bearings supported the rotor. Then, the radial magnetic bearings were turned off. In the test prototype, two non-contact displacement sensors near each touchdown bearing were used to measure the displacement of the rotor. The system also had a non-contact displacement sensor for measuring the axial displacement of the rotor. In the second sets of dropdown tests, an axial AMB was kept in service to study the radial movement without disturbance from the axial displacement of the rotor. The angular velocity of the rotor was recorded.

The nominal air gap (250  $\mu\text{m}$ ) was found to be different from the measurement results. One of the primary reasons for this discrepancy between the nominal air gap and the measurement value can be due to manufacturing and assembly tolerances, deflections in the system due to previous dropdowns, the differences in the locations of the sensors and bearings, as well as uncertainties of the measurement results. To specify the air gap from the measurement data, at the end of each test where the rotor settles in the touchdown bearing was selected for the air gap limit (from Fig. 4.21). The outcome was; 270  $\mu\text{m}$  and 275  $\mu\text{m}$  for the lower and upper limits of the air gap at NDE (non-drive end). 280  $\mu\text{m}$  and 285  $\mu\text{m}$  for the lower and upper limits of the air gap at DE (drive end).

#### 4.3.1 Support stiffness and damping

The support properties were estimated by studying the vertical displacement of the rotor. The first contact of the rotor and the touchdown bearing was chosen to estimate the support properties. In the first contact, the supports were compressed mostly under the rotor weight, and the side effects from other phenomena that might appear in the dropdown were reduced.

As an example, a zoom in of the vertical displacement of the rotor for the dropdown at 100 Hz is shown in Fig. 4.15. The time  $t_1$  indicates the instance when the rotor starts to make contact with the touchdown bearing, and the rotor displacement is larger than the air gap. In the time duration of  $t_1-t_2$ , the rotor is in contact with the bearing. After this, the rotor bounces. The static equilibrium was selected from the measured displacement of the rotor at the end of the dropdown test where the rotor completely stops and the angular velocity of the rotor reaches zero. The static balance with respect to the mass center of the rotor gives the equivalent mass at each support. Then, the equivalent stiffness of the system is calculated (Eq. (3.3)).

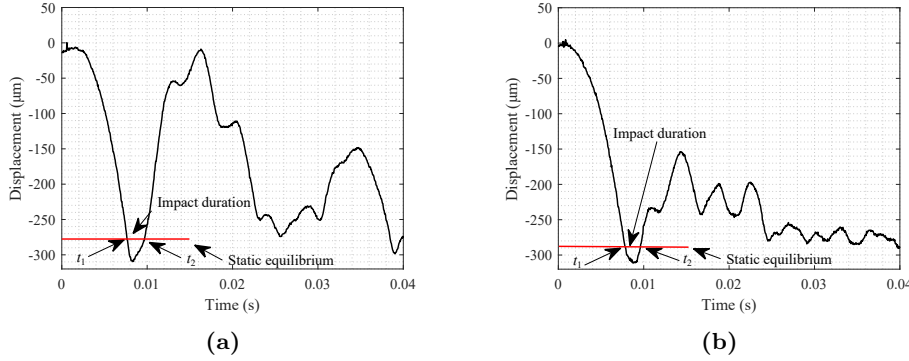


**Figure 4.15.** Determining the equivalent stiffness of the support from the time history of the dropdown test at 100 Hz, a) NDE b) DE.

The equivalent stiffness is a combination of the support and bearing stiffness. However, the mechanical model of the touchdown bearing shown in Fig. 2.2 needs to distinguish the support and bearing properties. In this study, the equivalent stiffness calculated from the measurement data was used to make an initial guess concerning the support properties. Using the touchdown bearing model presented in section 2.2 allows consideration of the deformation and the load of the bearing at different speeds. The least-squares optimization method was used to tune the support properties and minimize the difference between the vertical displacement of the rotor calculated from the simulation and the measurements (limited to the first contact). The final values for the support parameters are given in Table 4.3.

**Table 4.3.** Estimated support properties.

Parameter	NDE	DE
Support mass [kg]	51.2	51.2
Support stiffness [N/m]	$1.31 \cdot 10^8$	$4.03 \cdot 10^8$
Support damping [Ns/m]	$3.27 \cdot 10^3$	$5.74 \cdot 10^3$

Figure 4.16 shows the vertical displacement of the rotor using the same support properties for the dropdowns at 60 Hz, 100 Hz, 150 Hz, and 210 Hz. The simulation results are compared with the corresponding measurements. In this figure, the solid line shows the simulation results and the measurement data are shown by the dashed line. The simulation gives reasonable results for the dropdown at different dropdown speeds, especially for the contact time and the indentation of the rotor in the bearing. The results indicate a small difference between the bounce height of the rotor in the simulation and measurements for a dropdown at 60 Hz. For dropdowns at higher speeds, the difference in the bounce height between the simulation results and the measurement data is higher, mainly due

to the unbalance force. A possible difference between the unbalance phase and magnitude in the simulation and measurement can be a reason for this behavior.

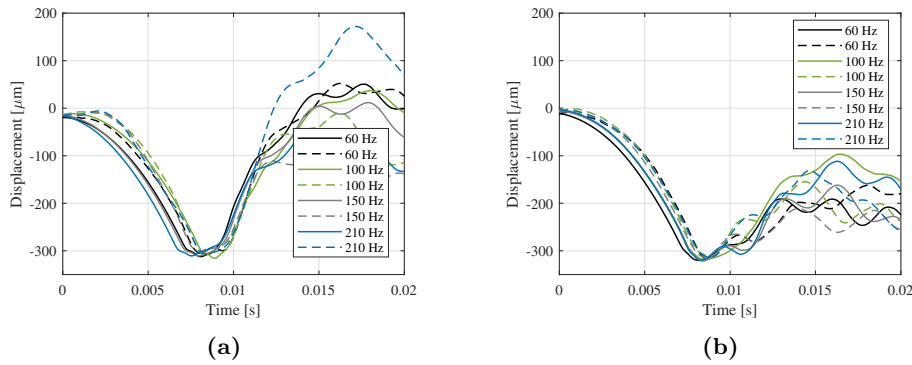


**Figure 4.16.** Vertical displacement of the rotor in the first contact, a) NDE b) DE.

### 4.3.2 Rotor orbit

The comparison of the rotor orbits with the measurement data shows that using the static friction coefficient of 0.13 and the dynamic friction coefficient of 0.1, the highest indentation of the rotor in the inner ring and the path where the rotor bounces agree with the test data. Then, with these parameters the model was assessed for rotor dropdowns at 100 Hz, 150 Hz, and 210 Hz. Examples of rotor orbits for the dropdown at 100 Hz are shown in Fig. 4.17.

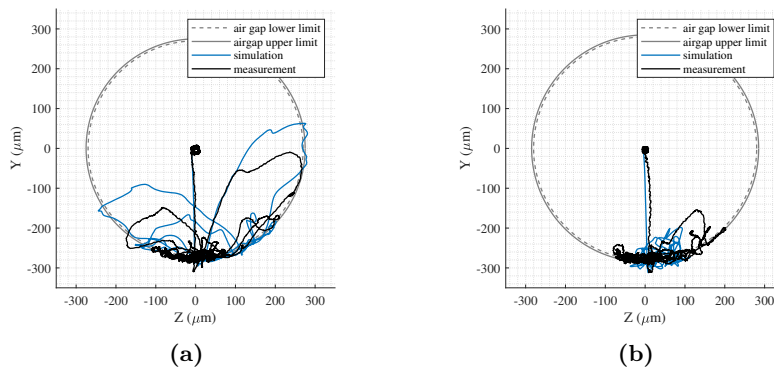


**Figure 4.17.** Rotor orbits under dropdown at 100 Hz a) NDE b) DE.

The horizontal and vertical displacements of the rotor in the DE touchdown bearing are in a better agreement with the test data compared to the NDE touchdown bearing. After the first few contacts of the rotor and NDE touchdown

bearing, a phase difference between the horizontal displacement of the rotor in the simulation and the measurements is observed. The difference between the friction model applied in the model and the actual friction that occurred during the experiment (Fig. 4.18) can be a reason for this phase shift. Similar behavior was found for the dropdowns at 60 Hz, 150 Hz, and 210 Hz.

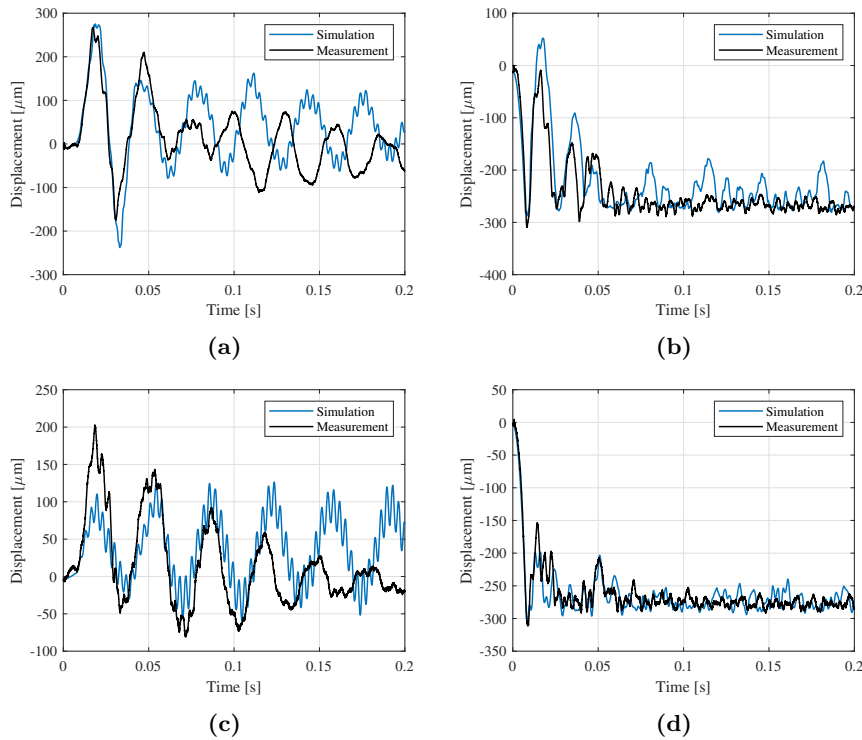


**Figure 4.18.** Rotor displacements under dropdown at 100 Hz a) horizontal at NDE b) vertical at NDE c) horizontal at DE d) vertical at DE.

### 4.3.3 Bearing force

A primary evaluation of the time history of the touchdown bearing force for the dropdown at 60 Hz showed that the maximum bearing force occurs in the initial contacts of the rotor and touchdown bearing (Fig. 4.19). In this case, using the upper limit of the air gap, the highest forces for the NDE and DE touchdown bearings were 2907 N and 4889 N, respectively.

For dropdowns at lower speeds, under gravity the rotor gradually stabilizes around the static level (Using the equivalent mass system shown in section 3.3, the static load at the location of touchdown bearings can be obtained). However, for a

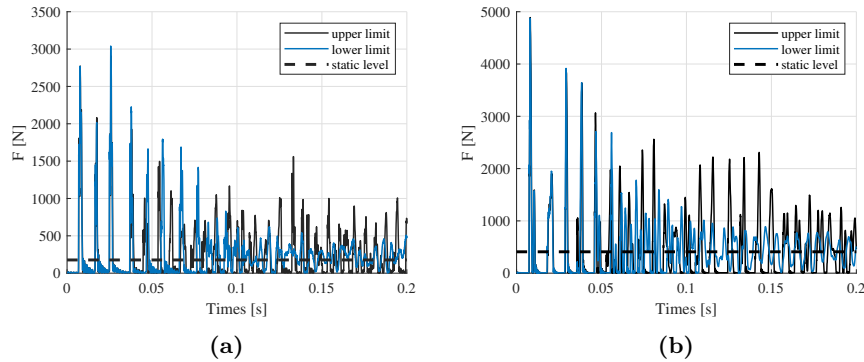


**Figure 4.19.** Bearing forces for dropdowns at a) 60 Hz at NDE b) 60 Hz at DE.

dropdown test at higher speeds the bearing forces were more erratic. In the dropdown at a higher speed, the effect of unbalance force increases and can lead to chaotic motions. The results also indicate that with the upper limit for the air gap the bearing force will be increased. In general, the DE touchdown bearing experiences higher forces than NDE touchdown bearing. Subject to the dropdown test case, the maximum of the bearing force can be seen at various instants.

In the future, the magnitude of the bearing force could be validated by installing a setup for measuring the force. In this study, the maximum Hertzian stresses at different dropdowns were chosen as a basis for relative comparison of different dropdowns. Figure 4.20 shows the relative comparison of the stresses in the touchdown bearing during different dropdowns. In the box plot, the outliers show the points where the stresses are more than three times the standard deviations from the mean of the stress. The high number of outliers implies high variation in the stress with respect to the mean. Table 4.4 shows maximum and average of the stresses in four dropdowns, and the main points of the the statistical analysis are as follows: i): The boxes are skewed and the stresses in the dropdown are non-uniform. ii): The maximum Hertzian stress at the DE touchdown bearing is higher than the NDE touchdown bearing that could be due to an unsymmetrical rotor and the non-central location of the mass center. iii): The average of the stress in the DE touchdown bearing is higher than NDE touchdown bearing.

Table 4.4 also shows that the maximum stress at touchdown bearings is not observed at 210 Hz while it is expected that the maximum stress occurs at dropdown at a higher speed. It should be noted that the maximum stress in the dropdown is not dependent only on the angular velocity of the rotor at the start of the dropdown. The initial condition of the rotor at the start of the tests also affects the estimated force, and therefore affects the stress value. Here, only four dropdown tests were carried out, for quantitative study more number of dropdown

tests should be studied.

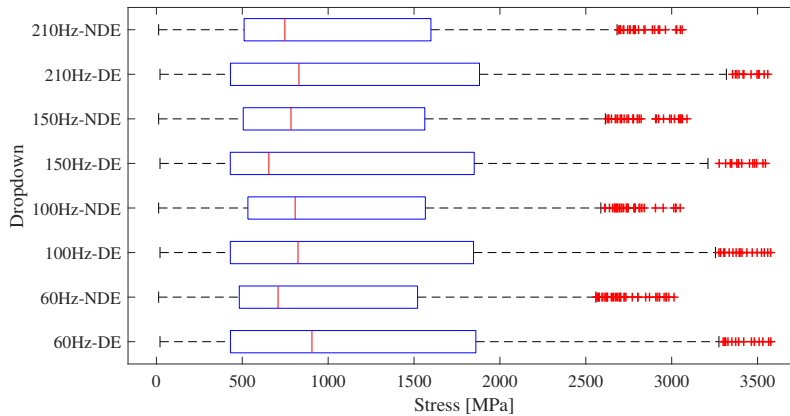


**Figure 4.20.** Box plot for the stress in the bearing, red line: median, +: outliers

**Table 4.4.** Stress in the bearing within 0.2 s (MPa)

Parameter	Maximum stress	Average
DE (60 Hz)	3577	1005
NDE (60 Hz)	3014	970
DE (100 Hz)	3576	1142
NDE (100 Hz)	3049	1038
DE (150 Hz)	3546	1103
NDE (150 Hz)	3089	1024
DE (210 Hz)	3559	1159
NDE (210 Hz)	3061	1025

#### 4.3.4 Further analysis of experimental results

Figure 4.21 shows the magnitudes of the measured displacements of the rotor for a dropdown test at 100 Hz. After 70 s the rotor fully stops on the touchdown bearing. The most important phenomena generally occur at the beginning of dropdown and performing the simulation for the whole dropdown event might not be necessary.

In all dropdown cases, the maximum indentation of the rotor in the touchdown bearings appeared at the initial stage of the dropdown. Therefore, the simulation time of 0.2 s is enough to identify the maximum force on the bearings. The results also show that during the deceleration of the rotor, the system undergoes

resonance. This behavior was observed for dropdowns in other cases. The main cause of this excitation needs to be studied in the future.

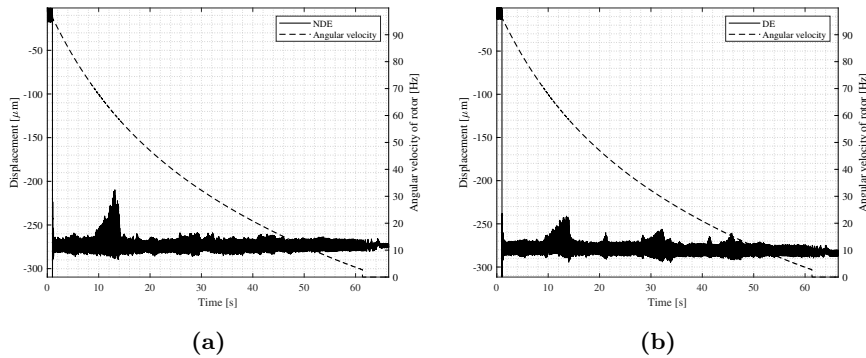


**Figure 4.21.** Magnitude of rotor displacement, dropdown test at 100 Hz a) NDE b) DE.

#### 4.3.5 Waterfall of the rotor dropdown

The FFT was applied to analyze the measurement data. The waterfall plots for the horizontal and vertical displacement of the rotor have the following features: The harmonics of the rotation speed (1X, 2X and 3X) were seen in all dropdown tests. The frequencies at 1.5X, 2.5X, 3.5X and 4.5X observed in the dropdowns at 100 Hz, and 150 Hz, might explain the rub and impact of the rotor in the touchdown bearing (Fig. 4.22).

Resonances at constant frequencies of 29 Hz, 134 Hz, and 235 Hz were found in all dropdown cases. The frequency of 29 Hz shows the frequency of the rotor due to the pendulum movement (see ref. [25]). The frequencies of 134 Hz and 235 Hz were identified using the critical speed map shown in Fig. 4.23. The vertical lines are plotted at the equivalent stiffness and intersect the first and second bending modes near the frequencies of 134 Hz and 235 Hz, respectively. These frequencies show the first and second bending modes of the rotor when settles in the bearing.

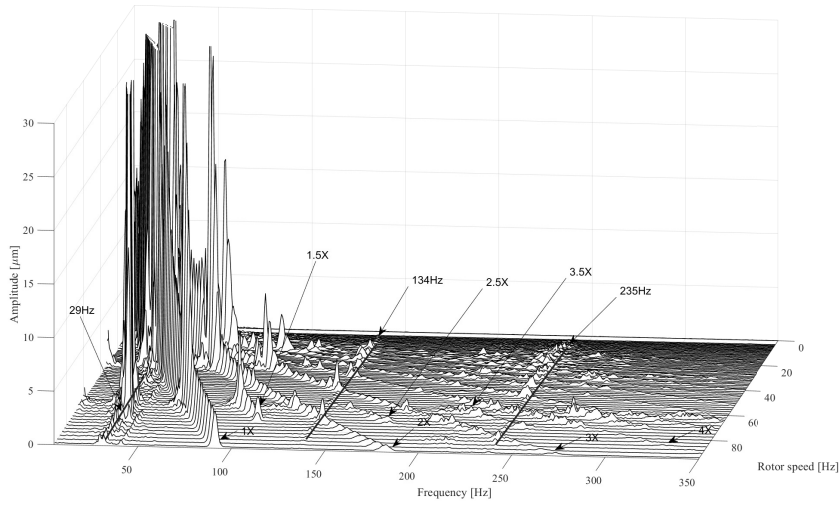


**Figure 4.22.** FFT waterfall for the vertical displacements of rotor at DE, dropdown at 100 Hz.

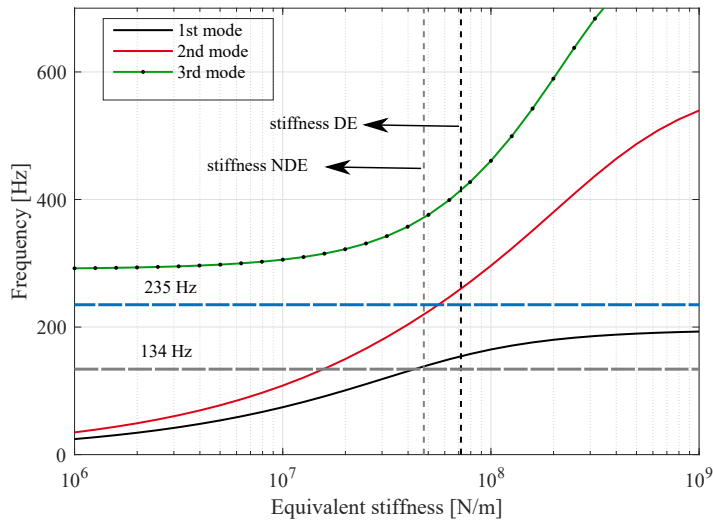


**Figure 4.23.** Critical speed map for the rotor when supported by a touchdown bearing.



## Conclusions

In this dissertation, the dropdown of an AMB supported rotor is presented. The study was initiated by assessment of the stresses in the touchdown bearing of an AMB-supported rotor. The stress in an off-sized ball was also evaluated. Then, the work was extended to develop a dynamic and thermal model of a touchdown bearing and the effect of the surface waviness on heat generation, and the thermal expansion of the touchdown bearing was studied.

In this dissertation, the dropdown of a generator rotor was examined both experimentally and numerically. In the test setup, the dropdown of the rotor for four dropdown speeds was carried out. The model-based approach was used to estimate the touchdown bearing force and different dropdown cases were compared relatively. The main conclusions of the aforementioned aspect are as follows:

### 5.1 Stress in a touchdown bearing with off sized ball

The stresses in the touchdown bearing of an AMB-supported were studied. The touchdown bearings of a deep groove ball bearing type were modeled using a simplified ball bearing model. The Hertzian contact model was used to obtain the stresses in the touchdown bearing. The results showed the distribution of the contact forces and stresses in the dropdown, and revealed that the maximum Hertzian stresses were not uniformly distributed among all the balls. In the first contact of the rotor and touchdown bearing, the balls which were initially located in the loaded zone of the bearing experienced higher stress, and as the inner ring started to accelerate, the location and the magnitude of the stress in the bearing changed. In addition, the model also enabled an evaluation of the effect of the off-sized ball on the stresses in the touchdown bearing. The results showed that

with off-sized balls within acceptable tolerance limits defined in standard ISO 3290-1, the change in Hertzian stress was not significant, although observable.

## 5.2 Influence of surface waviness in the heat generation and thermal expansion of a touchdown bearing

A dynamic and thermal model of a touchdown bearing was developed. The friction heat is generated due to the impact of the rotor on the touchdown bearing, and the internal friction torque in the bearing. A one-dimensional equivalent electrical circuit model was applied for the thermal model. The results showed that the temperature rise in the bearing is influenced by the variation of the angular velocity of the rotor and the inner ring, and the friction between the rotor and touchdown bearing, as well as the friction inside the bearing. Moreover, differences in the surface waviness in the bearing were studied. It was found that for a small amplitude of surface waviness, the various orders of surface waviness result in small changes in the contact force and heat generation in the bearing. The results indicated that the amplitude of the waviness has a greater effect on increasing the power loss and contact forces between balls, and also the contact of the rotor and inner race. Meanwhile, for the constant amplitude of the waviness, the higher waviness order does not lead to a considerable change in the results.

## 5.3 Model-based performance evaluation of a touchdown bearing

The model-based approach was used to estimate the touchdown bearing force. The dropdown test data was integrated with a simulation model. The modal expansion method was applied to calculate the initial condition of the rotor from the measurements. The support properties were approximated by using an equivalent single-mass model and was assessed to be robust for four dropdown cases. The rotor's displacement in the simulation was seen to agree with the test data, reasonably. The vertical displacement of the rotor was found to agree with the test results. In the horizontal displacement of the rotor, phase shifts in the responses were seen which can be due to the potential difference between the friction model and the test, and also the unbalance force.

The initial condition of the rotor has an important effects on the behaviour of the rotor in the dropdown. The dropdown test at a higher speed reveals a more erratic movement of the rotor, mainly due to the unbalance force. In the future, the magnitude of the bearing force should be validated by force measurement. In this study the rotor is unsymmetrical and the location of the mass center was closer to the DE touchdown bearing. Therefore, the maximum stress in the DE touchdown bearing is higher than the NDE touchdown bearing.

The FFT analysis of the recorded displacement of the rotor showed the harmonics of the rotational frequencies. When the dropdown was performed at a higher speed, the rub-impact frequencies were also observed. The constant frequencies representing the pendulum movement of the rotor as well as the first and second bending modes of the rotor settled in the bearing were seen in the FFT.

#### SUGGESTIONS FOR FUTURE WORK

The work presented in this dissertation can be continued by installing a force measurement system, which could be used for validating the magnitude of the bearing force. In addition, installing a measurement setup for the temperature of the touchdown bearing and evaluating the surface condition of the inner ring of the touchdown bearing is recommended.

As mentioned in the dissertation, there are some uncertainties due to the measurement error, and this could be clarified by rechecking the parameters according to the manufacturing data, measuring the from actual condition of machine (if it is possible), and controlling the sensor condition.

The numerical model can be improved by considering the advanced method for nonlinear estimation and applying machine learning techniques.



---

## REFERENCES

---

- [1] AI, S., WANG, W., WANG, Y., AND ZHAO, Z. Temperature rise of double-row tapered roller bearings analyzed with the thermal network method. *Tribology International* 87 (2015), 11–22.
- [2] AKTÜRK, N., AND GOHAR, R. The effect of ball size variation on vibrations associated with ball-bearings. *Proceedings of the Institution of Mechanical Engineers, Part J: Journal of Engineering Tribology* 212, 2 (1998), 101–110.
- [3] API617. Axial and centrifugal compressors and expander-compressors for petroleum, chemical and gas industry services 8th ed. (2014).
- [4] BARTHA, A. R. *Dry friction backward whirl of rotors*. PhD thesis, ETH Zurich, 2000.
- [5] BEAMS, J. W., AND HOLMES, F. T. Suspension of rotatable bodies, Sept. 23 1941. US Patent 2,256,937.
- [6] BREWE, D. E., AND HAMROCK, B. J. Simplified solution for elliptical-contact deformation between two elastic solids. *Journal of Lubrication Technology* 99, 4 (1977), 485–487.
- [7] BURTON, R., AND STAPH, H. Thermally activated seizure of angular contact bearings. *ASLE Transactions* 10, 4 (1967), 408–417.
- [8] CHANGQING, B., AND QINGYU, X. Dynamic model of ball bearings with internal clearance and waviness. *Journal of Sound and Vibration* 294, 1-2 (2006), 23–48.
- [9] ESCHMANN, P., AND HASBARGEN, L. *Ball and Roller Bearings: Theory, Design and Application*, 2 ed. John Wiley and Sons, New York, 1985.
- [10] FONSECA, C. A., SANTOS, I. F., AND WEBER, H. I. Influence of unbalance levels on nonlinear dynamics of a rotor-backup rolling bearing system. *Journal of Sound and Vibration* 394 (2017), 482–496.

- 
- [11] FUMAGALLI, M. Impact dynamics of high speed rotors in retainer bearings and measurement concepts. In *Proceedings of the Fourth International Symposium on Magnetic Bearings, ETH Zurich* (1992), pp. 239–244.
- [12] GREENWOOD, J. Analysis of elliptical Hertzian contacts. *Tribology International* 30, 3 (1997), 235–237.
- [13] GUPTA, P. K. Frictional instabilities in ball bearings. *Tribology Transactions* 31, 2 (1988), 258–268.
- [14] HABERMANN, H. Magnetic bearing block device for supporting a vertical shaft adapted for rotating at high speed, May 8 1973. US Patent 3,731,984.
- [15] HABERMANN, H., AND BRUNET, M. Magnetic bearings, Mar. 15 1977. US Patent 4,012,083.
- [16] HABERMANN, H., BRUNET, M., AND LECLERE, J. Radial displacement detector device for a magnetic bearing, Sept. 19 1978. US Patent 4,114,960.
- [17] HABERMANN, H., JOLY, P., AUBER, Y., LOYEN, R., AND LOYEN, N. V. G. Devices including rotating members supported by magnetic bearings, Jan. 22 1974. US Patent 3,787,100.
- [18] HALMINEN, O., ACEITUNO, J. F., ESCALONA, J. L., SOPANEN, J., AND MIKKOLA, A. A touchdown bearing with surface waviness: A dynamic model using a multibody approach. *Proceedings of the Institution of Mechanical Engineers, Part K: Journal of Multi-body Dynamics* 231, 4 (2017), pp. 658–669.
- [19] HALMINEN, O., ACEITUNO, J. F., ESCALONA, J. L., SOPANEN, J., AND MIKKOLA, A. A touchdown bearing with surface waviness: Friction loss analysis. *Mechanism and Machine Theory* 110 (2017), 73–84.
- [20] HAMROCK, B. J., AND DOWSON, D. Ball bearing mechanics. *NASA Technical Memorandum 81691* (1981).
- [21] HARRIS, T. A. *Rolling Bearing Analysis*, 4 ed. John Wiley & sons, New York, 2001.
- [22] HARRIS, T. A., AND KOTZALAS, M. N. *Essential concepts of bearing technology*, 5 ed. CRC press, 2006.
- [23] HARSHA, S. Nonlinear dynamic analysis of rolling element bearings due to cage run-out and number of balls. *Journal of Sound and Vibration* 289, 1-2 (2006), 360–381.

- [24] HARSHA, S., AND KANKAR, P. Stability analysis of a rotor bearing system due to surface waviness and number of balls. *International Journal of Mechanical Sciences* 46, 7 (2004), 1057–1081.
- [25] HAWKINS, L., FILATOV, A., IMANI, S., AND PROSSER, D. Test results and analytical predictions for rotor drop testing of an active magnetic bearing expander/generator. *Journal of Engineering for Gas Turbines and Power* 129 (2007), 522–529.
- [26] HEIKKINEN, J. E., GHALAMCHI, B., VIITALA, R., SOPANEN, J., JUHANKO, J., MIKKOLA, A., AND KUOSMANEN, P. Vibration analysis of paper machine’s asymmetric tube roll supported by spherical roller bearings. *Mechanical Systems and Signal Processing* 104 (2018), 688–704.
- [27] HELFERT, M., ERNST, M., NORDMANN, R., AND AESCHLIMANN, B. High-speed video analysis of rotor-retainer-bearing-contacts due to failure of active magnetic bearings. In *Proceedings of the 10th International Symposium on Magnetic Bearings* (2006), Martigny Switzerland, pp. 560–565.
- [28] HUNT, K. H., AND CROSSLEY, F. R. E. Coefficient of restitution interpreted as damping in vibroimpact. *Journal of Applied Mechanics* 42, 2 (1975), 440–445.
- [29] ISO14839-4. Mechanical vibration-vibrations of rotating machinery equipped with active magnetic bearings-part, 1st ed. (2012).
- [30] JARROUX, C., DUFOUR, R., MAHFOUD, J., DEFOY, B., ALBAN, T., AND DELGADO, A. Touchdown bearing models for rotor-AMB systems. *Journal of Sound and Vibration* 440 (2019), 51–69.
- [31] JIN, C., WU, B., AND HU, Y. Heat generation modeling of ball bearing based on internal load distribution. *Tribology International* 45, 1 (2012), 8–15.
- [32] JIN, C., ZHU, Y., XU, L., XU, Y., AND ZHENG, Y. The thermodynamic properties of a new type catcher bearing used in active magnetic bearings system. *Applied Thermal Engineering* 82 (2015), 253–263.
- [33] KÄRKKÄINEN, A., SOPANEN, J., AND MIKKOLA, A. Dynamic simulation of a flexible rotor during drop on retainer bearings. *Journal of Sound and Vibration* 306, 3-5 (2007), 601–617.
- [34] KRÄMER, E. *Dynamics of rotors and foundations*, 1 ed. Springer-Verlag, Berlin, 1993.

- [35] KUDU, F. N., UÇAK, Ş., OSMANCIKLI, G., TÜRKER, T., AND BAYRAKTAR, A. Estimation of damping ratios of steel structures by operational modal analysis method. *Journal of Constructional Steel Research* 112 (2015), 61–68.
- [36] LEE, J. G., AND PALAZZOLO, A. Catcher bearing life prediction using a rainflow counting approach. *Journal of Tribology* 134, 3 (2012), 031101.
- [37] LIU, W., ZHANG, Y., FENG, Z.-J., ZHAO, J.-S., AND WANG, D. A study on waviness induced vibration of ball bearings based on signal coherence theory. *Journal of Sound and Vibration* 333, 23 (2014), 6107–6120.
- [38] MARKERT, R., PLATZ, R., AND SEIDLER, M. Model based fault identification in rotor systems by least squares fitting. *International Journal of Rotating Machinery* 7, 5 (2001), 311–321.
- [39] MEEKS, C. R. Magnetic bearing structure, May 5 1992. US Patent 5,111,102.
- [40] MOHANTY, A. R. *Machinery condition monitoring: Principles and Practices*. CRC Press, 2018.
- [41] NELSON, H. A finite rotating shaft element using Timoshenko beam theory. *Journal of Mechanical Design* 102, 4 (1980), 793–803.
- [42] NGUYEN-SCHÄFER, H. *Computational design of rolling bearings*. Springer, 2016.
- [43] OLSSON, H., ÅSTRÖM, K. J., DE WIT, C. C., GÄFVERT, M., AND LISCHINSKY, P. Friction models and friction compensation. *Eur. J. Control* 4, 3 (1998), 176–195.
- [44] PALMGREN, A. Ball and roller bearing engineering. *Philadelphia: SKF Industries Inc., 1959* (1959).
- [45] PORITSKY, H., HEWLETT, C., AND COLEMAN, R. Sliding friction of ball bearings of the pivot type. *Journal of Applied Mechanics, Transactions of the ASME* 14, 4 (1947), A261–A268.
- [46] RAJU, K., RAMESH, K., SWANSON, E., AND KIRK, R. Simulation of amb turbomachinery for transient loading conditions. Tech. rep., Technomic Publishing Co. Inc., Lancaster, PA (United States), 1995.
- [47] SCHMIED, J., AND PRADETTO, J. Behavior of a one ton rotor being dropped into auxiliary bearings. In *Third International Symposium on Magnetic Bearings, Alexandria, VA* (1992), pp. 29–31.

- [48] SIEGL, G., TZIANETOPOULOU, T., AND DENK, J. Simulation and experimental validation of a 9 ton AMB rotor landing in rolling element back-up bearings. *Mechanical Engineering Journal* 3, 1 (2016), 15–00136.
- [49] SOPANEN, J. *Studies of rotor dynamics using a multibody simulation approach*. PhD thesis, Lappeenranta University of Technology, 2004.
- [50] SOPANEN, J., AND MIKKOLA, A. Dynamic model of a deep-groove ball bearing including localized and distributed defects. part 1: Theory. *Proceedings of the Institution of Mechanical Engineers, Part K: Journal of Multi-body Dynamics* 217, 3 (2003), 201–211.
- [51] SUN, G. Auxiliary bearing life prediction using hertzian contact bearing model. *Journal of Vibration and Acoustics, Transactions of the ASME* 128, 2 (2006), 203–209.
- [52] SUN, G. Rotor drop and following thermal growth simulations using detailed auxiliary bearing and damper models. *Journal of Sound and Vibration* 289, 1-2 (2006), 334–359.
- [53] TAKABI, J., AND KHONSARI, M. Experimental testing and thermal analysis of ball bearings. *Tribology International* 60 (2013), 93–103.
- [54] TAKABI, J., AND KHONSARI, M. On the thermally-induced failure of rolling element bearings. *Tribology International* 94 (2016), 661–674.
- [55] VAN RENSBURG, J. J., VAN SCHOOR, G., VAN VUUREN, P., AND VAN RENSBURG, A. J. Experimental validation of a rotor delevitation model with quantified severity indicators. *Measurement* 122 (2018), 82–90.
- [56] WARDLE, F. Vibration forces produced by waviness of the rolling surfaces of thrust loaded ball bearings part 1: Theory. *Proceedings of the Institution of Mechanical Engineers, Part C: Journal of Mechanical Engineering Science* 202, 5 (1988), 305–312.
- [57] WARDLE, F. Vibration forces produced by waviness of the rolling surfaces of thrust loaded ball bearings part 2: Experimental validation. *Proceedings of the Institution of Mechanical Engineers, Part C: Journal of Mechanical Engineering Science* 202, 5 (1988), 313–319.
- [58] YAN, K., WANG, N., ZHAI, Q., ZHU, Y., ZHANG, J., AND NIU, Q. Theoretical and experimental investigation on the thermal characteristics of double-row tapered roller bearings of high speed locomotive. *International Journal of Heat and Mass Transfer* 84 (2015), 1119–1130.

- [59] ZHAO, Y., YANG, G., SHI, Z., AND ZHAO, L. Thermal analysis and simulation of auxiliary bearings and its application in the high temperature reactor-10. *Journal of Tribology* 138, 1 (2016), 011102.
- [60] ZHUO, Y., ZHOU, X., AND YANG, C. Dynamic analysis of double-row self-aligning ball bearings due to applied loads, internal clearance, surface waviness and number of balls. *Journal of Sound and Vibration* 333, 23 (2014), 6170–6189.

## Publication I

Neisi, N., Sikanen, E., Heikkinen, J., Sapanen, J.

**Effect of off-sized balls on contact stresses in a touchdown bearing**

Reprinted with permission from

*Tribology International*

120 (2018) 340–349.

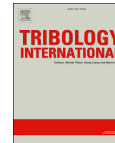
© 2018, Elsevier.





Contents lists available at ScienceDirect

Tribology International

journal homepage: [www.elsevier.com/locate/triboint](http://www.elsevier.com/locate/triboint)

## Effect of off-sized balls on contact stresses in a touchdown bearing

Neda Neisi<sup>\*</sup>, Eerik Sikanen, Janne E. Heikkinen, Jussi Sopenan



Department of Mechanical Engineering, Lappeenranta University of Technology, Skinnarilankatu 34, 53850 Lappeenranta, Finland

### ARTICLE INFO

#### Keywords:

Touchdown bearing  
Dropdown  
Hertzian contact stress  
Off-sized ball

### ABSTRACT

Contact stresses of a ball bearing type touchdown bearing with off-sized balls are studied. The touchdown bearing model includes descriptions of the stiffness, damping and friction between bearing components. The model gives the contact deformations between the balls and bearing races, contact forces, and Hertzian contact stresses in each ball. The bearing model is used in simulation together with a model of a flexible rotor. The results show that off-sized ball or balls alters the contact stiffness between the balls and bearing race and the localized deformation of race. The contact force and stresses consequently change. The stress values are dependent not only on the dimension of the off-sized ball or balls but also their location.

### 1. Introduction

Active magnetic bearings (AMBs) are a modern bearing family in which an electromagnetic field levitates the rotor and there is no physical contact between the rotating and stationary parts. AMB systems are wear-free but require continuous active control. The active control enables adjusting of dynamic motions of the system during usage and offers a valuable system control feature during regular operation that is not available with conventional bearing technology. Although AMBs have many advantages over conventional bearings, they require touchdown bearings in case of overload or failure of the electromagnetic field.

For many years, considerable effort has been devoted to study the contact of the rotor with the touchdown bearing. Comparison between experimental and numerical dropdown tests of a heavy industrial rotor performed by Schmied and Pradetto [1] revealed that as a result of time delay in the shutdown system and the existence of high electromagnetic forces at the beginning of the dropdown test, experimental results can differ from predicted numerical values. Keogh [2] developed a control model for thermal bending of the rotor and the interaction of the AMB system with the touchdown bearing. Kärkkäinen et al. [3] presented a comprehensive study on modeling contact in an AMB supported rotor. The work presented a modal reduction method and studied the effect of the number of modes used in the analysis of the touchdown event. The authors concluded that several mode pairs should be used because the touchdown impact might excite higher frequency eigenmodes. A recent paper by Halminen et al. [4] demonstrated the dynamic behavior of a rotor in a cageless touchdown

bearing with misalignment. It was noticed that in a touchdown bearing without misalignment the rotor settles quite rapidly. Increasing the misalignment affects the whirling motion of the rotor and a high degree of misalignment may cause severe whirling motion of the shaft and increases the probability of failure.

The above-mentioned references consider the touchdown phenomenon in general, and only a limited number of publications can be found that focus specifically on bearing life and stress analysis of touchdown bearings. Lifetime and stress are important issues for engineers designing touchdown bearings, especially since the rolling element in touchdown bearing applications experiences exceptional loading. Sun [5] estimated the fatigue life of the touchdown bearing. He evaluated the Hertzian contact stresses and used Lundberg-Palmgren method to approximate the fatigue life of the bearing. The drawback in the selected method is that the Lundberg-Palmgren method is applicable only for steady state loading conditions while in the touchdown bearings the load is time varying. After a few years, Lee and Palazzolo [6] applied the rainflow analysis to consider the time varying stress in evaluating the fatigue life of touchdown bearing. For the purpose of studying the stress in touchdown bearing, the load distribution and the contact forces in the touchdown bearings should be studied which can be based on the bearing models for conventional rotor-bearing systems. It is important to mention that the touchdown bearings used in AMB system distinct from the conventional rotor-bearing system in the following aspects: 1) In the conventional rotor-bearing system, the frictionless bearings are mounted on the shaft by either press fit or shrink fit. While in the AMB supported rotor, the air gap clearance exists between the inner ring of

<sup>\*</sup> Corresponding author.

E-mail addresses: [neda.neisi@lut.fi](mailto:neda.neisi@lut.fi) (N. Neisi), [eerik.sikanen@lut.fi](mailto:eerik.sikanen@lut.fi) (E. Sikanen), [janne.e.heikkinen@lut.fi](mailto:janne.e.heikkinen@lut.fi) (J.E. Heikkinen), [jussi.sopenan@lut.fi](mailto:jussi.sopenan@lut.fi) (J. Sopenan).

<https://doi.org/10.1016/j.triboint.2017.12.036>

Received 21 July 2017; Received in revised form 5 November 2017; Accepted 24 December 2017

Available online 28 December 2017

0301-679X/© 2018 Elsevier Ltd. All rights reserved.

Nomenclature			
$A$	Principal curvature of contact	$\alpha$	Contact parameter
$a$	Semi-major axis of the elliptic area	$\beta$	Attitude angle
$B$	Principal curvature of contact	$\Gamma$	Misalignment
$b$	Semi-minor axis of the elliptic area	$\delta$	Deformation of contact area
$C$	Damping matrix	$\kappa$	Elliptic eccentricity parameter
$c_r$	Radius of air gap	$\mu$	Friction coefficient
$d$	Diameter of the ball	$\nu$	Poisson's ratio
$d'$	Distance between inner race and outer race	$\bar{\xi}$	Elliptic integral of the first kind
$E$	Modulus of elasticity	$\sigma_{max}$	Maximum contact stress
$E^{eq}$	Effective Modulus of elasticity	$\varphi$	Contact angle
$e$	Eccentricity	$\Omega$	Angular velocity of the rotor
$F$	Force		
$F_1$	Vector of nodal unbalance	<i>Subscript</i>	
$F_2$	Vector of externally applied force	$c$	Contact
$G$	Gyroscopic matrix	$I$	Contact body I
$K$	Stiffness matrix	$II$	Contact body II
$K$	Contact stiffness	$in$	Inner race
$M$	Mass matrix	$j$	$j^{th}$ ball
$Q$	Normal force	$N$	Number of balls
$q$	Vector of generalized coordinate	$out$	Outer race
$R$	Radius	<i>Superscripts</i>	
$R_r$	Conformity ratio	$r$	Radial
$r$	Radius	$t$	Axial
		$tot$	Total

bearing and rotor and the bearing carries the load in case of overload or failure of the magnetic field. II) When the magnetic field operates properly, the inner ring of touchdown bearing is stationary. As the rotor drops due to the contact with the touchdown bearing, the inner ring starts to accelerate rapidly. Therefore in the system of equation of motion, the contact force and the friction between the rotor and the inner ring is taken into account. The load carrying capacity of touchdown bearings is dependent on both the static load and the dynamic load. Several bearing models can be found for the ball bearing, where the influence of centrifugal force and gyroscopic moment on the bearing performance is discussed in the paper presented by Kurvinen et al. [7]. The load distribution and heat generation due to internal friction in the touchdown bearing of high speed rotor can be modeled based on the high speed model for conventional ball bearing presented in the study of Jin et al. [8], where the centrifugal force as well as gyroscopic are taken into account in calculation of load distribution in the bearing. They considered the effects of the rotational speed and operating condition on the heat generation in the ball bearing and validated the model with the experimental setup.

Additionally, the dimensional error might exist in various types of bearings including touchdown bearings. It should be considered that in spite of recent development in the manufacture of high precision ball bearings, the identical balls are hard to produce and there is a possibility that the diameter of the balls might have some deviation from the nominal size. Balls having this defect are known as off-sized balls. Available scientific knowledge on the stresses in touchdown bearings generally assumes that the bearing is in ideal condition and dimensional error are rarely taken into account. The size deviation changes the contact force, which consequently can affect the dynamic performance of the bearing [9]. In the literature, several publications can be found that discuss the static and dynamic analysis of off-sized balls in conventional ball bearings. Gupta [10] studied the effect of off-sized ball dimensions and showed that when the deviation of the off-sized ball increases beyond the tolerance limit, the circular shape of the orbit of the ball changes to a polygonal shape. Vibration analysis of off-sized balls in ball bearings indicates that the vibration response of the off-sized balls can be characterized by cage frequency and its harmonics [11,12]. Nonlinear

dynamic analysis of ball bearing as a result of cage run out and bearing ring waviness was studied by Harsha [12] and Wardle et al. [13]. Harsha [12] also concluded that with the higher number of balls, the system stiffness increases and can reduce the amplitude of vibration. Chen et al. [9] provided a model for static load distribution in a roller bearing with off-sized balls. Similarly, a model for static load distribution of the deep groove ball bearing with the off-sized ball was developed by Zhou et al. [14]. Oswald et al. [15] studied the effect of internal clearance in both a ball bearing and a roller bearing and introduced a mathematical function for bearing life in terms of a dimensionless internal diametric clearance number. It was shown that small negative clearance can enhance the lifetime of the bearing and excessive clearance decreases the lifetime. Zhou et al. [16] applied the Lundberg-Palmgren life theory to illustrate the effect of off-sized balls on the fatigue life of a deep groove ball bearing.

In the AMB supported rotors, there is a considerable contact force and friction due to the collision of the rotor and touchdown bearing besides the whirling motion of the rotor which can lead to the rolling contact failure in the bearing. For the design aspect of the touchdown bearing, it is important to identify the stress imposed to the bearing and ensure that the bearing can tolerate the stress in the dropdown. For this reason, it is essential to conduct studies about the contact stress in the touchdown bearing. There are few papers available about the stress in touchdown bearing assuming the bearing is in ideal condition and the dimensional error as off-sized ball is not taken into account. Although there has been a considerable development in the manufacturing of high precision ball, the off-sized ball can exist in the bearing which can influence the contact stress in the touchdown bearing. The present study applies the Hertzian stress model to feature the stresses in the touchdown bearing, which can provide a computational model for the stress in the touchdown bearings. In the dropdown, the stresses in the bearing are not uniform. In the matter off-sized ball or balls, the load distribution in the bearing can deviate from the contact load in the bearing with ideal dimension and consequently affects the stress in the bearing. Therefore, the effect of one or more off-sized balls on the maximum contact stress of touchdown bearings is an important issue that needs to be addressed. With

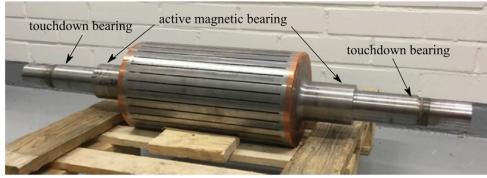


Fig. 1. Rotor under investigation.

this goal, the current study examines the load distribution effects in the touchdown bearing with off-sized balls. Additionally, the paper studies the effect of the location and number of off-sized balls on the contact stress, as well as the effect of the degree of deviation from nominal size.

2. Rotor and touchdown bearing models

Fig. 1 features the case study of the high-speed rotor. The photo was taken after manufacturing of the electric motor part, when the rotor was carried to the laboratory for an experimental modal analysis. In the regular operating condition, the rotor is supported by AMBs. During the dropdown event, it is in contact with the touchdown bearings at both ends of the rotor.

In the present work, Timoshenko beam elements are used in constructing the FE-model of the rotor. The contact forces between the rotor and the touchdown bearing as well as the internal contact force in the touchdown bearing are defined by the Hertzian contact model. A simplified spring-damper and mass model is utilized to model the bearing housings and supports. The equation of motion of the system is given by Ref. [17]:

$$M\ddot{q} + (C + \Omega G)\dot{q} + Kq = \Omega^2 F_1 + F_2 \tag{1}$$

where M, C, G and K are the mass, damping, gyroscopic and stiffness

Table 1

Technical data for the simulation of the rotor dropdown.

Simulation parameter	Value
Mass of rotor	97.3 kg
Initial rotation speed of the rotor	20000 rpm
Modulus of elasticity	2.0·10 <sup>11</sup> Pa
Material density	7801 kg/m <sup>3</sup>
Poisson's ratio	0.3
Support mass	5 kg
Support stiffness	5·10 <sup>7</sup> N/m
Support damping	5000 Ns/m
Contact stiffness between rotor and inner race	1.25·10 <sup>9</sup> N/m <sup>1.11</sup>
Parameter for contact between rotor and inner race	0.08
Air gap	300 μm
Polar moment of inertia of rotor	0.39 kgm <sup>2</sup>
Diameter moment of inertia of rotor	2.82 kgm <sup>2</sup>
Inner diameter of sleeve	60.6 mm
Outer diameter of sleeve	80.0 mm
Unbalance mass (node 9)	6·10 <sup>-5</sup> kg m @ 0°
Static contact friction coefficient between rotor and inner race	0.2
Dynamic contact friction coefficient between rotor and inner race	0.1

matrices of the rotor system, respectively. Vector q contains the system's coordinates while vectors F<sub>1</sub> and F<sub>2</sub> describe nodal unbalances and externally applied forces, respectively. The rotor under investigation rotates at the speed of Ω. Free-free bending frequencies of the rotor are measured by experimental modal analysis.

2.1. Model of a touchdown bearing with an off-sized ball

The current study utilizes a simplified model for a ball bearing presented in Ref. [18]. In this study, the centrifugal forces as well as gyroscopic moment are not included in the simulation, and the effect of the hydrodynamic oil film is neglected. The model consists of both the internal friction torque in the bearing and the mass moment of inertia of the inner race. In the matter of a touchdown bearing having an off-sized ball, the relative distance between each ball and the bearing race should be considered. In order to model the off-sized ball in a bearing, the ball diameter needs to be defined in a vector as follows:

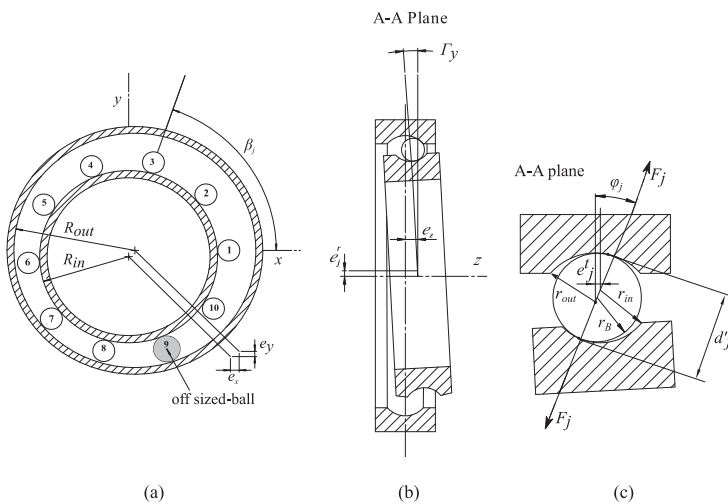


Fig. 2. Cross-section of the ball bearing.

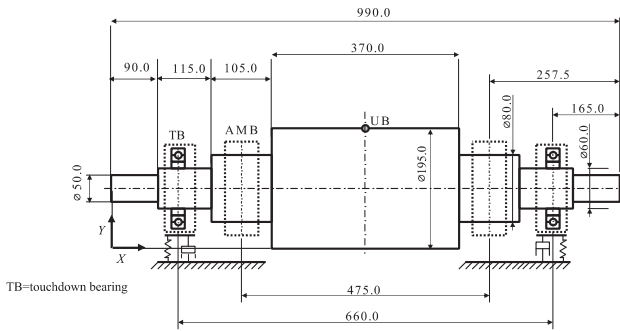


Fig. 3. Main dimensions of the rotor.

$$d = [d_1 \ d_2 \ \dots \ d_j \ d_N] \tag{2}$$

where  $N$  is the number of balls.

The relative displacement between rings for the ball number  $j \in [1, N]$  in the radial ( $e'_j$ ) and axial ( $e''_j$ ) direction is as follows [7]:

$$\begin{aligned} e'_j &= e_x \cos \beta_j + e_y \sin \beta_j \\ e''_j &= e_z - (-\Gamma_x \sin \beta_j + \Gamma_y \cos \beta_j)(R_{in} + r_{in}) \end{aligned} \tag{3}$$

where  $e_x$ ,  $e_y$  and  $e_z$  are the relative displacements of the bearing races in the principal axes (Fig. 2 (a, b)). Angular misalignment of the inner race in the  $x$  and  $y$ -directions are denoted as  $\Gamma_x$  and  $\Gamma_y$ , respectively. Angle  $\beta_j$  represents the ball attitude angle, while  $R_{in}$  and  $r_{in}$  are the inner race radius and inner race groove radius. The race conformity, the ratio between the radius of the bearing race and the diameter of the ball, can be defined as follows [18]:

$$R_v = \frac{r}{d} \tag{4}$$

Therefore, the radius of the inner/outer race groove ( $r_{in}$ ,  $r_{out}$ ) shown in Fig. 2 (c) can be obtained.

In the simulation, the coordinate transformation is used to map the coordinate system of the bearing on the FE-model of the rotor. The distance between the races,  $d'_j$ , can be calculated as follows [7]:

$$d'_j = r_{out} + r_{in} - \frac{R_{in} + r_{in} + e'_j - R_{out} + r_{out}}{\cos \varphi_j} \tag{5}$$

where,  $\varphi_j$  is the contact angle for each ball [7]:

$$\varphi_j = \tan^{-1} \left( \frac{e'_j}{R_{in} + r_{in} + e'_j - R_{out} + r_{out}} \right) \tag{6}$$

Thus, the total deformation  $\delta_j^{tot}$  can be obtained as follows [7]:

$$\delta_j^{tot} = d_j - d'_j \tag{7}$$

By applying the Hertzian contact theory, the normal contact force between the ball and bearing race is as follows [3]:

$$Q_j = K_c^{tot} (\delta_j^{tot})^{3/2} \tag{8}$$

where,  $K_c^{tot}$  refers to the total contact stiffness involving contacts of both races.

2.2. Contact stress

According to the Hertzian contact model, the maximum contact stress occurs at the geometrical center of the contact between the ball and bearing race, which can be found to be [19]:

$$\sigma_{max} = \frac{3Q_j}{2\pi ab} \tag{9}$$

where  $a$  and  $b$  are semi-major/minor axes of the elliptic contact, respectively. The following equations can be used for calculation of  $a$  and  $b$  [20]:

**Table 2**  
Technical specifications of the deep groove ball bearing type 6016.

Bearing parameter	Value
Bearing damping coefficient	0.25 Ns/mm
Bearing diametric clearance	15 $\mu$ m
Outer diameter	125 mm
Ball diameter	19.05 mm
Pitch diameter	110 mm
Bore diameter	80 mm
Modulus of elasticity of ball	$2 \cdot 10^{11}$ Pa
Modulus of elasticity of inner race	$2 \cdot 10^{11}$ Pa
Poisson's ratio of ball	0.3
Poisson's ratio of inner race	0.3
Conformity ratio	0.52
Number of balls	10

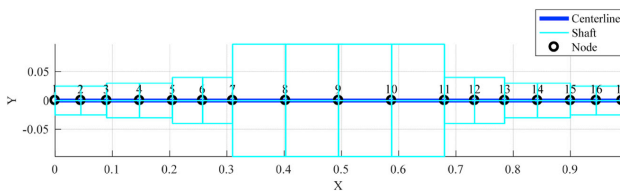


Fig. 4. FE-model of the rotor.

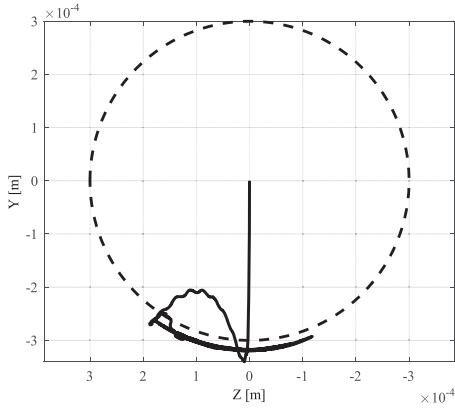


Fig. 5. Orbit of the rotor during the dropdown event.

$$a = \left( \frac{3\kappa^2 \bar{\xi} Q_j R}{\pi E^{eq}} \right)^{1/3}, \quad b = \left( \frac{3\bar{\xi} Q_j R}{\pi \kappa E^{eq}} \right)^{1/3} \quad (10)$$

where,  $E^{eq}$  represents the equivalent modulus of elasticity, given by:

$$\frac{1}{E^{eq}} = \frac{1 - \nu_I^2}{E_I} + \frac{1 - \nu_{II}^2}{E_{II}} \quad (11)$$

where  $\nu$  and  $E$  represent the Poisson's ratio and modulus of elasticity of bodies  $I$  and  $II$  (ball and inner race). The elliptic eccentricity parameter  $\kappa$  and the elliptic integral of the first kind  $\bar{\xi}$  can be computed as follows [21]:

$$\kappa \approx 1.0339 \left( \frac{B}{A} \right)^{0.636} \quad (12)$$

$$\bar{\xi} \approx 1.0003 + 0.5968 \left( \frac{A}{B} \right) \quad (13)$$

The equation that describes the radius of the contact curvature  $R$  given in Equation (10) is as follows [20]:

$$\frac{1}{R} = A + B \quad (14)$$

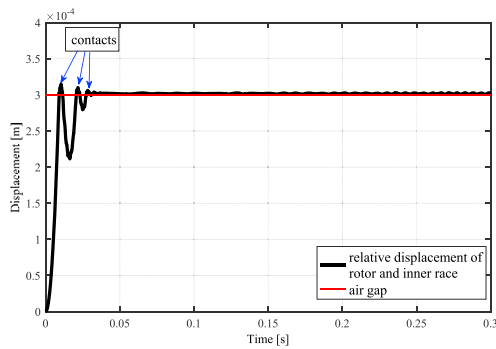


Fig. 6. Relative displacement of the rotor and the inner race.

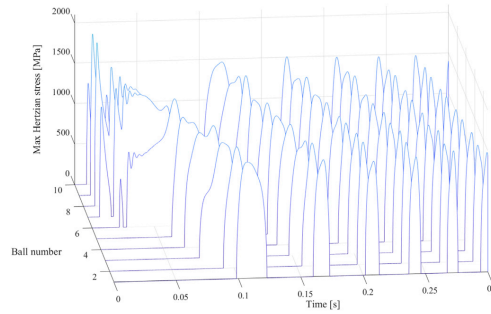


Fig. 7. Maximum Hertzian stress of each ball.

where  $A$  and  $B$  are the principal curvatures of contact in the  $x$  and  $y$ -direction [20].

### 2.3. Model of the contact

The radial contact force  $F_r$  between the rotor and touchdown bearing is computed by modified Hertzian contact theory [4]:

$$F_r = \begin{cases} K \delta^{10/9} (1 + (3/2)\alpha\delta) & ; e_r \geq c_r \text{ and } F_r > 0 \\ 0 & ; e_r < c_r \text{ and } F_r \leq 0 \end{cases} \quad (15)$$

In the equation above,  $K$  represents the contact stiffness between the rotor and inner race, and  $\alpha$  is a contact parameter that for steel ranges between 0.08 and 0.2 [22]. Numerical parameters adopted in this study for the contact between the rotor and touchdown bearing are given in Table 1. In Equation (15),  $\delta$  is the penetration of the rotor in the inner race and it can be calculated from the following equation:

$$\delta = e_r - c_r \quad (16)$$

where  $c_r$  is the radial clearance of the air gap between the rotor and touchdown bearing. The radial displacement of the rotor,  $e_r$ , can be found to be [4]:

$$e_r = \sqrt{e_{x,r}^2 + e_{y,r}^2} \quad (17)$$

where  $e_{x,r}$  and  $e_{y,r}$  are the radial displacement between the rotor and

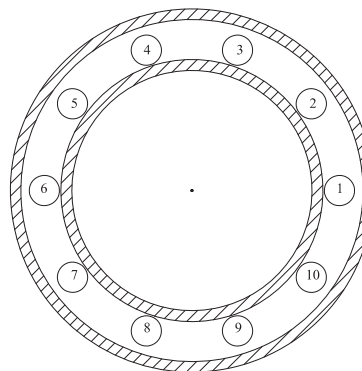


Fig. 8. Ball arrangement at the start of the simulation.

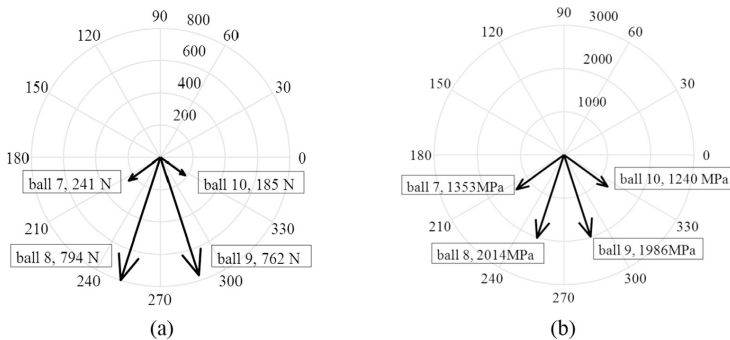


Fig. 9. Distribution of load (a) and stress (b) in the touchdown bearing during the first contact.

inner race in  $x$  and  $y$ -directions. Simulation model also includes the friction force  $F_{\mu}$ , between the rotor and inner race, which can be computed:

$$F_{\mu} = \mu F_r \tag{18}$$

where  $\mu$  is the friction coefficient between the rotor and inner race. The value and sign of the friction coefficient is a function of the relative velocity between the rotor and inner race according to the Coulomb friction law. More details about the friction model in a touchdown bearing can be found in Ref. [3].

In this study, the variation of the maximum Hertzian contact stress in the bearing during the dropdown is obtained. For future studies, the surface and subsurface stress required for calculation of the lifetime of the touchdown bearing can be obtained by applying the contact parameters, the friction model and the maximum Hertzian stress given in Equation (9). It should be noted that during the dropdown event the bearing is not under a steady load, and therefore, the time varying stress counting can be applied for calculation of the bearing life time as presented in Ref. [6].

### 3. Case studies and results

Fig. 3 depicts the main dimensions of the rotor, and the position of the AMBs and touchdown bearings. Table 1 shows the parameters that are used in the simulation of the dropdown event. The FE-model of the rotor is depicted in Fig. 4. The model comprises a total of 16 elements and the AMBs are located at the nodes 6 and 12. Deep groove ball bearings are used as touchdown bearings that are located at nodes 4 and 14 in the FE-model of the rotor. The parameters of the touchdown bearings are shown in Table 2.

The dropdown is simulated for 1 s and the simulation time step is 10  $\mu$ s. The equation of motion is time-integrated using MATLAB ode45. The relative error and maximum step size are equal to  $1 \cdot 10^{-5}$  and  $1 \cdot 10^{-5}$ , respectively [23].

#### 3.1. Stress in a touchdown bearing without an off-sized ball

In the simulation, the penetration of the ball in the inner race is computed from the relative displacements between the inner and outer races. Fig. 5 depicts the rotor's orbit during the dropdown. In this figure, the dashed line shows the air gap and the solid line shows the path of the center of the rotor during dropdown. After the first interaction of the rotor and bearing, the rotor bounces, after which it settles steadily on the bottom of the inner race. Fig. 6 shows the relative displacement of the rotor and inner race. The first contact of the rotor and touchdown bearing occurs at 8.98 ms. After 2 ms, the rotor bounces back and at 20.5 ms the

rotor contacts the inner race for the second time. After the third contact, at 27.06 ms, the rotor remains in continuous contact with the inner race.

Fig. 7 shows the stress history for the contact of each ball and the inner race. The stress history shows that the stresses are not uniformly distributed among the balls. After the first contact, the bearing experiences highest contact stress equal to 2014 MPa. Then, the stresses decline and the differences in the stresses among the balls gradually decreases as the bearing starts rotating. The maximum Hertzian contact stress is experienced in ball number 8, which was initially situated at 252° (Fig. 8).

Fig. 9 depicts the distribution of the load and the stress during the first contact of the rotor and the touchdown bearing. In the first contact, the balls number 7, 8, 9 and 10 penetrate the inner race. These balls are located at phase angles 216°, 252°, 288° and 324°, respectively. The highest stress is experienced in the contact of ball number 8 with the inner race. The contact force of ball number 8 with the inner race is equal to 794 N and the maximum Hertzian stress is 2014 MPa. In the first interaction of the rotor with the touchdown bearing, the total contact force between the rotor and inner race has two components. The vertical component is mainly due to the effect of the weight of the rotor. The friction force between the rotor and inner race is in the tangential direction and acts in the opposite direction to the rotation of the rotor (counterclockwise). Therefore, the total contact force between the rotor and inner race is orientated to the left. For this reason, ball 8 experiences higher contact force than ball 9.

Fig. 10 depicts the maximum Hertzian stress distribution in the maximum penetration of second and third contact of the rotor and inner race. In second and third contacts, ball number 10 is no longer in contact with the inner race. Moreover, the location of the balls has changed. In the second contact, balls 6, 7, 8 and 9 are at 185°, 221°, 257°, and 293° phase angles, respectively (Fig. 10 (a)) and ball number 8 experiences the highest stress. In the third contact, the balls 6, 7, 8 and 9 will move to 191°, 227°, 263° and 299° phase angles (Fig. 10 (b)) and the highest stress is found in the contact of ball number 7 and the inner race. The simulation reveals that in the dropdown event, different balls are in contact with the inner race at different times. Furthermore, the magnitude of the stress and the location of the ball with the highest stress change with the rotation of the balls in the bearing.

#### 3.2. Stress in a touchdown bearing with single off-sized ball

The first contact stress of an individual ball is studied for cases where the studied ball has a greater or smaller diameter with respect to the other balls. The difference in the size of ball affects the contact stiffness and the stresses in the bearing. Additionally, a few cases where a number of balls are assumed to have non-conformance diameters are also studied. The ball arrangement is randomly selected. Detailed information about

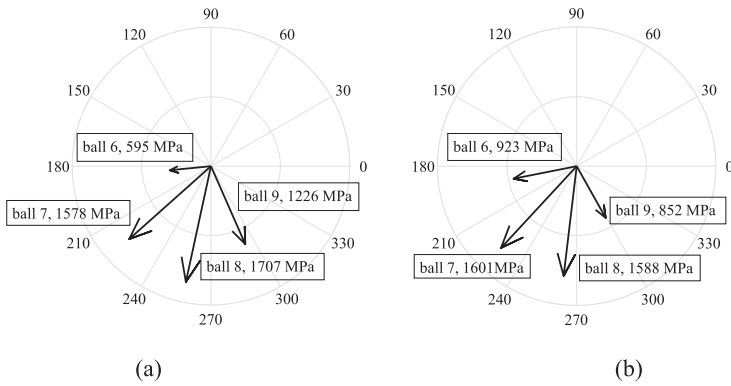


Fig. 10. Maximum Hertzian stress distribution in the second (a) and third (b) contact of the rotor with the inner race.

dimensional tolerance in steel ball bearings can be found in the standard ISO 3290-1 [24]. The off-sized ball with maximum 5 μm deviation from nominal size discussed in Section 3.2.1 would belong to grade G100 in the ISO 3290-1 standard. Section 3.2.2 discusses the effect of an off-sized ball with a dimension smaller than the nominal diameter.

3.2.1. Off-sized ball with diameter greater than nominal size

Ball diameter affects to the Hertzian contact stiffness between the ball and races. It can be shown in Fig. 11 that in the case of an off-sized ball with positive tolerance, the contact stiffness increases 0.29% as the diameter of the ball increases 5 μm from the nominal diameter.

In order to investigate the effect of the off-sized ball on the distribution of the contact force and stress, it is essential to consider the location of the off-sized ball. The location and the number of the balls contacting the inner race vary during the dropdown event. It is assumed that the bearing has a single off-sized ball, and this ball can be in locations 1–10 of Fig. 12. The effect of different location of an off-sized ball on the contact load and the stress of the balls carrying the load during the first interaction of the rotor with the inner race can be studied. In the first interaction of the rotor and touchdown bearing, balls 7, 8, 9 and 10 penetrate into the inner race (Fig. 12).

The effect of the location and size of the single off-sized ball on the contact stress of ball 8 is depicted in Fig. 13. The influence of the dimension of the off-sized ball on balls under load is also presented. As can be seen in Fig. 13 (a), when the off-sized ball is located in an

unloaded zone (locations 1–6 of Fig. 12) the increased diameter of the off-sized ball does not significantly affect the contact force of ball number 8. When the off-sized ball is in the loaded zone (lower half of the bearing) and is far from ball 8 (location 10) there is a small effect on the contact force and stress on ball 8 (mainly for the off-sized ball up to 3 μm). When ball 8 itself is off-sized, a clear increase in the contact load and stress can be observed. For an off-sized ball in other locations in the loaded zone (location 7 or 9), the increased diameter of the off-sized ball decreases the maximum Hertzian stress in the ball number 8 (Fig. 13 (b)). This reveals that the highest stress occurs in the location of the off-sized ball, while the stress in the adjacent balls decreases, which is compatible with previous research on the load distribution of off-sized balls in deep groove ball bearings [14]. In the matter of off-sized ball in the loaded zone, the load distribution in the bearing is different from the bearing with nominal size. Initially, the off-sized ball with a greater diameter than other balls contacts the inner ring. Then, the other balls will be in contact with the inner ring. Furthermore, a certain amount of energy is transferred from the kinetic energy of the rotor to the deformation of the bearings. When the off-sized ball is in the loaded zone, the off-sized ball experiences higher load while the other balls carry less load since the total amount of energy transferred in the bearing is not changing. Moreover, with the off-sized ball, the internal radial clearance in the bearing is decreased locally and causes the relative higher stiffness. Therefore, the contact force between the ball and bearing race is increased. The higher load in the off-sized ball leads to the higher contact

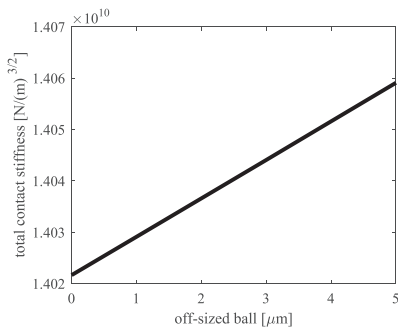


Fig. 11. Total contact stiffness in a touchdown bearing with a single off-sized ball.

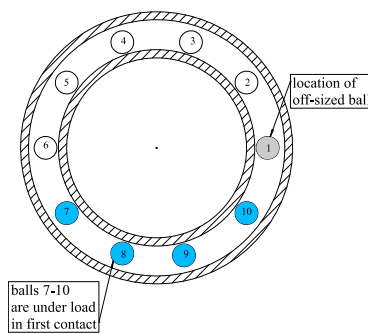


Fig. 12. Location of the single off-sized ball and balls under load first contact.

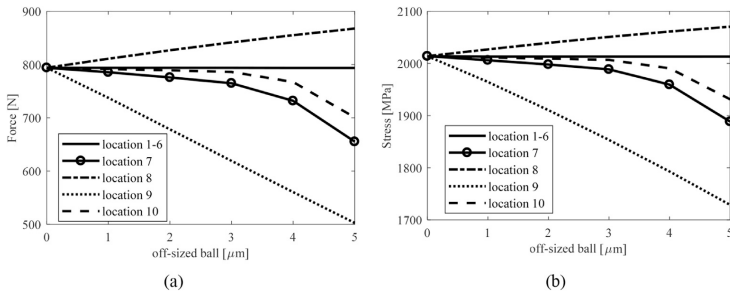


Fig. 13. Maximum contact force and Hertzian contact stress in ball number 8 during the first contact in cases where the off-sized ball is located in locations 1–10 in the bearing arrangement in Fig. 8.

stress. This can provide a physical explanation that why the highest stress occurs in the location of the off-sized ball.

3.2.2. Off-sized ball with dimension smaller than nominal size

The diameter of an off-sized ball can also be less than the nominal diameter. The approach presented in Section 3.2.1 can be implemented to study the effect of an off-sized ball with a diameter smaller than the nominal diameter. In this case, the radii of the curvature of the off-sized ball is smaller than the curvature of a ball of nominal size. Therefore, the contact stiffness is decreased. Table 3 shows the stresses in the balls carrying the load during the first contact as a result of a single off-sized ball having a diameter 2 μm smaller than the nominal diameter of the ball. In this case, the conformity ratio of the off-sized ball increases to 0.5201. The total contact stiffness of the off-sized ball is 0.105% less than the contact stiffness of the other balls. As with the previous case of a ball with a diameter greater than the nominal size, the location of the off-sized ball influences the stress in the balls carrying the load. When the off-sized ball is in the locations 1–6 (Fig. 12), the stress is the same as the stress of the balls with nominal size. When the off-sized ball is located in the location 8, the contact stress of the ball number 8 is reduced to 1906 MPa. A similar pattern is observed for the off-sized ball in locations 7, 9 and 10. The presence of a single off-sized ball with a diameter smaller than the nominal size reduces the stress of the ball being studied but increases slightly the stresses in the neighboring balls. In the case where the diameter of the off-sized ball (ball 8) was larger than the nominal size, the stress in ball 8

Table 4  
Stress in the touchdown bearing with multiple off-sized balls.

Multiple off-sized balls 5 μm					Single off-sized ball 5 μm
Ball under load	Nominal diameter	Ball 1, 6, 8	Ball 2, 5, 9	Ball 7, 8, 9	Ball 8
7	1353	1027	1107	1486	1027
8	2014	2070	1729	1994	2071
9	1986	1697	2047	1991	1698
10	1240	977	890	897	976

increased (Fig. 13). The off-sized ball in the loaded zone of the bearing and having a smaller diameter than nominal size causes the load distribution in the bearing will be different from the nominal size of the ball. First, the balls with nominal size contact the inner ring and then the off-sized ball. This causes that the balls with the nominal size carry the higher load. As the total amount of energy is not changed the off-sized ball experiences lower force. Besides, the off-sized ball smaller than nominal diameter increases the radial clearance, locally. Hence, the contact stiffness between the off-sized ball and bearing race is reduced and the contact force is less than the balls having a nominal diameter. It should be noted that several features are affected by the presence of an off-sized ball in the bearing, including the contact stiffness, total elastic deformation of the inner race, as well as the semi-minor/major of the elliptical contact area.

Table 3  
Stress in a touchdown bearing with a single sized ball with smaller diameter than nominal size, MPa.

Single off-sized ball (-2 μm)						
Ball number	Nominal diameter	Location 1-6	Location 7	Location 8	Location 9	Location 10
7	1353	1353	1158	1391	1362	1345
8	2014	2014	2025	1906	2034	2017
9	1986	1986	1989	2010	1873	1996
10	1240	1240	1230	1252	1279	1021

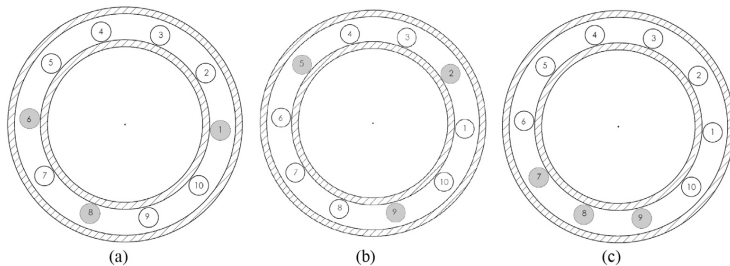


Fig. 14. Studied arrangements of multiple off-sized balls deviating 5 μm from the nominal size.

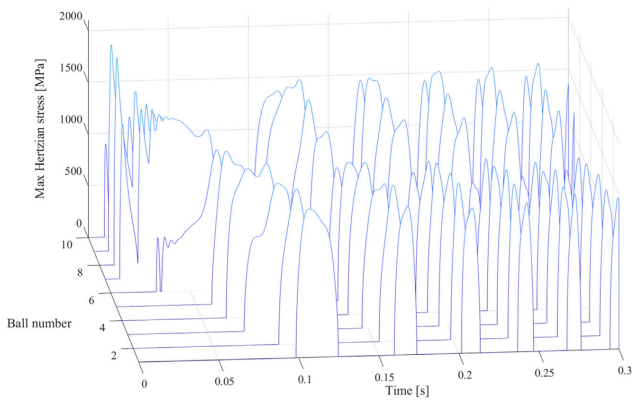


Fig. 15. Maximum Hertzian stress in each ball for the multiple off-sized balls.

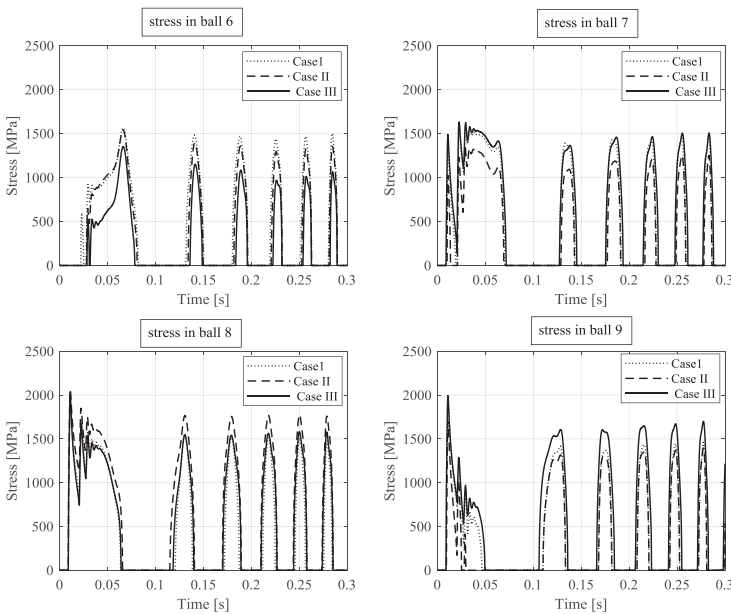


Fig. 16. Maximum Hertzian stress in balls 6, 7, 8 and 9. Case I: without off-sized ball, Case II: single off-sized ball (ball 8), Case III: multiple off-sized balls (ball 7, 8, 9).

3.3. Multiple off-sized balls

In practical applications, more than one off-sized ball might be present in the touchdown bearing and these balls can be in different arrangements. A touchdown bearing having three off-sized balls (+5 μm) located in the arrangements shown in Fig. 14 was studied. The effects of the stresses on the load carrying balls (in the first contact) are shown in Table 4. In all arrangements shown in Fig. 14, the bearing carries the same magnitude of the load. With the 5 μm off-sized balls, the conformity ratio is 0.51986. This results in contact stiffness of the off-sized ball being larger than in the case of conformant balls. When two off-sized balls are located in the unloaded zone (Fig. 14 (a) and (b)), one of the three off-

sized balls carries the highest load similarly as in the case of a single off-sized ball. The increase in stress is not very high and the stresses are similar to those of the single off-sized ball as described in Section 3.2.1. When all the off-sized balls are located in the loaded zone (Fig. 14 (c)), the difference in the stresses in the balls carrying load becomes even smaller. In this case, balls 8 and 9 carry similar stress. Multiple off-sized balls in the loaded zone cause less change in the stress experienced by the ball carrying the load than with a single off-sized ball.

The variation of the stresses in the contact of the ball and inner ring for the case where multiple off-sized balls exist in the bearing is shown in Fig. 15 where the balls 7, 8 and 9 are 5 μm off-sized. As shown in Fig. 14 (c) these balls are initially located on the lower half of the bearing. In this case, the

difference in the stress in the balls, mainly located in the loaded zone, has been observed. In order to have a more clear feature about the variation of the stress in the matter of the bearing with and without off-sized balls, Fig. 16 shows the maximum Hertzian stress in the balls carrying the load (ball 6, 7, 8 and 9) for three different cases: Case I: balls with nominal dimension, Case II: single off-sized ball (ball 8) and Case III: multiple off-sized balls (balls 7, 8 and 9). It can be found that when the off-sized ball is in the loaded zone of bearing, the time where the ball contacts with inner race is changed and the variation of the stress can be clearly observed. The balls numbered 1–5, which are in the upper half of the bearing do not experience a significant difference in the stress. Furthermore, the variation of the stress in ball 10 was not considerable and therefore it is not shown.

#### 4. Conclusions

The stresses during dropdown in a touchdown bearing of an AMB-supported rotor with off-sized balls were modeled using a numerical simulation. In this study, the system under investigation comprised of a flexible rotor, two AMBs and touchdown bearings. The touchdown bearings of the deep groove ball bearing type were modeled using a simplified ball bearing model. The flexible rotor was simulated by finite element method employing Timoshenko beam elements. This study evaluated the Hertzian contact stresses in the touchdown bearing. The contact stresses in the touchdown bearing are influenced by the dimensional tolerances, properties of the material used in touchdown bearing as well as the dynamic behavior of rotor. The stress history of the touchdown bearing was obtained. The study considered a variation of ball diameter based on the standard ISO 3290 for the size of the balls. Contact stiffness and bearing stresses were obtained from simulations in which the size and location of the off-sized balls were varied. The results showed that the normal contact forces are not uniformly distributed among all the balls of the touchdown bearing. In the first contact, the balls that are initially located in the loaded zone of the bearing experience higher stress. Furthermore, the dimension of the off-sized ball affects the highest contact stress in the bearing. Increasing the size deviation of the off-sized ball from one to five micrometers causes an increase in the contact stiffness between the balls and bearing race. When a single off-sized ball was located in the unloaded zone of the bearing, minimum change in the stress compared to the stress in the bearing with nominal size balls was found. The results showed that with off-sized balls within acceptable tolerance limits for chrome steel balls defined in standard ISO 3290-1, the change in Hertzian stress is not significant, although clearly observable.

#### Acknowledgment

The authors would like to thank Academy of Finland for funding

under the VIDROM project (grant number 277502).

#### References

- [1] Schmied J, Pradetto JC. Behaviour of a one ton rotor being dropped into auxiliary bearings. In: Proceeding of the third international symposium on magnetic bearings, Alexandria; 1992. p. 145–56.
- [2] Keogh PS. Contact dynamic phenomena in rotating machines: active/passive considerations. *Mech Syst Signal Process* 2012;29:19–33.
- [3] Kärkkäinen A, Sopenan J, Mikkola A. Dynamic simulation of a flexible rotor during drop on retainer bearings. *J Sound Vib* 2007;306:601–17.
- [4] Halminen O, Kärkkäinen A, Sopenan J, Mikkola A. Active magnetic bearing-supported rotor with misaligned cageless backup bearings: a dropdown event simulation model. *Mech Syst Signal Process* 2015;50–51:692–705.
- [5] Sun G. Auxiliary bearing life prediction using Hertzian contact bearing model. *ASME Journal of Vibration and Acoustics* 2006;128(2):203–9.
- [6] Lee JG, Palazzolo A. Catcher bearing life prediction using a rainflow counting approach. *ASME Journal of Tribology* 2012;134(3), 031101.
- [7] Kurvinen E, Sopenan J, Mikkola A. Ball bearing model performance on various sized rotors with and without centrifugal and gyroscopic forces. *Mech Mach Theor* 2015; 90:240–60.
- [8] Jin C, Wu B, Hu Y. Heat generation modeling of ball bearing based on internal load distribution. *Tribol Int* 2012;45:8–15.
- [9] Chen G, Mao F, Wang B. Effects of off-sized cylindrical rollers on the static load distribution in a cylinder roller bearing. *Proc IME J J Eng Tribol* 2012;226(8): 687–96.
- [10] Gupta PK. Frictional instabilities in ball bearings. *Tribol Trans* 1988;31:258–68.
- [11] Aktürk N, Gohar R. The effect of ball size variation on vibrations associated with ball-bearings. *Proc IME J J Eng Tribol* 1998;212:101–10.
- [12] Harsha SP. Nonlinear dynamic analysis of rolling element bearings due to cage run-out and number of balls. *J Sound Vib* 2006;289:360–81.
- [13] Wardle FP. Vibration forces produced by waviness of the rolling surfaces of thrust loaded ball bearings. Part 1: Theory. *Proc IME C J Mech Eng Sci* 1988;202:305–12.
- [14] Zhou X, Xu H, Xiong X, Wang L. Load distribution model of deep groove ball bearing with ball off size. In: *IEEE International Symposium on Assembly and Manufacturing (ISAM)*; 2013. p. 58–63.
- [15] Oswald FB, Zaretsky EV, Poplawski JV. Effect of internal clearance on load distribution and life of radially loaded ball and roller bearings. *Tribol Trans* 2012; 55:245–65.
- [16] Zhou X, Xu H, Xiong X, Wang L. Effect of ball off size on fatigue life of deep groove ball bearing. In: *IEEE International Symposium on Assembly and Manufacturing (ISAM)*; 2013. p. 64–8.
- [17] Kärkkäinen A. Dynamic simulations of rotors during drop on retainer bearings. Ph.D. thesis, Lappeenranta University of Technology; 2007.
- [18] Sopenan J, Mikkola A. Dynamic model of a deep-groove ball bearing including localized and distributed defects. Part 1: theory. *Proc Inst Mech Eng - Part K J Multi-body Dyn* 2003;217:201–11.
- [19] Harris TA, Kotzalas MN. *Essential concepts of bearing technology: rolling bearing analysis*. fifth ed. CRC Press; 2007.
- [20] Greenwood JA. Analysis of elliptical Hertzian contacts. *Tribol Int* 1997;30:235–7.
- [21] Brewe DE, Hamrock BJ. Simplified solution for elliptical-contact deformation between two elastic solids. *ASME J Lubric Technol*. 1977;99(4):485–7.
- [22] Sun GY. Rotor drop and following thermal growth simulations using detailed auxiliary bearing and damper models. *J Sound Vib* 2006;289(1–2):334–59.
- [23] Sikanen E, Halminen O, Heikkinen J, Sopenan J, Mikkola A, Matikainen M. Stresses of an AMB-supported rotor arising from the sudden contact with backup bearings. In: *ASME International Mechanical Engineering Congress and Exposition, 4A*; 2015. p. 51373.
- [24] ISO 3290-3291 Rolling bearings – balls – Part 1: steel balls. 2008.

## **Publication II**

Neisi, N., Heikkinen, J., Sapanen, J.

**Influence of surface waviness in the heat generation and thermal expansion of the touchdown bearing.**

Reprinted with permission from  
*European Journal of Mechanics / A Solids*

74 (2019) 34–47

© 2019, Elsevier.





Contents lists available at ScienceDirect

European Journal of Mechanics / A Solids

journal homepage: [www.elsevier.com/locate/ejmsol](http://www.elsevier.com/locate/ejmsol)

## Influence of surface waviness in the heat generation and thermal expansion of the touchdown bearing

Neda Neisi<sup>\*</sup>, Janne E. Heikkinen, Jussi Sopanen

Department of Mechanical Engineering, Lappeenranta University of Technology, Skinnarilankatu 34, 53850, Lappeenranta, Finland

## ARTICLE INFO

## Keywords:

Touchdown bearing  
Rotor  
Dropdown  
Friction  
Thermal analysis  
Waviness

## ABSTRACT

In an active magnetic bearings (AMBs) supported rotor system, the touchdown bearings have been proposed to support the rotor during an electromagnetic field shortage. The heat generation due to the high impact and collision of the rotor and touchdown bearing, in addition to the internal friction in the bearing, raises the temperature of the touchdown bearing. In this work, a numerical model is applied to simulate the rotor drop-down where the FE-model of the rotor is integrated with the dynamic and thermal model of the touchdown bearing. The rotor that is used as a case study is supported by a deep groove ball bearing and a pair of angular contact ball bearings installed in an X-configuration. The present study focuses on evaluating different orders of surface waviness in a pair of angular contact ball bearings. The equivalent electrical circuit model is implemented for computing the thermal behavior of the touchdown bearing. Results indicated that the dynamic friction coefficient between the rotor and inner race has a considerable impact on bounce height and the whirling motion of the rotor. Furthermore, for a certain amplitude of surface waviness, the effect of various orders of waviness is investigated and it has been found that surface waviness of the bearing alters the contact force and friction loss in the touchdown bearing. In addition, the effect of a higher amplitude of surface waviness on thermal expansion of the touchdown bearing is studied.

## 1. Introduction

The field of rotating electric machines has experienced a dramatic change from constant rotational speed machines to variable speed machines controlled by a frequency converter. Simultaneously, the rotational speeds have increased due to the advantages of higher rotational speeds. The highest rotational speeds can be achieved when the rotor can be rotated freely without mechanical contact with any other parts, even the bearings. This can be achieved using airfoil bearings that levitate the rotor on the air film, but this solution requires high rotational speeds to function and still the aerodynamic losses are noteworthy. The solution that is more promising is to levitate the rotor using a controlled electromagnetic field. In the active magnetic bearings (AMBs) supported system, electromagnetic forces levitate the rotor. The system does not suffer from wear due to this no-contact operation. Therefore, the AMBs are the preferred choice in high-speed applications compared to other bearing types. Nevertheless, an AMB system requires a backup system for preventing fatal failures in case the electromagnetic field is lost due to electric short circuit or error in the control system.

Several studies have been conducted on rotor and touchdown

bearing contact. As demonstrated by Kärkkäinen et al. (2007) and Ecker (1998), the high collision and friction forces in the dropdown will influence the whirling motion of the rotor. The nonlinear dynamic model of rotor casing rub has been extensively studied during the last century. A few well-known studies on rotor rub were performed by Taylor (1924), Newkirk (1926) and Childs (1979). Choy and Padovan (1987) developed a theoretical model on the relation between rub force histories, energy levels, rub duration, incidence separation angles, as well as initiation of backward whirling. Muszynska (1984), studied the rotor-stator rub theoretically and experimentally. Keogh (Keogh, 2012; Keogh and Yong, 2007) studied the contact of the rotor and the touchdown bearing, thermal bending of the rotor, and the effect of open loop and closed loop control systems for recovering the rotor levitation on AMBs. Recently, Liu et al. (2018) developed a method based on signal processing to identify the orbit response of an AMB supported rotor during the bounce, and rub in the touchdown bearings. They applied the Fourier transform to identify the pendulum vibration and the full rub of the rotor. The previous study on the experimental and numerical rotor drop investigated by Schmied and Pradetto (1992) indicated that because of the presence of electromagnetic force at the start of the dropdown test and also the time lag in the control system,

<sup>\*</sup> Corresponding author.

E-mail addresses: [neda.neisi@lut.fi](mailto:neda.neisi@lut.fi) (N. Neisi), [janne.e.heikkinen@lut.fi](mailto:janne.e.heikkinen@lut.fi) (J.E. Heikkinen), [jussi.sopanen@lut.fi](mailto:jussi.sopanen@lut.fi) (J. Sopanen).

<https://doi.org/10.1016/j.euomechsol.2018.10.014>

Received 3 April 2018; Received in revised form 10 September 2018; Accepted 19 October 2018

Available online 25 October 2018

0997-7538/ © 2018 Elsevier Masson SAS. All rights reserved.

the numerical result can deviate from the outcome of the experimental test.

Even though there has been considerable advancement in bearing technology, several cases of thermal failures of the bearings have been reported (Burton and Staph, 1967; Takabi and Khonsari, 2016). The reported failures were due to the rapid growth of the thermal induced preload and high-temperature gradient in the bearing. This type of failure can occur even without a considerable change in the vibration levels (Takabi and Khonsari, 2016). Numerous publications implemented the equivalent electrical circuit to study the heat transfer in the touchdown bearings (Sun, 2006a, 2006b; Lee and Palazzolo, 2012; Zhao et al., 2016; Jin et al., 2015). Takabi and Khonsari, 2013, 2016 developed an experimental setup to evaluate the temperature in the conventional deep groove ball bearing. The experimental setup enabled them to investigate the variation of temperature under different speeds and operating conditions. The touchdown bearings utilized in an AMB supported rotor differ from the conventional rotor bearing system and the differences have been demonstrated in paper by Neisi et al. (2018). Due to the complicated geometry of the bearing assembly and the change in the heat generation rate, some simplifications for the boundary conditions and the model might be required. Accordingly, the result of the analytical solution might be slightly different from the experimental result (Jin et al., 2012). In addition to the single-row bearings, the thermal analysis of double-row bearings has been studied. Yan et al. (2015) and Ai et al. (2015) performed the thermal analysis of the double-row tapered roller bearing. Jin et al. (2015) compared the thermal structure of the single-decker and double-decker touchdown bearings. They presented a model for improving the rotational speed of the intermediate race of the double-decker ball bearing. They concluded that the double-decker configuration decreases the temperature rise in the touchdown bearing. The aforementioned publications on the thermal model of the touchdown bearing presume that the bearing is installed in an ideal condition. However, as a result of the surface waviness, particularly due to the wear between rotor and touchdown bearing in the previous dropdown of the rotor, the friction torque and the power loss calculated for the thermal model of the touchdown bearing can be different from the ideal condition of the bearing. As stated in the standard API 617, the touchdown bearing should withstand a minimum of two full dropdowns from maximum continuous speed to zero speed and a minimum of ten partial contacts due to disturbances in the system exceeding the force capacity of the AMBs (Xial and Centrifuga, 2002).

The waviness in the bearing can be considered as one of the main reasons for bearing vibration. There are numerous studies about

bearing waviness in a conventional ball bearing. Zhuo et al. (2014) evaluated the influence of applied load, internal clearance, number of balls as well as surface waviness on the kinematic behavior of a double-row self-aligning ball bearings. They described the vibration characteristic of the rotor bearing system including surface waviness in the bearing races. The influence of the surface waviness on the stability of a rigid rotor supported by ball bearings is presented in a paper by Harsha and Kankar (2004). They showed that the nonlinear vibration response of the rotor bearing system due to the surface waviness in the bearing system is highly affected by the number of balls and order of waviness. In addition, they pointed out that by increasing the number of balls, the stiffness of the system will be higher and the influence of ball pass frequency decreases. Wardle, 1988a, 1988b conducted both a mathematical and experimental study on the frequency response and vibration analysis of the bearing having surface waviness. The study by Changqing and Qingyu (2006) on the effect of internal clearance and waviness includes the high-speed effect, and their work indicated that the waviness causes the change in the frequency of the peak of amplitude. Liu et al. (2014) developed a multibody dynamic model for a ball bearing. They found that as a consequence of the high-speed effect in the bearing, the waviness in the outer race has a higher influence on the vibration of the system rather than the waviness in the inner race. The aforementioned publications on the surface waviness in the bearing mainly discuss the influence of surface waviness, theoretically. A recent paper by Heikkinen et al. (2018) evaluates the vibration analysis of a spherical roller bearing from surface waviness both experimentally and numerically.

Few studies have focused on the influence of the waviness in touchdown bearing application. Recently, Halmnen et al., 2017a, 2017b developed a multibody model of the touchdown bearing including surface waviness. They investigated the effect of 1<sup>st</sup>, 2<sup>nd</sup> and 3<sup>rd</sup> order surface waviness in the bearing races in the calculation of the friction loss in the touchdown bearing. It is possible to acquire further improvement in the touchdown bearing design by considering the influence of the surface waviness in the dynamic and thermal model of the touchdown bearing. With this goal, the present study aims to apply the simple model for the ball bearing to evaluate the contact force and power loss in a rotor drop. Moreover, the influence of friction heat generated in the touchdown bearing due to different orders of surface waviness in bearing rings will be identified. Furthermore, this work presents the impact of the waviness on the temperature rise in the bearing during rotor drop.

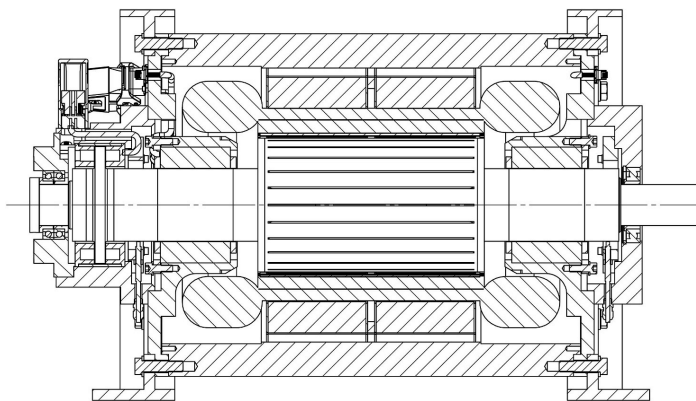


Fig. 1. A case study of the electric motor.

## 2. Model of the rotor

The FE-model of the rotor of a high-speed electric motor depicted in Fig. 1 has been constructed based on the shear deformable Timoshenko beam element that was used for rotating shafts by Nelson (1980). In regular operation of the machine, the rotor is levitated in the electromagnetic field and AMBs carry the weight of the rotor and the operational loads. The equation of motion of the system can be written as:

$$\mathbf{M}\ddot{\mathbf{X}} + (\mathbf{C} + \omega\mathbf{G})\dot{\mathbf{X}} + \mathbf{K}\mathbf{X} = \omega^2\mathbf{Q}_1 + \mathbf{Q}_2 \quad (1)$$

In the equation of motion,  $\mathbf{M}$  defines the mass matrix,  $\mathbf{C}$  is damping matrix and  $\mathbf{K}$  represents the stiffness matrix. The gyroscopic matrix is denoted by  $\mathbf{G}$ . The vector of the generalized coordinate is shown by  $\mathbf{X}$ . The vector  $\mathbf{Q}_1$  is vector of nodal unbalance and the vector of externally applied force is denoted as  $\mathbf{Q}_2$  and  $\omega$  is the angular rotation speed of the rotor.

## 3. Model of a touchdown bearing

The touchdown bearings are simulated utilizing the model for the ball bearing developed by Sapanen and Mikkola (2003). The relative displacement between bearing rings is as follows:

$$\begin{aligned} e_x^j &= e_x \cos \beta_j + e_y \sin \beta_j \\ e_z^j &= e_z - (\psi_x \sin \beta_j + \psi_y \cos \beta_j)(R_{in} + \varepsilon_{in} + r_{in}) \end{aligned} \quad (2)$$

where  $e_x$ ,  $e_y$  and  $e_z$  feature the relative displacements between the bearing races along main axes. The index  $j$  represents the ball number.  $\beta_j$  is the azimuth angle of  $j$ th ball. In Fig. 2, the inner race radius and inner race groove radius are denoted as  $R_{in}$  and  $r_{in}$ , respectively. The tilting of the inner race in principle directions are denoted as  $\psi_x$  and  $\psi_y$ . The distance between the bearing rings is given by:

$$D_j = r_{out} + r_{in} - \frac{(R_{in} + \varepsilon_{in}) + r_{in} + e_z^j - (R_{out} + \varepsilon_{out}) + r_{out}}{\cos \varphi_j} \quad (3)$$

where the contact angle is denoted as  $\varphi_j$ :

$$\varphi_j = \tan^{-1} \left( \frac{e_z^j}{R_{in} + \varepsilon_{in} + r_{in} + e_z^j - R_{out} - \varepsilon_{out} - r_{out}} \right) \quad (4)$$

where  $\varepsilon_{in}$  and  $\varepsilon_{out}$  represent the thermal expansion of the inner race and outer race, respectively. In the dropdown, based on the relative displacement of the rotor and inner ring, the contact angle,  $\varphi_j$ , can be slightly different from the nominal contact angle of the bearing mentioned in the bearing catalogue.

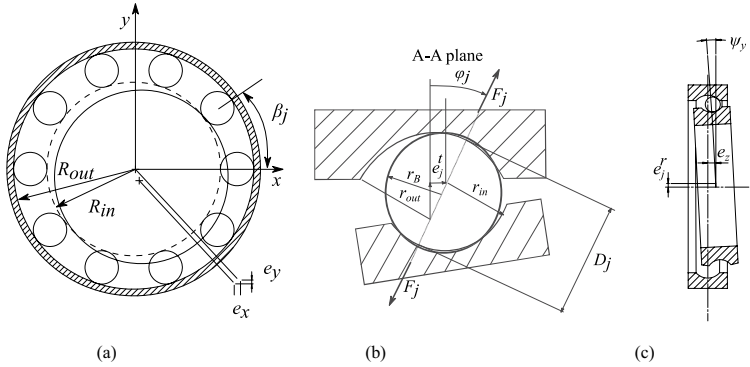


Fig. 2. Cross-section of the ball bearing.

The total elastic deformation of the inner race is as follows:

$$\delta_j^{tot} = d_j + \varepsilon_b - D_j \quad (5)$$

where  $\varepsilon_b$  is thermal expansion of balls. Then, the contact force between ball  $j^{th}$  and inner race can be obtained by Hertzian contact theory (Kärkkäinen et al., 2007):

$$F_j = K_b (\delta_j^{tot})^{3/2} \quad (6)$$

The detailed calculation of total contact stiffness,  $K_b$ , is presented in previous publications (Sapanen and Mikkola, 2003).

### 3.1. Model of the contact

The radial contact force between rotor and touchdown bearing is calculated based on the nonlinear contact model introduced by Hunt and Crossley (1975) and the energy dissipation during the impact is taken into account:

$$F_j = \begin{cases} K\delta^n + b\delta^n\dot{\delta}^q & ; e_r > c_r \text{ and } F_j > 0 \\ 0 & ; e_r \leq c_r \text{ and } F_j \leq 0 \end{cases} \quad (7)$$

where  $K$  represents the contact stiffness between the rotor and inner race,  $q = 1$  and  $n$  is a constant dependent on the type of the contact (for the contact between the rotor and touchdown bearing  $n = 10/9$ ) and  $\dot{\delta}$  is the rate of indentation. The damping parameter ( $b$ ) can be related to the coefficient of restitution which is defined as the ratio of relative velocity before and after collision of the bodies. Hunt and Crossley (1975) showed that  $b = \frac{2}{3}\lambda K$  and they pointed out that the contact parameter  $\lambda$  ranged between 0.08 and 0.32 s/m can be reasonable. If  $\lambda$  is very low, the material will be very resilient. On the other hand, very large value of  $\lambda$  as 0.64 s/m can raise questions in the assumption for deriving  $b = \frac{2}{3}\lambda K$  and might not be appropriate. This method has been also used in simulation of the dropdown by Sun (2006b). For the steel the coefficient  $\lambda$  ranges 0.08 and 0.2 (Sun, 2006b). In present study the contact parameter  $\lambda$  equal to 0.08 has been used in the simulation.

The penetration of the rotor in the inner race can be obtained as:

$$\delta = e_r - c_r + \varepsilon_{in} \quad (8)$$

where the radius of the air gap between the rotor and touchdown bearing is denoted as  $c_r$ . In the modified Hertzian contact model, the velocity of penetration of the rotor in the touchdown bearing,  $\dot{\delta}$ , has been taken into account. The following equation can be used to obtain the radial displacement of the rotor (Kärkkäinen et al., 2007):

$$e_r = \sqrt{e_{x,r}^2 + e_{y,r}^2} \quad (9)$$

where the radial displacement between the rotor and the inner race along the  $x$  - and  $y$  -axis are denoted as  $e_{x,r}$  and  $e_{y,r}$ . The friction force between the rotor and inner race is given by:

$$F_{\mu} = \mu F_r \tag{10}$$

where  $\mu$  is the friction coefficient between the rotor and inner race. The comparative study on the effect of the friction coefficient and the friction model in the simulation of the rotor dropdown presented in the study of Kärkkäinen et al. (2007) indicated that the Coulomb Mohr friction model with the constant friction is able to provide acceptable results for the dynamic simulation of rotor dropdown. The assumption of constant friction coefficient has been made for the simulation since, the dropdown occurs in a short time interval and it was expected that not significant change in friction coefficient happens. Furthermore, the sensitivity analysis for the influence of different values of the dynamic friction coefficient on the temperature rise of inner ring of touchdown bearing shows that there is a small change in the temperature rise of inner ring due to increasing the friction coefficient (Jin et al., 2015). It is important to note that the friction coefficient is not the only parameter affecting the heat generation in the touchdown bearing and the temperature rise is influenced by additional parameters as: geometry and structure of rotor, bearing and support properties as well as the angular velocity of rotor in the start of dropdown.

Considering the contact model and the bearing model introduced earlier, the mechanical model for the interaction of the rotor and touchdown bearing is introduced in Fig. 3.  $F_r$  and  $F_{\mu}$  are the normal and tangential force in the contact of the rotor and touchdown bearing. The forces can be obtained from equations (7) and (10) respectively.  $K_{sup}$  and  $C_{sup}$  represent the support stiffness and damping. The damping of the bearing  $C_b$  typically ranges  $(0.25-2.5) \cdot 10^{-5}$  bearing stiffness  $K_b$  (N/ $\mu\text{m}$ ) (Krämer, 1993). Defining the support stiffness and damping parameters is not straightforward, but they can be obtained experimentally or using FE analysis.  $M_f$  is friction drag torque (load dependent friction torque) that will be demonstrated in section 3.4.  $\omega_i$  and  $\omega_r$  represent the angular velocity of inner race and rotor, respectively.

### 3.2. Modeling of surface waviness

The waviness imperfection refers to the dimensional irregularity where the bearing surface periodically deviates from the nominal

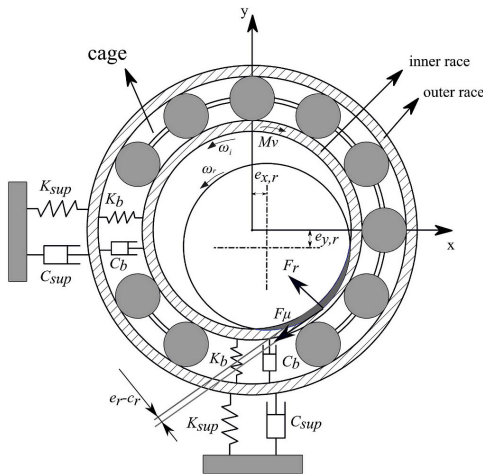


Fig. 3. Mechanical model for interaction of the rotor and touchdown bearing.

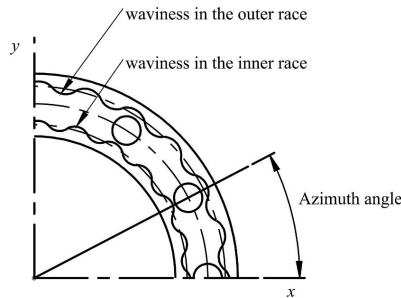


Fig. 4. Model of surface waviness in bearing races.

dimension. Hence, it can influence the total elastic deformation of the bearing race. Consequently, it can change the contact force in the touchdown bearing. The surface waviness in the bearing can be modeled using the sinusoidal function as follows:

$$A_{in} = A \sin(m\beta) \tag{11}$$

where  $A$  is amplitude,  $m$  is order of waviness and  $\beta$  is azimuth angle of the bearing (Fig. 4).

Therefore, the elastic deformation of the bearing race can be rewritten as:

$$\delta_j^{tot} = d_j + \varepsilon_0 - D_j + \sum_{N_w=1}^n A_m^{in} \sin(m^{in}(\beta) + \theta_{inw}) + \sum_{N_w=1}^n A_m^{out} \sin(m^{out}(\beta) + \theta_{ow}) \tag{12}$$

where  $m$  is waviness order and  $\theta_{inw}$  and  $\theta_{ow}$  are the phase angles of  $m^{th}$  order waviness of the inner race and outer race, respectively. In practice, it is possible that the surface waviness in the bearing will be a combination of different waves. Therefore, the amplitudes of the various number of waves ( $n$ ) are summed.

### 3.3. Bearing kinematic

In the high-speed bearing, the spinning of the ball around its axis can be considered as one of the sources of the friction generated in the bearing. Applying the instant center of velocity and trigonometry relation, the spinning velocity of the ball can be derived (Eschmann, 1985). The angular speed of the ball in the contact area between ball/inner race ( $\omega_{ci}$ ) and ball/outer race ( $\omega_{co}$ ) intersect each other at the point  $P$  along the axis of the bearing (Fig. 5).

The spinning velocity in the contact of ball and bearing races is as follows (Hamrock and Dowson, 1981):

$$\begin{aligned} \omega_{ci} &= -\omega_b \sin(\varphi_i - \theta) + \omega_{ci} \sin(\varphi_i) \\ \omega_{co} &= \omega_b \sin(\varphi_o - \theta) + \omega_{co} \sin(\varphi_o) \end{aligned} \tag{13}$$

where  $\varphi_i$  and  $\varphi_o$  represents the contact angle in inner race and outer race, respectively. The ball pitch angle is denoted as  $\theta$ :

$$\tan \theta = \frac{\sin \varphi_o}{\cos \varphi_o + d_b/d_m} \tag{14}$$

and  $\omega_b$  is the angular speed of ball and it can be calculated as follows (Nguyen-Schäfer, 2016):

$$\omega_b = \frac{\omega_{co}(d_m + d_b \cos \varphi)}{d_b} \tag{15}$$

where  $d_b$  and  $d_m$  represent the ball diameter and pitch diameter, correspondingly.

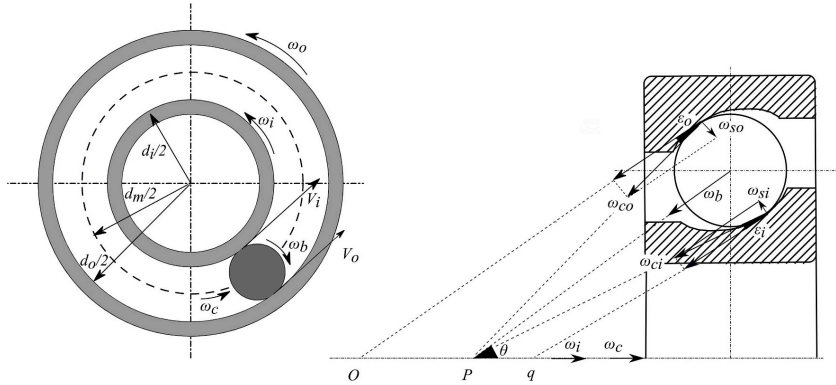


Fig. 5. Spinning velocity in the ball bearing.

3.4. Thermal model of bearing

In the touchdown bearing, heat transfers by both conduction and convection heat transfer mechanisms. The friction between the rotor and the inner race, and also the friction heat generated between the ball and bearing races, are considered as heat sources. Previous studies (Lee and Palazzolo, 2012; Zhao et al., 2016; Jin et al., 2015; Sun, 2006b) presented the one-dimensional heat transfer model for the thermal model of the touchdown bearings. Fig. 6 shows a schematic of the equivalent electrical circuit of the thermal model.

The thermal resistances are summarized in Table 1. Where  $d_b$ ,  $d_h$ ,  $d_i$ ,  $d_o$ ,  $d_s$ ,  $d_o$ ,  $L_h$  and  $W$  are the dimensions of the bearing that can be found from the bearing catalog and the drawings of the case study.  $H_i$ ,  $H_o$  and  $H_r$  represent the heat generation in the inner ring, outer ring and in the contact of rotor and touchdown bearing, respectively and that will be described in section 3.5.

The following equation represents the coefficient of free convection heat transfer from the bearing housing (Harris, 2001):

$$h_h = 23(T - T_\infty)^{0.25} \tag{16}$$

where  $T$  is temperature and  $T_\infty$  is the ambient temperature.

The heat transfer balance should be satisfied in each node of the model (Zhao et al., 2016).

$$H_{in} - H_{out} = \rho CV \frac{dT}{dt} \tag{17}$$

Table 1  
Thermal resistance of bearing elements (Zhao et al., 2016).

Shaft/Inner race	Ball/ambient	Outer race	Housing
$R_1$ convection	$R_5$ conduction	$R_7$ conduction	$R_8$ conduction
$R_2$ conduction	$R_6$ convection		$R_9$ convection
$R_3$ conduction			
$R_4$ conduction			

where  $H_{in}$  and  $H_{out}$  are input and outflow power loss, respectively.  $C$  is the specific heat,  $\rho$  is the density and  $V$  is the volume. The temperature gradient is denoted as  $dT/dt$ . In a discrete form, the thermal balance in the bearing can be rewritten as (Jin et al., 2015).

$$\mathbf{M}_{brg} \mathbf{C}_{brg} (\mathbf{T}^{t+\Delta t} - \mathbf{T}^t) = (\mathbf{H}_{in}^t - \mathbf{H}_{out}^t) \Delta t \tag{18}$$

where  $\mathbf{M}_{brg}$  is lumped mass matrix and  $\mathbf{C}_{brg}$  is a matrix form of the specific heat for the bearing model. The input heat flux and output heat flux are denoted as  $\mathbf{H}_{in}^t$  and  $\mathbf{H}_{out}^t$ , correspondingly. The temperature in new time step ( $\mathbf{T}^{t+\Delta t}$ ) can be obtained by the temperature in the previous time step ( $\mathbf{T}^t$ ).

3.5. Calculation of power loss in dropdown

As mentioned earlier, the friction between the rotor and the inner race besides the friction inside bearing are considered as heat sources.

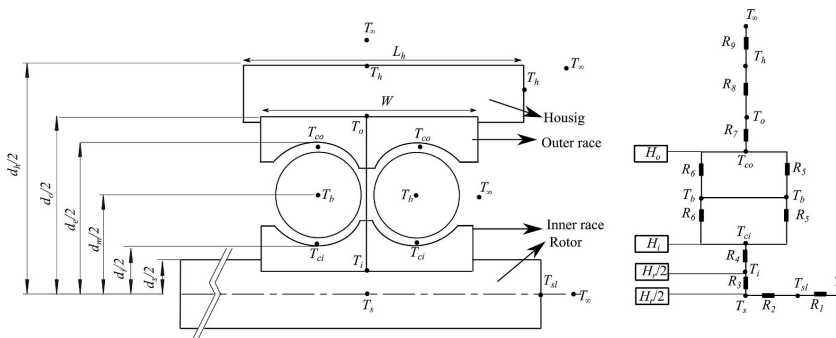


Fig. 6. Equivalent electrical circuit model of the bearing.

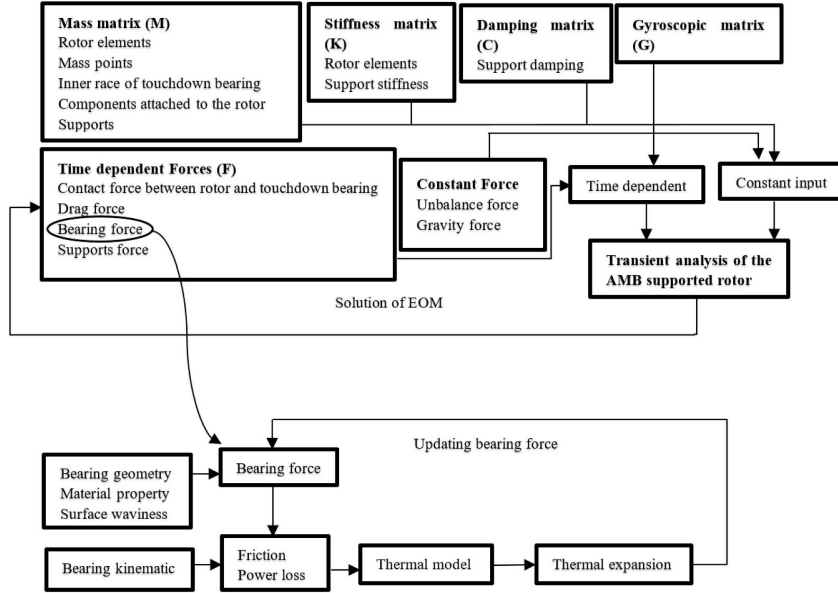


Fig. 7. Flowchart of updating bearing load in the AMB supported rotor.

The power loss resulting from the contact between the rotor and inner race can be expressed as follows (Jin et al., 2015):

$$H_f = F_{fr} V_{rel} \quad (19)$$

where  $V_{rel}$  is the relative velocity between rotor and inner race and  $F_{fr}$  is the friction force between the rotor and touchdown bearing. The second part of the power loss is due to friction between the balls and the races. The equation that expresses the global friction in the bearing ( $M$ ) is as follows (Harris, 2001):

$$M = M_L + M_s \quad (20)$$

The load-dependent term is given by (Palmgren, 1959):

$$M_L = f_1 P d_m \quad (21)$$

where  $P$  is the equivalent load of the ball bearing. The velocity-dependent term can be calculated by (Palmgren, 1959):

$$\begin{cases} M_v = 10^{-7} f_2 (\nu N)^{2/3} d_m^3 & \nu N > 2000 \\ M_v = 160 \times 10^{-7} f_2 d_m^3 & \nu N \leq 2000 \end{cases} \quad (22)$$

where,  $f_1$  and  $f_2$  are factors dependent on the design of the bearing and the load on the bearing,  $\nu$  is kinematic viscosity (centistoke) and  $N$  is speed of inner race (rpm) and  $d_m$  presents the pitch diameter (mm). In high-speed application, the spinning torque, as a consequence of the spinning movement of the individual balls around its own axis, cannot be neglected. The spinning torque in the inner ring can be expressed as follows (Poritsky et al., 1947):

$$M_{si} = \frac{3\mu F_j a \bar{\zeta}}{g} \quad (23)$$

where  $\mu$  is the friction coefficient,  $F_j$  is contact force given in equation (6). The parameter  $\bar{\zeta}$  is the elliptical integral of second type. The equation that describes the total heat generation at the inner race is as follows (Zhao et al., 2016):

$$H_i = \sum_j H_{ij} = \sum_j (\omega_b M_{ij} + \omega_{si} M_{si}) \quad (24)$$

where,  $M_{ij}$  is the friction torque in the inner race and  $M_{si}$  is spinning drag torque. A similar approach can be applied to obtain the total heat generation at the outer race.

### 3.6. Bearing deformation under thermal effect

As a result of variation in the temperature, the dimension of the bearing components can be changed. The thermal expansion of ball and inner race are expressed as (Sun, 2006b):

$$\epsilon_b = \alpha_b \nu_b T_b \quad (25)$$

$$\epsilon_{in} = \frac{\alpha_i (1 + \nu_i) r_s}{3 r_i + r_s} [\Delta T_i (2r_s + r_i) + \Delta T_{ci} (2r_i + r_s)] \quad (26)$$

The radius of the ball, inner race and cross section of rotor in the location of the touchdown bearing are denoted as  $r_b$ ,  $r_i$  and  $r_s$ , respectively. The thermal expansion coefficient of the ball and inner race are expressed as  $\alpha_b$  and  $\alpha_i$ , respectively.  $\nu_i$  is the Poisson's ratio of the inner ring. The temperature of the ball is denoted as  $T_b$ , and  $\Delta T_i$  is the difference between the temperature of the inner ring and ambient temperature. Likewise,  $\Delta T_{ci}$  shows the corresponding value for the contact area of the ball/inner ring.

Calculation of the radial thermal expansion of the outer race is as follows (Sun, 2006b):

$$\epsilon_{out} = \frac{\alpha_o (1 + \nu_{out}) r_{out}}{3 r_{out} + r_h} [\Delta T_{out} (2r_{out} + r_h) + \Delta T_h (2r_h + r_{out})] \quad (27)$$

In the above equation,  $r_{out}$  and  $r_h$  refer to the radius of the outer race and housing, respectively.  $\alpha_o$  is the thermal expansion coefficient of the outer race and  $\nu_{out}$  is the Poisson's ratio of the outer race. The difference between the temperature of the outer race and housing with the ambient temperature are denoted as  $\Delta T_{out}$  and  $\Delta T_h$ , correspondingly.

The following equation gives the total radial interface in the bearing (Zhao et al., 2016):

$$\varepsilon_t = \varepsilon_b + \frac{(\varepsilon_{in} - \varepsilon_{out})}{2} \cos \varphi \quad (28)$$

The data from the thermal expansion of the bearing are required to obtain the thermal preload of the bearing which will be described in the following section.

### 3.7. Updating the model

The material of the bearing and the geometry will be designated in a way that there should be a balance between the heat generation inside the bearing and the heat dissipated from the bearing. If the heat dissipation is less than the heat generated inside the bearing, the temperature in the bearing will rise and it can promote the possibility of thermal failure. Therefore, it is essential to update the thermal effect in the model and include the effect of thermal expansion in equations (2)–(5) and (8). The flow chart of the simulation is presented in Fig. 7.

## 4. Case studies and results

The parameters required to analyze the case study of a rotor are shown in Table 2. The main dimensions of the rotor are depicted in Fig. 8-a. The touchdown bearings 1 is a hybrid deep groove ball bearing of the type 6014 HC5/C3 and touchdown bearing 2 is a pair of angular contact ball bearings of the type 71914-E-T-PS4 installed in an X-configuration, the technical data of bearing are shown in Table 3. Material properties of the bearing is presented in Table 4. Fig. 8-b shows the FEM model of the rotor main shaft and the location of the touchdown bearings. The rotor FE model includes 31 rotor nodes. The bearing coordinate system shown in Fig. 2 differs from rotor coordinate system that is considered by using a transfer matrix for bearing forces. In the FE model, the touchdown bearings are located at nodes 2 and 28. The connection gear (node 1), axial AMB (node 5), axial AMB nut (node 3), nuts for radial AMB rotor stacks (nodes 7, 25), radial AMB rotor stacks (nodes 10, 22) are modeled as mass points. A conservative modeling approach was used and only the main shaft is modeled as beam

**Table 2**  
The main data for the simulation of the rotor dropdown.

Parameter	value
Initial rotation speed of the rotor	15200 rpm
Modulus of elasticity of steel part of rotor	$2.0 \cdot 10^{11}$ Pa
Material density of steel part of rotor	$7850 \text{ kg/m}^3$
Poisson's ratio of steel part of rotor	0.3
Modulus of elasticity of radial AMB lamination of rotor	$1.85 \cdot 10^{11}$ Pa
Material density of radial AMB lamination of rotor	$7600 \text{ kg/m}^3$
Poisson's ratio of radial AMB lamination of rotor	0.285
Mass of rotor	109.7 kg
Effective mass of support, NDE	50 kg
Support stiffness of NDE ( $K_y, K_z$ )	$(1.5, 1.1) \cdot 10^9 \text{ N/m}$
Effective mass of support, DE	85 kg
Support stiffness of DE ( $K_y, K_z$ )	$(2.7, 1.5) \cdot 10^9 \text{ N/m}$
Support damping of NDE ( $C_y, C_z$ )	$(2.82) \cdot 10^3 \text{ N/m}$
Support damping of DE ( $C_y, C_z$ )	$(3.68) \cdot 10^3 \text{ N/m}$
Contact stiffness between rotor and inner race (bearing 1)-TB1	$1.144 \cdot 10^9 \text{ N/m}^{1.11}$
Contact stiffness between rotor and inner race (bearing 2)-TB2	$1.73 \cdot 10^9 \text{ N/m}^{1.11}$
Radial Air gap between rotor and touchdown bearings	250 $\mu\text{m}$
Polar moment of inertia of rotor	$0.39 \text{ kgm}^2$
Diameter moment of inertia of rotor	$4.5535 \text{ kgm}^2$
Unbalance mass at AMB disk	$1.07 \cdot 10^{-6} \text{ kg m @ } 180^\circ$
Unbalance mass at the center of the rotor active part	$2.78 \cdot 10^{-6} \text{ kg m @ } 180^\circ$
Static contact friction coefficient between rotor and inner race	0.05
Dynamic contact friction coefficient between rotor and inner race	0.1

elements whereas all the surface elements are included as mass elements neglecting the stiffness of the components contributing to the total rotor stiffness. The copper end-rings in the rotor are also considered as mass points at nodes 13 and 19. The detail figure for the mechanical interaction of the rotor and touchdown bearing is shown in Fig. 3.

The FEM model of the rotor is validated using experimental modal analysis by obtaining the bending frequencies of the rotor. The lowest bending mode frequency of the rotor was 673.5 Hz (Heikkinen et al., 2015). The FE model of the rotor is created in self-made MATLAB rotordynamics toolbox. The transient analysis was performed using a ready-made ode45 integrator that is based on 4<sup>th</sup> order Runge-Kutta integration method. The simulation time was 0.3 s using a time step of 1e-5 s, the maximum integration step was 5e-6 s and the maximum allowable integration error 1e-5.

The support stiffness was obtained by FEM analysis and the damping was estimated using FE modal analysis and damping ratio of 1% that is typical for steel structures. The effective mass for the support stiffness was obtained using FE modal analysis and 3D model of the structure by obtaining the moving part of the structure at first mode and defining the corresponding inertia properties from 3D model. The unbalance masses are obtained from balancing results of a low speed balancing of the prototype machine and balancing planes are used for unbalance locations. The value used for the static and dynamic contact friction is selected from the literature (Jin et al., 2015).

### 4.1. Orbital motion of rotor

The orbital motions of the rotor for three different dynamic friction coefficients between the rotor and touchdown bearings are shown in Fig. 9. It can be seen in Fig. 9(a–c) that after the initial impact of the rotor with touchdown bearings, the rotor bounces back up to the height more than half of the air gap. The simulation result revealed that the friction has a visible influence on the orbital motion. As can be seen in Fig. 9-a, with the low value of the friction coefficient as 0.05, after the second contact of the rotor and touchdown bearing number 2 (TB2), the rotor bounces up to approximately  $-150 \mu\text{m}$ . As the friction between the rotor and touchdown bearing increases to 0.1 and 0.15, the rotor impacts the touchdown bearing at a point where the arc length is wider and the rotor gradually settles toward the right and the magnitude of the bounce height decreases (Fig. 9-b,c).

In the FE-model of the rotor, the x-axis is defined along the longitudinal axis of the rotor (Fig. 8). This work focuses on studying the deformations and contact forces in the bearing plane (y- and z-directions) and the axial deformations are not considered. Fig. 10 shows the displacements in y- and z-directions of the rotor at the locations of touchdown bearings during a touchdown event using the friction coefficient listed in Table 2. The first hit of the rotor on the touchdown bearings deforms both bearings and support, resulting in higher displacement than  $250 \mu\text{m}$  that is the air gap length of the touchdown bearings. After the first hit, the rotor lifts off from the inner ring and during the subsequent contacts the displacement in the vertical direction is reduced (Fig. 10a) and gradually the rotor will stabilize on the bottom of the bearing inner ring having a total displacement slightly higher than the air gap length. The contacts of the rotor with the touchdown bearings can be also seen from the z-displacement (Fig. 10b). In this direction, the displacement is not exceeding or even approaching very close to the air gap length. The results curve indicates a smooth swinging motion on the bottom of the bearing inner ring, decreasing gradually in the direction of the gravity (0 displacement in the z-direction).

Fig. 11 shows angular velocities of the inner rings in both bearings. As can be seen, the inner rings of the touchdown bearings accelerate with different rates. That is mainly due to the different bearing types having different inertia properties. The touchdown bearing 1 is a deep groove ball bearing that accelerates faster. After 0.2 s, the tangential

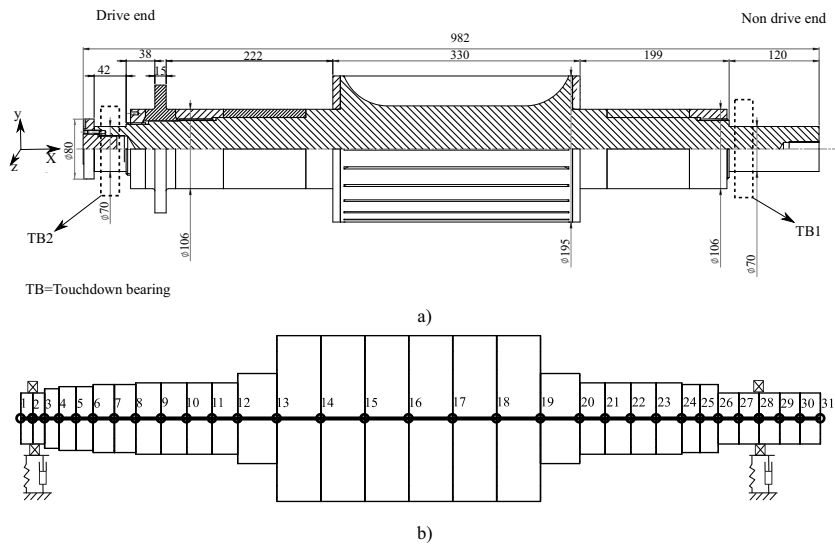


Fig. 8. The main dimensions and FEM model of the electric motor rotor/touchdown bearing. a) Dimension, b). FEM model of rotor.

Table 3  
Bearing data, bearing type 71914-E-T-PS4.

Bearing parameter	Value
Bore diameter	70 mm
Outside diameter of inner race	78 mm
Inside diameter of outer race	100 mm
Outside diameter of outer race	110 mm
Pitch diameter	85 mm
Bearing width (for one row)	16 mm
Housing axial width (for one row)	25 mm
Housing diameter	120 mm
Nominal contact angle	25degree
Number of balls	23

Table 4  
Material properties of bearing.

Thermal properties	Ceramic ball	Steel
Thermal conductivity of race (W/mK)	35	70
Linear expansion coefficient	$3.2 \cdot 10^{-6}$	$11.8 \cdot 10^{-6}$
Poisson's ratio	0.3	0.26
Density	3200	7800
Modulus of elasticity	$3.15 \cdot 10^{11}$ Pa	$2.0 \cdot 10^{11}$ Pa
Specific heat capacity (J/kgK)	673	510
Kinematic viscosity of air ( $m^2/s$ )	$1.5 \cdot 10^{-5}$	

velocity of the bearing inner ring equals the tangential velocity of the rotor outer surface. As the pair of angular contact bearing has a higher mass and moment of inertia, the acceleration of the second bearing is lower.

4.2. Effect of surface waviness

In order to evaluate the influence of the surface waviness on the friction heat generated in the touchdown bearings, the contact forces and the friction heat generation in the bearing has been evaluated for six different configurations that are introduced in Table 5. The first case

presumes that the bearing has an ideal surface. In cases 2–4, the inner race has a surface waviness with the amplitude of 1 μm and the 1<sup>st</sup>, 2<sup>nd</sup> and 3<sup>rd</sup> orders of waviness are studied. The last two cases are used to evaluate the influence of a higher amplitude of surface waviness.

4.2.1. Contact force

Fig. 12 shows the contact force between the rotor and the bearing inner ring as functions of time. The waviness orders of the first to third orders (namely eccentricity, ellipticity and triangularity) are studied and compared with the bearing having the ideal geometry. In the simulation, the contact forces between individual balls and bearing races have been investigated. Then, the magnitudes of bearing force depicted in Fig. 13 are obtained based on the model presented in (Sopanen and Mikkola, 2003). The first hit of the rotor on the bearings results in high contact forces exceeding 5000 N. After the first two hits, the rotor experiences lower bounces thus shorter time periods where rotor and inner ring are not in contact. Fig. 12-b shows a close zoom of the figure for the time span of 0.025–0.1 s. The figure shows that with the surface waviness of amplitude 1 μm, the contact occurs in the time close to the bearing with the ideal surface and it does not cause noticeable change in the contact time of the rotor and touchdown bearing. Eventually, the rotor is in continuous contact with the bearing inner ring and the contact force between the rotor and the inner ring gradually settles around 500 N. The difference of the bearing waviness can be seen actually at the time when the rotor is in continuous contact with the bearing. The waviness components affect the variation of the forces when the rotor is swinging smoothly on the bottom of the touchdown bearing. In the ideal case, the contact force between the rotor and inner ring settles at the level of 500 N soon after the first hits. In other cases where any order of bearing waviness is included, the contact force varies below or above the magnitude of the contact force in the ideal bearing. The magnitude of the variation can be as high as double the stabilized level of the contact force in the ideal case. The highest variation in contact forces between the rotor and the inner ring are in the case of triangular waviness where the contact force varies between 150 and 1000 N when the rotor is swinging on the bearings. Contradictorily, the contact forces in the bearing are evenly smooth in the case of

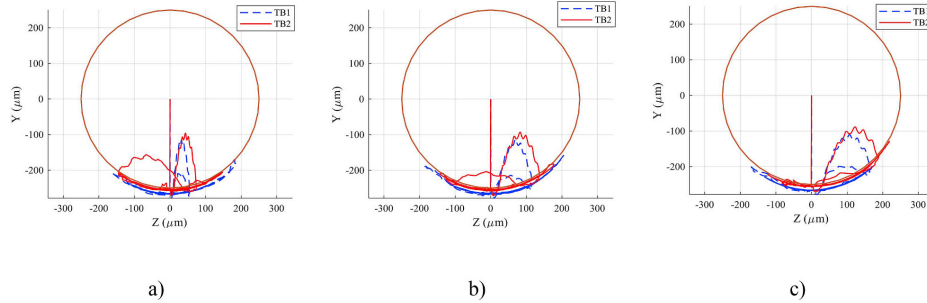


Fig. 9. The orbital motion of a rotor for different values of dynamic friction coefficient between rotor and inner race: a) 0.05 b) 0.1 c) 0.15.

triangular bearings and in ideal bearings (Fig. 13). In cases of first and second order waviness, the contact forces in the bearing vary notably. A reason for such behavior is most likely geometrical. The triangularity of the bearing has a 120-degree phase difference between wave peaks that results in forces that are counteracting with respect to each other. In the case of a 180-degree phase difference in the waves, there are no such counteracting forces and the highest force component follows the wave peak traveling in the lower half of the bearing ring.

4.2.2. Friction heat generation

Fig. 14a shows the friction torque in the touchdown bearing in the case of the ideal bearing surface. In this case study, the load-dependent friction torque is less than the velocity-dependent friction torque. In the first contact, the load-dependent friction has the highest value of about 0.14 Nm. After the second contact, it is reduced and gradually approaches a uniform level. The velocity-dependent term is highly affected by the angular velocity of the inner race and by increasing the angular velocity, the level of viscous friction torque rises. In the high-speed application, the velocity-dependent viscous friction term is the most determinative term in the calculation of global friction torque (equation (20)). It is required to mention that applying the empirical equation for the velocity dependent friction determined by Palmgren (1959), equation (22), can raise some uncertainties in the calculation of the velocity dependent term in oil free touchdown bearing. Above equation is valid for the case where the bearing operates at moderate speed and does not carry excessive load and can be used for the oil with the specific gravity of 0.9. Therefore, it is necessary to investigate the

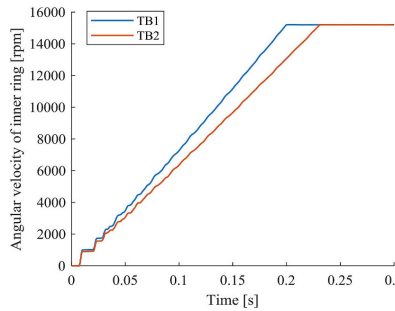


Fig. 11. Angular velocity of rotor and inner race during dropdown.

influence of the velocity dependent term in the calculation of the power loss in the bearing. Later on, in section 4.2.3 it will be shown that the internal heat generation in the inner ring and outer ring is relatively low compared to the friction heat due to the contact of rotor and inner ring. Therefore, applying the equation for the calculation velocity dependent term by Palmgren still can provide reasonable result for the dropdown of the rotor in oil free touchdown bearing. The velocity of the bearing inner ring increases constantly when the rotor is in contact resulting in a smooth friction torque curve. Fig. 14b shows that for surface waviness with the amplitude of 1  $\mu\text{m}$ , the global friction torque

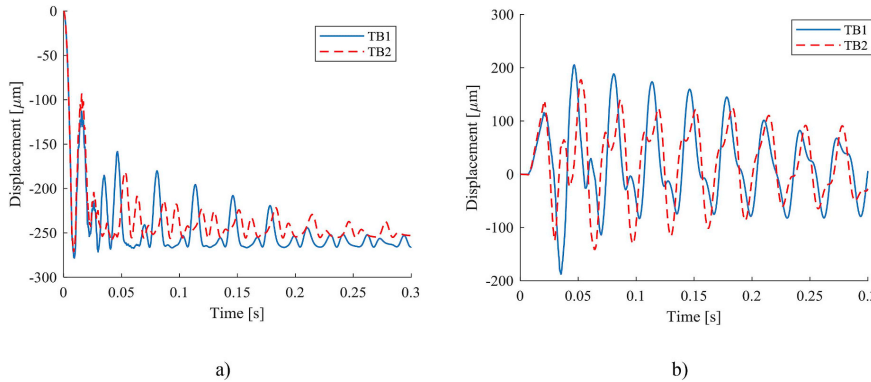
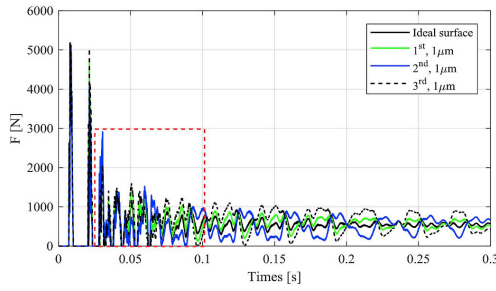


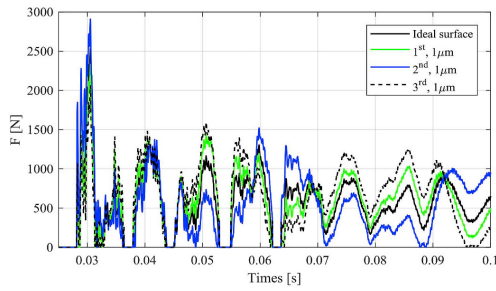
Fig. 10. The displacement of rotor at touchdown bearing location: a) y-direction b) z-direction.

**Table 5**  
Various cases of waviness in bearing.

Different cases of surface waviness in bearing, waviness order (Amplitude)						
	Ideal	1 <sup>st</sup> (1 μm)	2 <sup>nd</sup> (1 μm)	3 <sup>rd</sup> (1 μm)	2 <sup>nd</sup> (4 μm)	3 <sup>rd</sup> (2 μm)
Ideal surface of bearing	✓	-	-	-	-	-
Waviness in both races	-	✓	✓	✓	✓	✓
Waviness in contact of rotor inner race	-	✓	✓	✓	✓	✓



a)



b)

**Fig. 12.** Magnitude of the contact force between the rotor and inner race for the bearing with the ideal surface and a bearing with waviness. a) simulation time 0.3 s, b) zoomed view from 0.025 to 0.1 s.

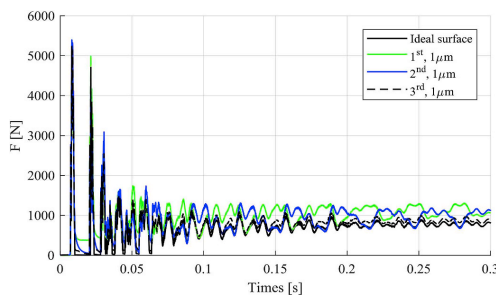


**Fig. 13.** The magnitude of the bearing force for the bearing with an ideal surface and bearing with waviness.

has a small variation irrespective of the waviness order, and the effect is negligible.

The effect of the spinning velocity on the calculation of the total heat generation in the bearing race (equation (24)) should be taken into account. The spinning torque of the ball which undergoes the highest contact stress is shown in Fig. 15. The spinning torque in the rotor drop is not uniform and in the first hit, the contact force between the ball and bearing race is high and in the following contacts, the spinning torque is reduced.

**4.2.3. Heat generation**

Fig. 16 shows the heat generation in the bearing during a 0.3 s time span from the rotor drop. The figure shows that from the start of the dropdown until 0.2 s, the heat generation increases in both races; afterward it is stabilized around the constant value. In the case of the bearing with the ideal surface, the maximum heat generation in the contact of the outer race is 60 W; that is approximately 10 W higher than the maximum heat generation in the inner race. This figure reveals the heat generation in the bearing races has a similar trend to the acceleration of the bearing race (Fig. 11). In addition, for the surface waviness with the amplitude of 1 μm, regardless of the waviness order, the heat generation in the bearing is higher than the bearing with the ideal surface. In the case of first order waviness, the maximum heat generation in the bearing races is about 10% higher than the corresponding values for the bearing with the ideal surface. In the same amplitude of surface waviness, for the higher order of waviness (2<sup>nd</sup>, 3<sup>rd</sup>), the difference in the heat generation of the bearing with surface waviness and the ideal surface are reduced to approximately 7% and 5%, respectively. Furthermore, at the start of dropdown the difference between the heat generation in the bearing with surface waviness and the bearing with the ideal surface is low and as the rotor starts to rub against the touchdown bearing, the difference will be higher; after 0.2 s the difference in the heat generation of the bearing with surface waviness and ideal case reaches to the maximum value.

As demonstrated in (Zhao et al., 2016), the global friction torque in the bearing is divided into the friction torque in the inner ring and outer ring. Due to the smaller radius of the inner race rather than the outer race radius, the friction torque in the inner race (The term  $M_{ij}$  in equation (24)) is less than the friction torque in the outer race. Therefore, the inner race experiences less heat generation compared to the outer ring. As mentioned earlier, the heat generation in the bearing races is dependent on the friction torque and the angular velocity of the bearing component. Just after the dropdown, the touchdown bearing experiences a high contact force and at this time the angular velocity of the inner ring is still low. For this reason, in the first few milliseconds of the simulation, the main part of the global friction torque is due to the load-dependent friction torque. When the inner ring accelerates because of the high angular velocity of the inner ring, the friction drag torque increases. In addition, the friction drag torque is expressed in terms of the angular velocity of the inner ring. For this reason, the heat generation in the bearing follows the same trend as the acceleration of the inner ring. Moreover, when the surface waviness exists in the bearing, the overall magnitude of the contact force in the bearing is higher compared to the bearing with the ideal surface. After the inner ring rotates at the same speed as the rotor, a clear fluctuation in the magnitude of the heat generated in the bearing is observed. This can be

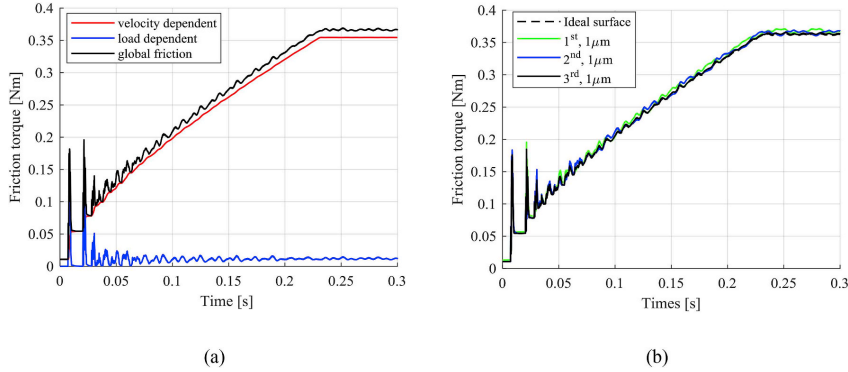


Fig. 14. Friction torque in bearing a) ideal surface b) global friction torque for ideal surface and the bearing with 1–3 order waviness with the amplitude of 1 μm.

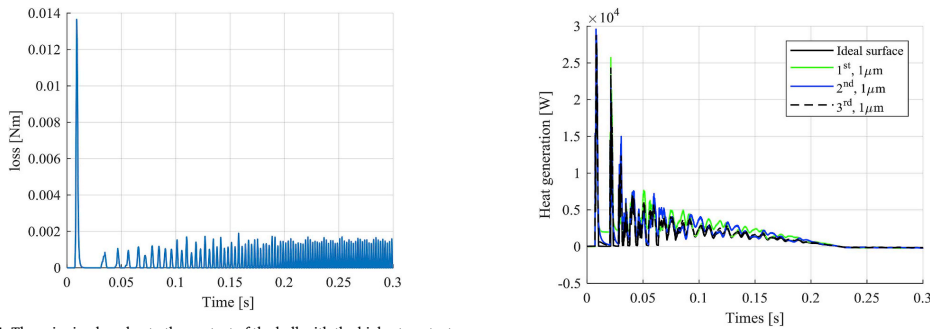


Fig. 15. The spinning loss due to the contact of the ball with the highest contact stress and the bearing race (Case I - Table 5).

Fig. 17. Friction heat generation in the contact of rotor and touchdown bearing.

attributed to the nature of the sinusoidal function used for the numerical simulation of the waviness.

Fig. 17 depicts the frictional heat generation that is created during the contact between the rotor and the touchdown bearings. The figure shows that a few milliseconds after the dropdown, the heat generation in the bearing with the ideal surface rises to the maximum value of

$2.8 \cdot 10^4$  W. Then it is reduced and for a couple of milliseconds becomes zero. Then, the second peak in the heat generation is observed. Afterward, the reduction in the heat generation is followed by a fluctuation until 0.2 s. Then, the heat generation becomes zero. The overall pattern shows that waviness imperfection results in greater amount of heat

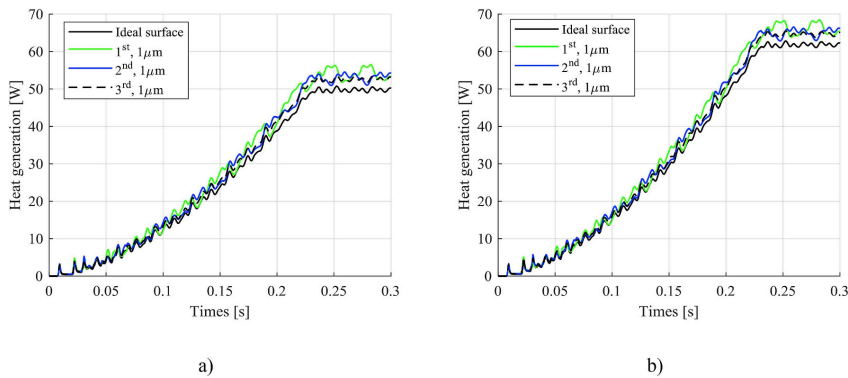


Fig. 16. Internal heat generation in the touchdown bearing a) inner ring b) outer ring.

generation between the rotor and inner ring rather than the bearing with the ideal surface.

When the magnetic field fails, a few milliseconds will pass before the rotor drops and contacts the touchdown bearing. At this time, the rotor does not have contact with the inner ring and therefore in the start of the dropdown, the heat generation between the rotor and inner ring is zero. Due to the high magnitude of the contact force between the rotor and inner race, and also the high magnitude of the relative angular velocity of the rotor and inner race, the heat generation in the first contact of the rotor and inner race were found to be considerably greater than internal heat generated in the bearing. When the rotor bounces for a second time, there is no physical contact between the rotor and touchdown bearing. Therefore, the heat generation again becomes zero. As the inner ring accelerated with the same speed as the rotor (after 0.2 s), the relative velocity between the rotor and inner ring becomes zero. Therefore, the heat generation is equal to zero.

The surface waviness in the bearing results in greater penetration of the rotor in the inner ring. Consequently, the contact force increases and the bearing has to endure higher heat generation. Even though the magnitudes of the peak values are very high, the time periods for the highest peaks are just some milliseconds, resulting in a moderate rise in temperatures, as will be shown in the next section.

#### 4.3. Thermal analysis

First, the thermal analysis of the bearing has been studied for the case where the bearing has an ideal surface. Fig. 18 shows the temperature rise for different nodes of the model introduced in Fig. 6 during the 0.3 s time span after the dropdown. This figure shows that in the dropdown, the temperature of bearing races, ball, the contact area of the ball and bearing races, housing as well as the rotor, is increased. Nevertheless, the thermal expansion of different components of the bearing and rotor are dissimilar. For the few milliseconds after the dropdown, the temperature of the inner ring is the same as ambient temperature; then the sudden increase in the temperature is observed. Afterward, for the second time, the temperature of the inner ring remains constant and instantaneously rises. This behavior continues until gradually the temperature reaches the maximum value of 296.2 K at 0.2 s. Then, the temperature stabilizes. A similar pattern has been observed for the temperature of the shaft. However, the maximum temperature of the shaft is approximately six times less than the maximum temperature of the inner ring. In the contact point of the ball and bearing race, the temperature increases rapidly to just slightly above the maximum temperature of the inner ring and then remains almost constant. During the simulation time of 0.3 s, the temperature of the ball and outer race increases to 294.5 and 293.2 K, respectively. The bearing

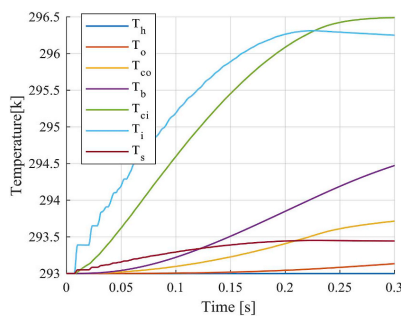


Fig. 18. Temperature rise in the rotor ( $T_h$ ), inner ring ( $T_i$ ), outer ring ( $T_o$ ), ball ( $T_b$ ), housing ( $T_h$ ), contact of the ball and bearing races ( $T_{ci}, T_{co}$ ).

housing does not experience a significant rise in temperature and remains close to 293 K.

It should be noted that the temperature rise in the bearing is not a linear phenomenon. The rotor drop speed, geometry and material property of the rotor and bearing, the air gap clearance, as well as the friction in the bearing, can influence the temperature of the rotor and touchdown bearing. In the beginning of the dropdown, the rotor moves downwards; at this time the rotor is not in contact with the touchdown bearing. For this reason, during the first few milliseconds, the temperature of the inner ring is the same as the ambient temperature. After the initial contact, there is a considerable friction heat generation between the rotor and inner ring which can explain the instantaneous increase in the temperature of the inner race. After the first contact of the rotor and inner ring, the rotor bounces back; at this time the temperature remains constant until the rotor contacts the bearing for a second time. This behavior lasts until the rotor continually whirls in the bearings. The temperature of the inner ring increases in relation to the acceleration of the bearing race. When the inner ring accelerates, the temperature of the inner ring increases and when it rotates with the same angular velocity as the rotor (from 0.2 s to end of simulation), the heat generation remains constant and the temperature of the inner ring stabilizes. The high friction between the bearing and rotor, and also the friction inside bearing, makes the temperature in the contact region of the ball and bearing race and ball be high. In addition, it is clear from Fig. 6 that in the thermal model of the bearing, the lumped mass of the shaft is significantly greater than the lumped mass of bearing components. Therefore, the temperature of the rotor increased at a lower rate rather than the bearing. Inside the bearing housing, the heat transfers via conduction and the natural convection occurs between the outer face of the housing and environment. Therefore, the temperature rise is lower than in other parts and there is not a significant difference in the temperature rise.

The results can be partially validated based on the existing literature on the rotor dropdown. The trend in the temperature increase of the inner race is found to be similar to Jin et al. (2015) and Zhao et al. (2016). In the start of dropdown, a sharp increase in the temperature of the inner ring has been observed. Then, the temperature increase until a maximum level is reached. In their study, the maximum temperature rise of the inner ring was approximately 6 K, which is in line with results of this study. In the simulation it is shown that high contact force between rotor and inner ring occurs for a very short moment (mainly in first contact) and a similar finding was reported by Zhao (Zhao et al., 2016).

Fig. 19a presents the temperature rise of the inner race for the different amplitude of surface waviness. In the circumstance where the bearing suffers from surface waviness regardless of either the amplitude of waviness or the waviness order, the temperature of the inner ring is higher than the temperature of the bearing with the ideal surface. For the surface waviness with the amplitude of 1  $\mu\text{m}$ , the first order waviness results in a higher temperature rise rather than the higher order of waviness. In order to observe the influence of the higher amplitude of surface waviness in the temperature rise of the bearing, the last two cases, 2  $\mu\text{m}$  (3<sup>rd</sup>) and 4  $\mu\text{m}$  (2<sup>nd</sup>), has been also studied. The highest studied amplitude for the surface waviness is 4  $\mu\text{m}$ , which is within the range of the surface waviness of bearings with best bearing manufacturing conditions reported in (Mohanty, 2015). The higher amplitude of surface waviness (2  $\mu\text{m}$ , 3<sup>rd</sup>) leads to more temperature rise in the inner ring. For the bearing with the ideal surface, the temperature rise is 3.5 K, whereas for the last case (4  $\mu\text{m}$ , 2<sup>nd</sup>) the temperature of the inner race has an 8 K increase. A similar pattern has been found for the temperature rise of the contact area of the ball and the inner ring (Fig. 19b). The previous section showed that in the case of surface waviness with the amplitude of 1  $\mu\text{m}$ , the waviness orders 1–3 causes a minor change in friction heat generation. Consequently, the temperature of the inner ring experiences a small increase (approximately 1 K) when compared to the bearing with the ideal surface. With the higher

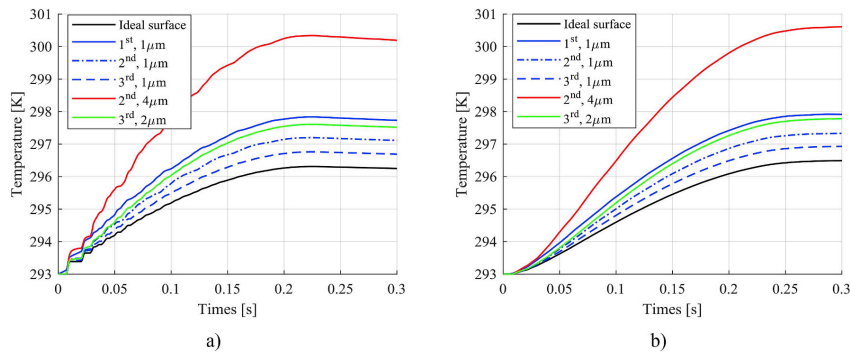


Fig. 19. Temperature rise of the inner ring and the contact area of ball/inner ring for both ideal surface and the various order and magnitude of surface waviness; a) inner ring b) contact point of ball inner ring.

amplitude of the waviness, there are noticeable increases in the contact force and power loss in the bearing. For this reason, the temperature of the inner ring rises noticeably higher than the bearing with the ideal surface. In addition, when both races have waviness, the contact force and the power loss is higher than the case where only one race has waviness.

## 5. Conclusion

In this study, the dynamic and thermal model of touchdown bearings in a rotor drop were presented. In the simulation, the FE-model of the flexible rotor was integrated with the dynamic model of the touchdown bearing. The contact forces between the rotor and safety bearing, as well as internal contact force in the touchdown bearing, were calculated by Hertzian contact theory. The friction heat generated due to impact, whirling of the rotor on the touchdown bearing, and the internal friction torque in the bearing were obtained. The one-dimensional equivalent electrical circuit model is applied to the thermal model of the touchdown bearing. The orbital motion of the rotor showed that the higher dynamic friction coefficient between the rotor and touchdown bearing increases the arc of the contact region which the rotor settles in the bearing. The results showed that the temperature rise in the bearing is influenced by the variation of the angular velocity of the rotor and inner ring, viscosity of lubrication and the friction between the rotor and touchdown bearing, as well as the friction inside the bearing. Moreover, differences in surface waviness in the bearing have been studied. It has been found that for a small amplitude of surface waviness, the various orders of surface waviness result in small changes in the contact force and heat generation in the bearing. The results indicated that the amplitude of the waviness has a greater effect on increasing the power loss and contact forces between balls, and also the contact of the rotor and inner race. Meanwhile, for the constant amplitude of the waviness, the higher waviness order does not lead to a considerable change in the results.

## Acknowledgment

The authors would like to thank Academy of Finland for funding under the ViDROM project (grant number 277502).

## References

Ai, S., Wang, W., Wang, Y., Zhao, Z., 2015. Temperature rise of double-row tapered roller bearings analyzed with the thermal network method. *Tribol. Int.* 87, 11–22.  
 Burton, R.A., Staph, H.E., 1967. Thermally activated seizure of angular contact bearings. *Tribol. Trans.* 10, 408–417.

Changqing, B., Qingyu, X., 2006. Dynamic model of ball bearings with internal clearance and waviness. *J. Sound Vib.* 294, 23–48.  
 Childs, D.W., 1979. Rub induced parametric excitation in rotors. *J. Mech. Des.* 101, 640–644.  
 Choy, F.K., Padovan, J., 1987. Non-linear transient analysis of rotor-casing rub events. *J. Sound Vib.* 113, 529–545.  
 Ecker, H., 1998. Nonlinear stability analysis of a single mass rotor contacting a rigid backup bearing. *Proc. Euromech. Colloquium 15–18, 79–88* Loughborough, UK.  
 Eschmann, H.W., 1985. *Ball and Roller Bearings: Theory, Design and Application*, second ed. Wiley.  
 Halminen, O., Aceituno, J.F., Escalona, J.L., Sopanen, J., Mikkola, A., 2017a. A touchdown bearing with surface waviness: a dynamic model using a multibody approach. *Proc. Inst. Mech. Eng. - Part K J. Multi-body Dyn.* 231, 658–669.  
 Halminen, O., Aceituno, J.F., Escalona, J.L., Sopanen, J., Mikkola, A., 2017b. A touchdown bearing with surface waviness: friction loss analysis. *Mech. Mach. Theor.* 110, 73–84.  
 Hamrock, B.J., Dowson, D., 1981. *Ball Bearing Mechanics*. NASA Technical Memorandum 81691.  
 Harris, T.A., 2001. *Rolling Bearing Analysis*, fourth ed. John Wiley & sons, New York.  
 Harsha, S.P., Kankar, P.K., 2004. Stability analysis of a rotor bearing system due to surface waviness and number of balls. *Int. J. Mech. Sci.* 46, 1057–1081.  
 Heikkinen, J., Smirnov, A., Hakonen, V., Sopanen, J., 2015. Virtual Testing of AMB Supported Rotor-system. pp. 465–471.  
 Heikkinen, J.E., Ghahramani, B., Viitala, R., Sopanen, J., Juhanko, J., Mikkola, A., Kuosmanen, P., 2018. Vibration analysis of paper machine's asymmetric tube roll supported by spherical roller bearings. *Mech. Syst. Signal Process.* 104, 688–704.  
 Hunt, K., Crossley, F., 1975. Coefficient of restitution interpreted as damping in vibroimpact. *ASME J. Appl. Mech.* 42 (2), 440–445.  
 Jin, C., Wu, B., Hu, Y., 2012. Heat generation modeling of ball bearing based on internal load distribution. *Tribol. Int.* 45, 8–15.  
 Jin, C., Zhu, Y., Xu, L., Xu, Y., Zheng, Y., 2015. The thermodynamic properties of a new type catcher bearing used in active magnetic bearings system. *Appl. Therm. Eng.* 82, 253–263.  
 Kärkkäinen, A., Sopanen, J., Mikkola, A., 2007. Dynamic simulation of a flexible rotor during drop on retainer bearings. *J. Sound Vib.* 306, 601–617.  
 Keogh, P.S., 2012. Contact dynamic phenomena in rotating machines: active/passive considerations. *Mech. Syst. Signal Process.* 29, 19–33.  
 Keogh, P.S., Yong, W.Y., 2007. Thermal assessment of dynamic rotor/auxiliary bearing contact events. *ASME J. Tribol.* 129, 143–152.  
 Krämer, E., 1993. *Dynamics of Rotors and Foundations*. Springer-Verlag, Berlin.  
 Lee, J.G., Palazzolo, A., 2012. Catcher bearing life prediction using a rainflow counting approach. *ASME J. Tribol.* 134.  
 Liu, W., Zhang, Y., Feng, Z., Zhao, J., Wang, D., 2014. A study on waviness induced vibration of ball bearings based on signal coherence theory. *J. Sound Vib.* 333, 6107–6120.  
 Liu, T., Lyu, M., Wang, Z., Yan, S., 2018. An identification method of orbit responses rooting in vibration analysis of rotor during touch-downs of active magnetic bearings. *J. Sound Vib.* 414, 174–191.  
 Mohanty, A.R., 2015. *Machinery Condition Monitoring Principal and Practice*. CRC Press, Taylor & Francis.  
 Muszynska, A., 1984. Partial lateral rotor to stator rubs. *Proc. Inst. Mech. Eng.* C281–C284.  
 Neisi, N., Sikanen, E., Heikkinen, J.E., Sopanen, J., 2018. Effect of off-sized balls on contact stresses in a touchdown bearing. *Tribol. Int.* 120, 340–349.  
 Nelson, H.D., 1980. A finite rotating shaft element using Timoshenko beam theory. *ASME Journal of Mechanical Design* 102 (4), 793–803.  
 Newkirk, B.L., 1926. Shaft rubbing. *Mech. Eng.* 48, 830–832.  
 Nguyen-Schäfer, 2016. *Hung Computational Design of Rolling Bearings*. Springer International Publishing.

- Palmgren, A., 1959. Ball and Roller Bearing Engineering, third ed. pp. 34–41 Burbank, Philadelphia.
- Poritsky, H., Hewlett, C.W., Coleman, R.E., 1947. Sliding friction of ball bearings of the pivot type. *J. Appl. Mech.* 14, 261–268.
- Schmied, J., Pradetto, J.C., 1992. Behaviour of a one ton compressor rotor being dropped into the auxiliary bearings. Proceeding of the third international symposium on magnetic bearings, Alexandria 145–156.
- Sopanen, J., Mikkola, A., 2003. Dynamic model of a deep-groove ball bearing including localized and distributed defects. Part 1: Theory. *Proc. Inst. Mech. Eng. - Part K J. Multi-body Dyn.* 217, 201–211.
- Sun, G., 2006a. Auxiliary bearing life prediction using Hertzian contact bearing model. *ASME Journal of Vibration and Acoustics* 128, 203–209.
- Sun, G., 2006b. Rotor drop and following thermal growth simulations using detailed auxiliary bearing and damper models. *J. Sound Vib.* 289, 334–359.
- Takabi, J., Khonsari, M.M., 2013. Experimental testing and thermal analysis of ball bearings. *Tribol. Int.* 60, 93–103.
- Takabi, J., Khonsari, M.M., 2016. On the thermally-induced failure of rolling element bearings. *Tribol. Int.* 94, 661–674.
- Taylor, H.D., 1924. Rubbing shafts above and below resonant speed. GE Technical Information Series, No. 16709 16709.
- Wardle, F.P., 1988a. Vibration forces produced by waviness of the rolling surfaces of thrust loaded ball bearings Part 1: Theory. *Proc. IME C J. Mech. Eng. Sci.* 202, 305–312.
- Wardle, F.P., 1988b. Vibration forces produced by waviness of the rolling surfaces of thrust loaded ball bearings Part 2: experimental validation. *Proc. IME C J. Mech. Eng. Sci.* 202, 313–319.
- API. Axial and Centrifugal Compressors and Expander-compressors for Petroleum, Chemical and Gas Industry Services (Standard API 617). American Petroleum Institute, USA.
- Yan, K., Wang, N., Zhai, Q., Zhu, Y., Zhang, J., Niu, Q., 2015. Theoretical and experimental investigation on the thermal characteristics of double-row tapered roller bearings of high speed locomotive. *Int. J. Heat Mass Tran.* 84, 1119–1130.
- Zhao, Y., Yang, G., Shi, Z., Zhao, L., 2016. Thermal analysis and simulation of auxiliary bearings and its application in the high temperature reactor-10. *J. Tribol.* 138.
- Zhuo, Y., Zhou, X., Yang, C., 2014. Dynamic analysis of double-row self-aligning ball bearings due to applied loads, internal clearance, surface waviness and number of balls. *J. Sound Vib.* 333, 6170–6189.

### Publication III

Neisi, N., Ghalamchi, B., Heikkinen, J., Sillanpää, T., Hartikainen, T., Sapanen, J.

**A Case Study of the Contact Force and Stress in the Backup Bearing of a Generator: Experimental Study and Numerical Simulation of Dropdown.**

Reprinted with permission from  
*Mechanisms and Machine Science*

IFToMM 2018: Proceedings of the 10th International Conference on Rotor Dynamics – IFToMM, Vol(62), 2019.

© 2019, Springer Nature.





# A Case Study of the Contact Force and Stress in the Backup Bearing of a Generator: Experimental Study and Numerical Simulation of Dropdown

Neda Neisi<sup>1</sup> , Behnam Ghalamchi<sup>1,2</sup>, Janne E. Heikkinen<sup>1</sup>,  
Teemu Sillanpää<sup>1</sup>, Toni Hartikainen<sup>3</sup>, and Jussi Sopenen<sup>1</sup>

<sup>1</sup> Lappeenranta University of Technology,  
Skinnarilankatu 34, 53850 Lappeenranta, Finland  
neda.neisi@lut.fi

<sup>2</sup> Department of Mechanical Engineering,  
Laboratory of Unmanned Aerial Robotics, University of California, Berkeley,  
2000 Carleton Street, Berkeley, CA 94720-2284, USA

<sup>3</sup> Aurelia Turbines, Höyläkatu, 1, 53500 Lappeenranta, Finland

**Abstract.** This paper presents both experimental and numerical study on the dropdown of a generator rotor in a two-stage radial gas turbine utilizing AMB system. The simulation unifies the FE-model of the flexible rotor and the dynamic model of backup bearings. The system under investigation includes a flexible rotor, an axial and two radial AMBs and two backup bearings, double row angular contact ball bearings. The recorded behavior of the studied rotor in the sudden failure of the electromagnetic field is demonstrated. Furthermore, the fine-tuned rotor-system model is used for studying the contact force and the contact stress in the backup bearing. The comparison between the measured results and the simulated results confirms that the used simulation tool can be applied for the design consideration of rotor-backup bearing system and enables to investigate the effect of various design parameters on the dynamic behavior of rotor in the dropdown.

**Keywords:** Backup bearing • Rotor • Dropdown

## 1 Introduction

Applying active magnetic bearing (AMB) system in high-speed turbomachinery has numerous advantages in preference to utilizing the conventional mechanical bearing. In order to avoid fatal failure in loss of electromagnetic field principally because of the electric short circuit and the fault in the control system, these machineries are equipped with the backup bearings to secure the rotor and AMB components, mainly the radial actuators and position sensors, from the damages in the dropdown. The backup bearings bear the high contact load and a friction rub. The backup bearing can be also known as either auxiliary bearing or touchdown bearing. During the last years, several researches have been conducted on the simulation of the dropdown. In the study of

© Springer Nature Switzerland AG 2019

K. L. Cavalca and H. I. Weber (Eds.): IFToMM 2018, MMS 62, pp. 374–386, 2019.  
[https://doi.org/10.1007/978-3-319-99270-9\\_27](https://doi.org/10.1007/978-3-319-99270-9_27)

Kärkkäinen et al. [1] the contact forces and friction force during the dropdown has been demonstrated. The contact of the rotor and backup bearing, open-loop, and closed-loop control system for AMB as well as transient analysis of the temperature in the rotor drop have been also discussed in the papers presented by Keogh [2, 3]. Recently, Liu et al. [4] developed a numerical model based on signal processing to recognize the complete rub of the rotor, bounce of the rotor after the contact with backup bearing and the pendulum movement of the rotor.

In the design aspect of the backup bearing, it is essential to decrease the deformation of the backup bearing and maintain the maximum stress in bearing below the endurance limit for the stress in the bearing. There are a limited number of studies about the contact stress in the backup bearing [5, 6]. Sun [5] applied the Lundberg-Palmgren theory to evaluate the fatigue life of the backup bearing. This theory specifically can be used for the steady state condition of the bearing. Lee and Palazzolo [6] considered the stress counting method, rainflow method, for calculation of the fatigue life of the backup bearing. Besides that, the effect of the off-sized ball in the contact stress of the backup bearing has been studied by Neisi et al. [7]. Above study indicated that the dimension and location of the off-sized ball/balls can influence the contact stress in the backup bearing. Apart from this several researches have been conducted on the thermal analysis of backup bearings [8–10].

Most of the available studies on the AMB supported rotors are devoted to the numerical simulation of dropdown and few publications can be found studied the rotor dropdown both experimentally and numerically. An experimental study on the dropdown test by Schmied and Pradetto [11] showed that because of the time lag in the control system, the electromagnetic force might exist in the machine. Therefore, the results of the simulation can be different compared to the recorded behavior of the rotor in the test bench. The comparison between the measured and the simulated results can be used for the design consideration of rotor-backup bearing system and enables to evaluate the influence of various design parameters on the dynamic behavior of rotor in the dropdown and still needs to be studied. For this reason, this work presents both experimental and numerical study on the dropdown of a generator rotor in a two-stage radial gas turbine employing AMB system. The unit composed of LP and HP rotors operating at supercritical speed. This work concentrates on the study the dropdown of LP rotor. The normal operation speed of both rotors is 550 Hz and the unit generates up to 400 kW electric power. The FE-model of the rotor is validated with the experimental modal analysis. The system under investigation includes a flexible rotor, an axial and two radial AMBs and two backup bearings, double row angular contact ball bearings. In this study, the recorded behavior of the studied rotor in sudden failure of the electromagnetic field is demonstrated. The description of the support stiffness and friction coefficients in the bearings are fine-tuned in the rotor model to meet the measured results during the dropdown. In addition, the fine-tuned rotor-system model is used for studying the contact force and contact stress in the backup bearing. Furthermore, the rotor orbit and the displacement of the rotor during the dropdown are featured.

## 2 Model of Rotor and Backup Bearing

Figure 1 shows the rotor under investigation. The rotor is modeled using shear deformable beam elements. In a rotor dropdown, the backup bearing supports the rotor by nonlinear contact load. The equation of motion is as follows [12]:

$$\mathbf{M}\ddot{\mathbf{X}} + (\mathbf{C} + \omega\mathbf{G})\dot{\mathbf{X}} + \mathbf{K}\mathbf{X} = \omega^2\mathbf{F}_1 + \mathbf{F}_2 \quad (1)$$

where  $\mathbf{M}$ ,  $\mathbf{C}$ ,  $\mathbf{K}$ , and  $\mathbf{G}$  are mass, damping, stiffness and gyroscopic matrix, respectively.  $\mathbf{X}$  is the vector of the generalized coordinate. The vector  $\mathbf{F}_1$  is the vector of nodal unbalance and  $\mathbf{F}_2$  represents the vector externally applied forces. The angular velocity of the rotor is  $\omega$ .

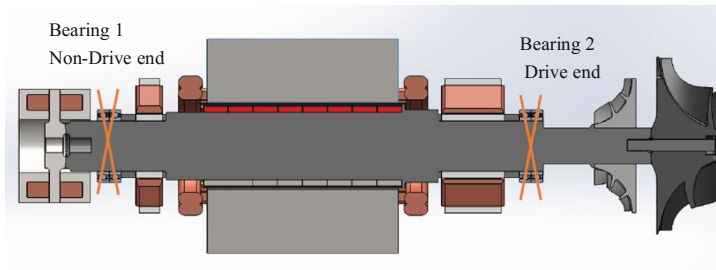


Fig. 1. Rotor under investigation

Applying a pair of angular contact ball bearings as backup bearings enable to take the advantage of the ability of backup bearing to withstand both the axial and radial loads, low friction, lubricant free and compact size. The backup bearings are considered as consumable parts. After several dropdowns, because of the high contact forces and mechanical rub, it is required to replace them. The model for the backup bearing, duplex pair of angular contact ball bearing, is developed on the basis of the ball bearing model introduced by Sopenan and Mikkola [13]. The bearing forces are calculated based on the bearing geometry, material property and the deformation of the bearing in the dropdown. In the model, the relative displacement between races is given by:

$$\begin{aligned} e_j^r &= e_x \cos \beta_j + e_y \sin \beta_j \\ e_j^t &= e_z - (\psi_x \sin \beta_j + \psi_y \cos \beta_j)(R_{in} + r_{in}) \end{aligned} \quad (2)$$

where  $e_{x,y,z}$  represent the relative displacements of the bearing races (Fig. 2), and  $\psi_x$  and  $\psi_y$  show the tilting of the inner race in  $x$ ,  $y$ -axis.  $\beta_j$  is the attitude angle of  $j^{\text{th}}$  ball. Thus, the distance between the races can be calculated as follows:

$$D_j = r_{out} + r_{in} - \frac{R_{in} + r_{in} + e_j^r - R_{out} + r_{out}}{\cos \varphi_j} \quad (3)$$

where  $\varphi_j$  is the contact angle.

$$\varphi_j = \tan^{-1} \left( \frac{e_j^t}{R_{in} + r_{in} + e_j^r - R_{out} + r_{out}} \right) \quad (4)$$

where  $R_{in}$  and  $r_{in}$  represent the inner race radius and inner race groove radius, correspondingly.

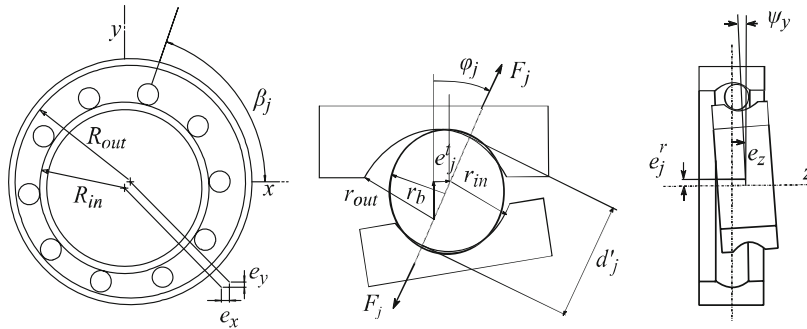


Fig. 2. Ball bearing model

The following equation expresses the total elastic deformation of the inner ring.

$$\delta_j^{tot} = d_j - D_j \quad (5)$$

The Hertzian contact theory has been used for the calculation of the contact force in the dropdown. Where the contact force between ball  $j^{th}$  and the inner race is as follows [12]:

$$F_j = K_c^{tot} \left( \delta_j^{tot} \right)^{3/2} \quad (6)$$

where the total contact stiffness is denoted as  $K_c^{tot}$  [13].

### 2.1 Model of the Contact Between Rotor and Backup Bearing

The contact between the rotor and backup bearing is modeled based upon the modified Hertzian contact model [1]:

$$F_r = \begin{cases} K\delta^{10/9} \left( 1 + (3/2)\lambda\dot{\delta} \right); & e_r > c_r \text{ and } F_r > 0 \\ 0; & e_r \leq c_r \text{ and } F_r \leq 0 \end{cases} \quad (7)$$

where  $K$  represents the contact stiffness between the rotor and inner race and  $\lambda$ , is a contact parameter. In above equation, the penetration of the rotor in the backup bearing can be calculated as follows:

$$\delta = e_r - c_r \tag{8}$$

where  $c_r$  is the radius of the air gap between the rotor and backup bearing, and the radial displacement of the rotor is denoted as  $e_r$  [1].

The friction force between the rotor and backup bearing can be obtained by:

$$F_\mu = \mu F_r \tag{9}$$

where  $\mu$  is the friction coefficient and the detailed calculation of the friction coefficient is described in the study of Kärkkäinen et al. [1]. In the model, the coordinate system in the FE-model of rotor and bearing model are mapped together.

### 2.2 Model of Contact Stress in Backup Bearing

The design of the backup bearing requires to evaluate the contact load, deformation of the bearing and make sure that the stress carried by backup bearings does not exceed the maximum allowable stress for bearings. The Hertzian contact model can be implemented for the calculation of the contact stress in the backup bearing. In this method, the stress can be calculated from the projection of elliptic contact area between the ball and bearing race. The highest stress can be found at the at the geometrical contact area [14]:

$$\sigma_{\max} = \frac{3Q_j}{2\pi ab} \tag{10}$$

where the semi-major and minor axes of the elliptic contact are denoted as  $a$  and  $b$ , correspondingly.

## 3 Case Studies and Results

The parameters required to analyze the case study of the rotor are shown in Table 1. The FE-model of the rotor is depicted in Fig. 3. The backup bearings are a pair of angular contact ball bearings type XCB71914-E-2RSD-T-P4S-U (Schaeffler) mounted in X-arrangement. The parameter used for the supports is shown in Table 2.

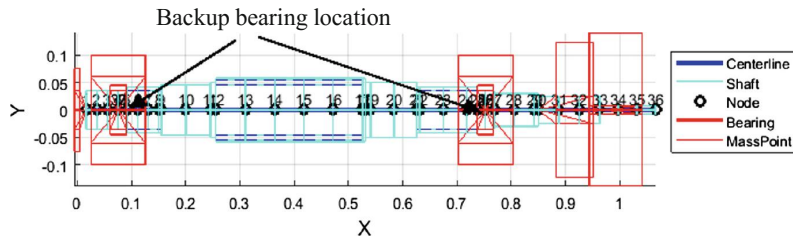


Fig. 3. The main dimensions and finite element model of the rotor.

**Table 1.** The main data for the simulation of the rotor dropdown

Initial rotation speed of the rotor	60 Hz
Modulus of elasticity	$2.0 \cdot 10^{11}$ Pa
Mass of rotor	59.5 kg
Poisson's ratio	0.3
Contact stiffness between rotor and backup bearings	$2.4 \cdot 10^9$ N/mm <sup>1.11</sup>
Air gap	250 $\mu$ m
Unbalance mass at Non drive end of generator active part	$4.4 \cdot 10^{-6}$ kg m @ 0°
Unbalance mass at drive end of generator active part	$4.4 \cdot 10^{-6}$ kg m @ 0°
Unbalance mass at compressor impeller	$0.6 \cdot 10^{-6}$ kg m @ 0°
Unbalance mass at turbine impeller	$3.1 \cdot 10^{-6}$ kg m @ 0°
Static contact friction coefficient between rotor and inner race	0.15
Dynamic contact friction coefficient between rotor and inner race	0.1

**Table 2.** The parameters used for rigid and soft supports

Mass	5 kg
Stiffness	$2.4 \cdot 10^9$ N/m
Damping	$2.8 \cdot 10^3$ Ns/m

The mass properties of the compressor and turbine impellers are shown in Table 3. In the FE-model of the rotor, the impellers are modeled as mass points and they are connected to the rotor by spring model.

**Table 3.** Mass properties of the impellers

	Compressor	Turbine
Material	Aluminum alloy 7075-T6	Heat resistant alloy steel
Mass (kg)	2.7	9.9
Center of mass x, y, z (m)	0, 0, 0.0648	0, 0, 0.03749
Moment of inertia $I_d$ , $I_p$ (kg m <sup>2</sup> )	0.0197, 0.0126	0.0436, 0.0449

### 3.1 Orbital Motion of Rotor

Figure 4 features the rotor orbit at the location of backup bearings. In the dropdown, the rotor falls down and contacts the backup bearing. After the initial hit, the rotor bounces back and again hits the bearing. This can repeat until the rotor steady set in the bearing.

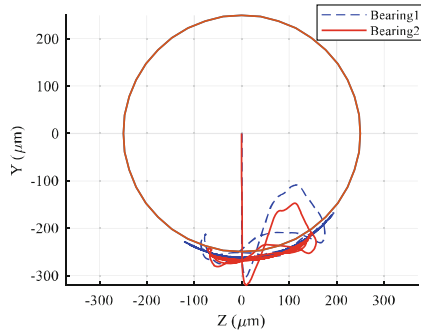


Fig. 4. Rotor orbit, dropdown simulation at 60 Hz

### 3.2 Contact Forces and Stress

The contact force in the backup bearing is modeled on the basis of the bearing model presented in the paper by Kurvinen et al. [15]. As can be seen in Fig. 5, in the first hit of the rotor with backup bearing, the bearing bears high contact force, about 2346 N at the drive end (Bearing 2). In the subsequent contacts, the magnitude of the contact force is decreased and after continues rub in the backup bearing reaches to the stable value. The figure shows that in the initial contacts of the rotor and bearing, the contact force in the drive end (Bearing 2) is approximately 1.36 times of the force in the Non-drive end (Bearing 1) and in the following contacts, the difference between the contact forces in the bearings is reduced. In the beginning of the dropdown, the rotor has a considerable kinematic energy. Therefore, when the rotor hits the bearing for the first time, the highest contact force is observed. As a result of the friction between the rotor and backup bearing, part of the kinetic energy of rotor is dissipated as friction heat generation. For this reason, in the subsequent contacts, the magnitude of contact force is reduced. It should be noted that due to the movement of the ball inside the bearing, the location where the highest contact force exists is changing. Furthermore, the center

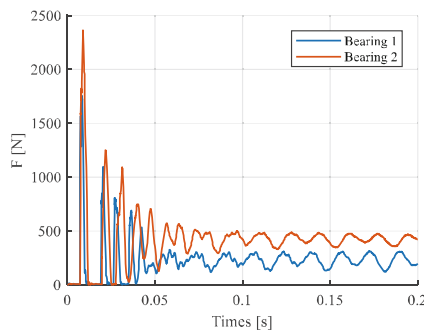
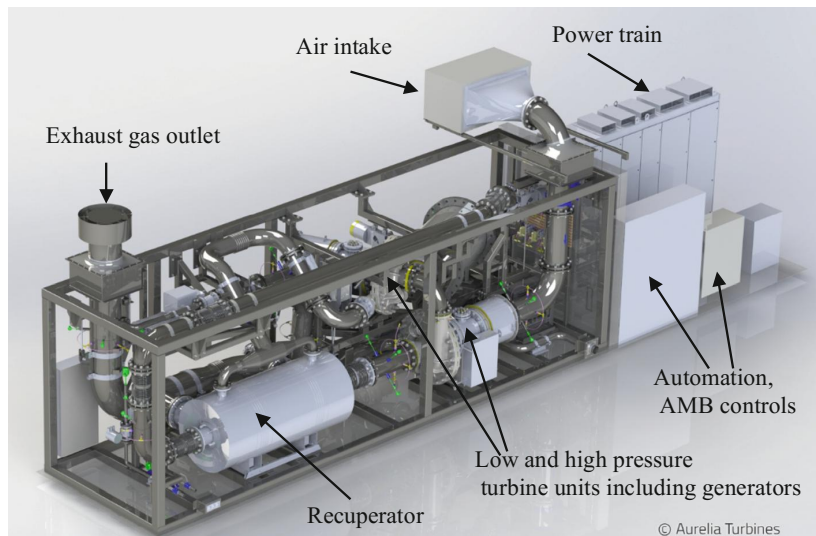


Fig. 5. Contact force in the bearing

of mass of the rotor is close to the drive end or rotor (Bearing 2). Therefore, the force in the Bearing 2 is higher than the Bearing 1. After obtaining the contact force between the balls and inner race, the maximum Hertzian contact stress between balls and bearing ring is obtained (Eq. 10). The highest contact stress in the contact of the rotor and Bearing1 and Bearing 2 found to be 3451 and 3549 MPa, respectively.

### 3.3 Experimental Result

The prototype of two-stage radial gas turbine shown in Fig. 6 produces 400 kW electricity. The nominal operation speed of both rotors is 550 Hz. The dropdown test of the rotor was carried out at two different speeds: 60 and 100 Hz. Before the dropdown, the rotor was supported by active magnetic bearings. Then, the magnetic bearing source was switched off and the unit is shut down. The measurement setup is equipped with two non-contact displacement sensors at the location of each backup bearings and the relative displacement of the rotor is recorded. These sensors are mounted at 45° with respect to the vertical axis of the rotor. For this reason, it is required to map the recorded data to the coordinate system used in the FE-model of the rotor. By means of a third noncontact probe, the displacement of the rotor in the axial direction is measured. The dropdown speed has been also recorded.



**Fig. 6.** The figure of the prototype for two-stage radial gas turbine under investigation.

Figure 7 depicts the recorded orbital movement of the rotor for the dropdown test at 60 and 100 Hz. As can be seen in Fig. 7(a and b), when the rotor drops, the rotor moves downward, then bounces back and it hits the backup bearing over and over until

thoroughly settles on the bottom of the bearing inner ring. When the rotor is dropped at higher initial rotational speed, the first bounce is higher.

The comparison of the orbital movement of the rotor shown in Fig. 4 (simulation tool) and the rotor orbit measured in the test (Fig. 7a and b) reveals that the simulation model is able to feature the orbital movement of the rotor. However, the amplitude of the rotor orbit in the measurement found to be different from the simulation. The test results show that the radial displacement of the rotor exceeds  $280\ \mu\text{m}$ , while the simulation results indicated that in the first contact, the displacement of the rotor exceeds  $250\ \mu\text{m}$ . Then, the radial displacement is reduced around the air gap and the rotor starts to have a wobbling movement on the bottom of the bearing and the radial displacement is reduced around the air gap. There are several possible explanations can be found for this difference between the amplitude of orbit in the simulation and test result. In the numerical simulation, the air gap clearance is in accordance to the air gap clearance in the design phase of machine. One of the primary reasons for this discrepancy can be due to the problem in the sensitivity of sensor and the electrical runout particularly because of the dent, scratch in the probe area of the rotor and rotor runout. Furthermore, the structure of the support of the machine is complicated and the simulation of dropdown generally requires simplifications in supports definition. The rotor orbit is obtained from the displacement of the rotor in horizontal and vertical direction and the effect of the support stiffness in the amplitude of the rotor displacement cannot be neglected.

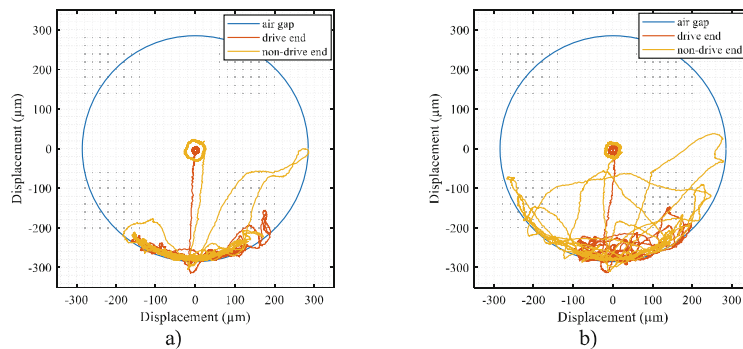
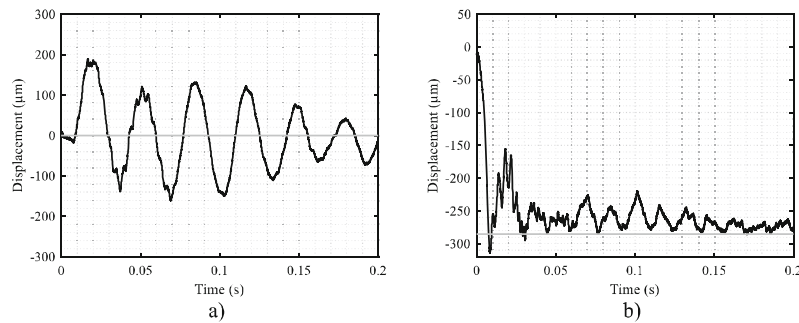


Fig. 7. Orbit movement of rotor at different dropdown speeds (a) 60 Hz (b) 100 Hz

Figure 8 depicts the displacement of the rotor for the dropdown at 60 Hz at the drive end backup bearing. It is clear from Fig. 8 that when the electromagnetic field switched off, the rotor has high displacement in the vertical direction, while the horizontal displacement of the rotor is considerably lower. Figure 8a shows that the rotor starts to have the highest oscillation in the horizontal direction about  $200\ \mu\text{m}$  which is less than the air gap and gradually the horizontal displacement of the rotor is reduced and the rotor stabilized around the vertical centerline of the bearings. Figure 8b features

that the rotor descends and the vertical displacement of the rotor is over  $320\ \mu\text{m}$ . Afterwards, the rotor moves up. In the following contacts, the displacement of the rotor decreases. In the first interaction of rotor and backup bearing, the contact force is so high that the vertical displacement of the rotor exceeding the air gap, then the rotor is reflected from the inner ring. Later, the vertical displacement of the rotor is reduced and the rotor starts to stabilize within the air gap.



**Fig. 8.** Displacement of rotor at the location of backup bearing (drive end), dropdown test at 60 Hz (a) x-direction (b) y-direction

The displacement of the rotor at the location of the non-drive end backup bearing is shown in Fig. 9. The same as the drive end bearing, the highest displacement of the rotor at vertical direction was recorded at the first contact of the rotor and bearing and then the amplitude of the displacement is decreased. The results reveal a clear difference between the recorded displacement of the rotor at the backup bearing in the drive end and non-drive end. First, the recording shows that the maximum displacement of the rotor at the non-drive end is approximately  $300\ \mu\text{m}$  that is less than the maximum displacement at the drive end of the rotor. Second, the comparison of Figs. 8b and 9b shows that the rotor contacts the bearings at different times. Third, it can be found from the measurement data that the rotor hits the drive end more than the non-drive end.

The mass center of the rotor is close to the drive end bearing. The static force equilibrium of the rotor shows that the force in drive end bearing is higher than non-drive end bearing. Therefore, the vertical displacement of the rotor at the drive end bearing is higher and it is confirmed by measurement results. In addition, the high number of contacts of the rotor with drive end bearing can be attributed the conical movement of the rotor that has a good agreement with the results of our previous study on the rotor dynamic analysis of the rotor (The rotor dynamic analysis indicated that at lower frequencies the rotor has a conical mode shape).

In the test setup, the axial displacement of the rotor is measured by non-contact displacement probe close to the axial disc of the rotor. The axial clearance of the axial safety bearing is  $900\ \mu\text{m}$ . Figure 10 shows the axial displacement of the rotor for the dropdown test at 60 Hz. The measurement shows that from the start of the dropdown until the first contact of rotor and backup bearing the rotor has an axial displacement of

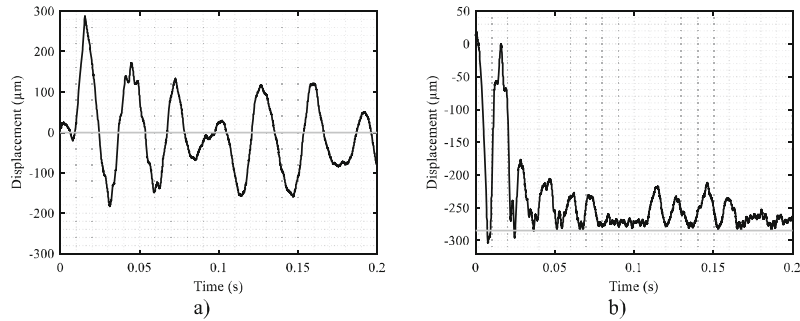


**Fig. 9.** Displacement of rotor at the location of backup bearing (Nondrive end), dropdown test at 60 Hz (a) x-direction (b) y-direction

80  $\mu\text{m}$ . Then, very rapidly, the rotor moves axially in opposite direction. And from 40  $\mu\text{m}$  at 0.02 s, the rotor experiences the higher axial displacement of 110  $\mu\text{m}$  at 0.05 s. Then, the direction of the movement reversed until 0.1 s. After that, the axial displacement of the rotor is reduced and the rotor experiences several backs and forth movements.

Even though the magnitude of the axial displacement of the rotor seems to be small compared to the maximum limit for the clearance, the data provides an important information about the behavior of the rotor. In the normal operation of the machine, the pressurized air in the outlet of the compressor directed to the turbine impeller and when the switch of electromagnetic field turned off, the axial force resulted from the back pressure in the compressor impeller causes that the rotor moves reversely. The rotor undergoes several backs and forth axial movement particular because of the unstable fluid flow in the dropdown. In the numerical simulation, the axial pressure in the compressor section is not taken into account. It should be remind that this dropdown test was carried out at very low speed rather than the operation speed of rotor (550 Hz). The existence of the axial pressure from the compressor impeller can provide a physical

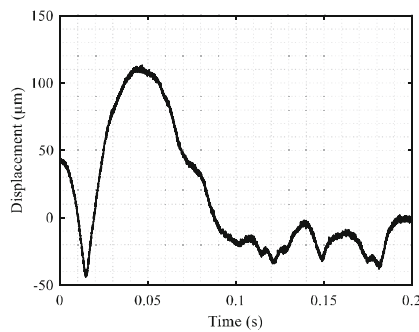


**Fig. 10.** Axial displacement of rotor, dropdown test at 60 Hz

explanation that the outcome of the simulation of the two-stage radial gas turbine generator rotor, mainly at operating speed, expected to be different from the real behavior of the rotor in the dropdown. In future, the effect of the force from the magnetic field and also the axial force in the compressor impeller needs to be considered.

#### 4 Conclusion

On the circumstance that the electromagnetic field fails, the rotor drops and the backup bearing suffers from high contact load. A numerical and experimental study on the dropdown of the case study of the rotor in a two-stage radial gas turbine generator unit was carried out. The contact forces and the stress in the backup bearing were studied. For the purpose of the calculation of the contact forces in the dropdown, the Hertzian contact model was implemented. The contact force between the rotor and backup bearing and the contact force in the bearing was calculated. The results indicated that the backup bearing is exposed to time-varying load. The backup bearing bears the high contact load during the initial hit of the rotor with the bearing. In addition, the maximum Hertzian stress between the ball and the bearing race was obtained. In the test setup, the dropdown of the rotor for various dropdown speed was carried out. The displacement of the rotor in the location of backup bearing and the rotor orbits was featured. The simulation result had a agreement with the recorded behavior of the rotor in the experimental dropdown. For further improvement in the dropdown simulation, the axial pressure in the compressor impeller should be taken into account.

#### References

1. Kärkkäinen, A., Sopenan, J., Mikkola, A.: Dynamic simulation of a flexible rotor during drop on retainer bearings. *J. Sound Vib.* **306**, 601–617 (2007)
2. Keogh, P.S.: Contact dynamic phenomena in rotating machines: active/passive considerations. *Mech. Syst. Signal Process.* **29**, 19–33 (2012)
3. Keogh, P.S., Yong, W.Y.: Thermal assessment of dynamic rotor/auxiliary bearing contact events. *ASME J. Tribol.* **129**, 143–152 (2007)
4. Liu, T., Lyu, M., Wang, Z., Yan, S.: An identification method of orbit responses rooting in vibration analysis of rotor during touchdowns of active magnetic bearings. *J. Sound Vib.* **414**, 174–191 (2018)
5. Sun, G.: Auxiliary bearing life prediction using Hertzian contact bearing model. *ASME J. Vib. Acoust.* **128**, 203–209 (2006)
6. Lee, J.G., Palazzolo, A.: Catcher bearing life prediction using a rainflow counting approach. *ASME J. Tribol.* **134**, 031101:1–031101:15 (2012)
7. Neisi, N., Sikanen, E., Heikkinen, J.E., Sopenan, J.: Effect of off-sized balls on contact stresses in a touchdown bearing. *Tribol. Int.* **120**, 340–349 (2018)
8. Jin, C., Zhu, Y., Xu, L., Xu, Y., Zheng, Y.: The thermodynamic properties of a new type catcher bearing used in active magnetic bearings system. *Appl. Therm. Eng.* **82**, 253–263 (2015)
9. Zhao, Y., Yang, G., Shi, Z., Zhao, L.: Thermal analysis and simulation of auxiliary bearings and its application in the high temperature reactor-10. *J. Tribol.* **138**, 011102:1–011102:11 (2016)

10. Sun, G.: Rotor drop and following thermal growth simulations using detailed auxiliary bearing and damper models. *J. Sound Vib.* **289**, 334–359 (2006)
11. Schmied, J., Pradetto, J.C.: Behaviour of a one ton compressor rotor being dropped into the auxiliary bearings. In: *Proceeding of the Third International Symposium on Magnetic Bearings*, Alexandria, pp. 145–156 (1992)
12. Kärkkäinen, A.: Dynamic simulations of rotors during drop on retainer bearings. Ph.D. thesis, Lappeenranta University of Technology, Finland (2007)
13. Sopanen, J., Mikkola, A.: Dynamic model of a deep-groove ball bearing including localized and distributed defects. Part 1: Theory. *Proc. Inst. Mech. Eng. Part K J. Multi-body Dyn.* **217**, 201–211 (2003)
14. Harris, T.A., Kotzalas, M.N.: *Essential Concepts of Bearing Technology: Rolling Bearing Analysis*, 5th edn. CRC Press, Boca Raton (2007)
15. Kurvinen, E., Sopanen, J., Mikkola, A.: Ball bearing model performance on various sized rotors with and without centrifugal and gyroscopic forces. *Mech. Mach. Theory* **90**, 240–260 (2015)



## **Publication IV**

Neisi, N., Heikkinen, J., Sillanpää, T., Hartikainen, T., Sapanen, J.  
**Performance evaluation of touchdown bearing using model-based  
approach.**

Accepted to  
*Nonlinear dynamics*, 2020



## ACTA UNIVERSITATIS LAPPEENRANTAENSIS

871. HUJALA, ELINA. Quantification of large steam bubble oscillations and chugging using image analysis. 2019. Diss.
872. ZHIDCHENKO, VICTOR. Methods for lifecycle support of hydraulically actuated mobile working machines using IoT and digital twin concepts. 2019. Diss.
873. EGOROV, DMITRY. Ferrite permanent magnet hysteresis loss in rotating electrical machinery. 2019. Diss.
874. PALMER, CAROLIN. Psychological aspects of entrepreneurship – How personality and cognitive abilities influence leadership. 2019. Diss.
875. TALÁSEK, TOMÁS. The linguistic approximation of fuzzy models outputs. 2019. Diss.
876. LAHDENPERÄ, ESKO. Mass transfer modeling in slow-release dissolution and in reactive extraction using experimental verification. 2019. Diss.
877. GRÜNENWALD, STEFAN. High power fiber laser welding of thick section materials - Process performance and weld properties. 2019. Diss.
878. NARAYANAN, ARUN. Renewable-energy-based single and community microgrids integrated with electricity markets. 2019. Diss.
879. JAATINEN, PEKKO. Design and control of a permanent magnet bearingless machine. 2019. Diss.
880. HILTUNEN, JANI. Improving the DC-DC power conversion efficiency in a solid oxide fuel cell system. 2019. Diss.
881. RAHIKAINEN, JARKKO. On the dynamic simulation of coupled multibody and hydraulic systems for real-time applications. 2019. Diss.
882. ALAPERÄ, ILARI. Grid support by battery energy storage system secondary applications. 2019. Diss.
883. TYKKYLÄINEN, SAILA. Growth for the common good? Social enterprises' growth process. 2019. Diss.
884. TUOMISALO, TEEMU. Learning and entrepreneurial opportunity development within a Finnish telecommunication International Venture. 2019. Diss.
885. OYEDEJI, SHOLA. Software sustainability by design. 2019. Diss.
886. HUTTUNEN, MANU. Optimizing the specific energy consumption of vacuum filtration. 2019. Diss.
887. LIIKANEN, MIIA. Identifying the influence of an operational environment on environmental impacts of waste management. 2019. Diss.
888. RANTALA, TERO. Operational level performance measurement in university-industry collaboration. 2019. Diss.
889. LAUKKANEN, MINTTU. Sustainable business models for advancing system-level sustainability. 2019. Diss.

- 890.** LOHRMANN, CHRISTOPH. Heuristic similarity- and distance-based supervised feature selection methods. 2019. Diss.
- 891.** ABDULLAH, UMMI. Novel methods for assessing and improving usability of a remote-operated off-road vehicle interface. 2019. Diss.
- 892.** PÖLLÄNEN, ILKKA. The efficiency and damage control of a recovery boiler. 2019. Diss.
- 893.** HEKMATMANESH, AMIN. Investigation of EEG signal processing for rehabilitation robot control. 2019. Diss.
- 894.** HARMOKIVI-SALORANTA, PAULA. Käyttäjät liikuntapalvelujen kehittäjinä - Käyttäjälähtöisessä palveluinnovaatioprosessissa käyttäjien tuottama tieto tutkimuksen kohteena. 2020. Diss.
- 895.** BERGMAN, JUKKA-PEKKA. Managerial cognitive structures, strategy frames, collective strategy frame and their implications for the firms. 2020. Diss.
- 896.** POLUEKTOV, ANTON. Application of software-defined radio for power-line-communication-based monitoring. 2020. Diss.
- 897.** JÄRVISALO, HEIKKI. Applicability of GaN high electron mobility transistors in a high-speed drive system. 2020. Diss.
- 898.** KOPONEN, JOONAS. Energy efficient hydrogen production by water electrolysis. 2020. Diss.
- 899.** MAMELKINA, MARIA. Treatment of mining waters by electrocoagulation. 2020. Diss.
- 900.** AMBAT, INDU. Application of diverse feedstocks for biodiesel production using catalytic technology. 2020. Diss.
- 901.** LAAPIO-RAPI, EMILIA. Sairaanhoidajien rajatun lääkkeenmääräämistoiminnan tuottavuuden, tehokkuuden ja kustannusvaikuttavuuden arviointi perusterveydenhuollon avohoidon palveluprosessissa. 2020. Diss.
- 902.** DI, CHONG. Modeling and analysis of a high-speed solid-rotor induction machine. 2020. Diss.
- 903.** AROLA, KIMMO. Enhanced micropollutant removal and nutrient recovery in municipal wastewater treatment. 2020. Diss.
- 904.** RAHIMPOUR GOLROUDBARY, SAEED. Sustainable recycling of critical materials. 2020. Diss.
- 905.** BURGOS CASTILLO, RUTELY CONCEPCION. Fenton chemistry beyond remediating wastewater and producing cleaner water. 2020. Diss.
- 906.** JOHN, MIHA. Separation efficiencies of freeze crystallization in wastewater purification. 2020. Diss.
- 907.** VUOJOLAINEN, JOUNI. Identification of magnetically levitated machines. 2020. Diss.
- 908.** KC, RAGHU. The role of efficient forest biomass logistics on optimisation of environmental sustainability of bioenergy. 2020. Diss.





ISBN 978-952-335-521-7  
ISBN 978-952-335-522-4 (PDF)  
ISSN-L 1456-4491  
ISSN 1456-4491  
Lappeenranta 2020